Computer modelling of complex oxide surfaces

Kelsey, E. T.

Award date:
1993

Awarding institution:
University of Bath

Computer Modelling of Complex Oxide Surfaces

submitted by E. T. Kelsey

for the degree of PhD

of the University of Bath

1993

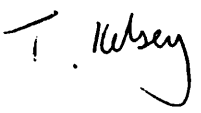

ProQuest LLC
789 East Eisenhower Parkway
P.O. Box 1346
Ann Arbor, MI 48106-1346

Abstract

The aim of this thesis is to model complex oxide surfaces using computer simulation techniques to study the structure and properties. In Chapter 1 we introduce the experimental methods and discuss the purpose of simulation. Chapter 2 examines the theory behind the methods for modelling different structures. Chapter 3 shows how we develop potential models able to reproduce and predict the properties of real materials.

The remainder of this thesis presents the results of calculations on bulk and surface structures. In Chapter 4 zinc oxide is modelled and the defect structure of the bulk is related to the known properties of the solid. The defects present on the surface are determined and used to locate possible catalytic sites. Ternary oxides with the ilmenite and perovskite structures are modelled in Chapter 5 and their calculated bulk and surface structures compared to previous computational and experimental work. In addition to defect calculations, the ability of static simulations to model different phases is tested. In Chapter 6, the calculation of the bulk structure of barium sulphate is enabled by a model which includes intramolecular forces for the polyanion. However relating the predicted and the observed morphologies requires an attempt to determine kinetic factors affecting growth rates under different conditions, and an ability to estimate their relative magnitude for different surfaces.

Acknowledgements

I would like to thank my supervisor, Dr. S.C. Parker, for his encouragements and insights and, not least, for his patience.

I would also like to thank Pete and Graeme for their interruptions and alarums, and many other friends and colleagues for the advice and useful discussions I benefited from during this work.

Finally I wish to acknowledge the financial support provided by the Science and Engineering Research Council for this work.

Contents

Chapter 1

Introduction

One of the general aims of this work was to apply atomistic simulation techniques to model the surface structures and stabilities of a range of complex oxides. In this chapter are briefly reviewed the general aims of simulation, available experimental and simulation techniques - used previously in studying the surfaces of oxides, and finally the specific aims of this thesis.

1.1 The relationship of computer simulation to experiment

Ceramics can display a wide range of technologically useful properties, and yet our understanding of the detailed atomic processes which cause these desirable properties is often tentative. As a consequence attempts to design materials and to predict properties of new materials are often undertaken using a trial and error basis. In particular, many useful properties are found by manipulating the defect structure of these materials. Examples include electronic and fast-ion conductivity, corrosion resistance of oxide scales, sintering densification and grain structure, mechanical

properties such as creep rates and magnetic and optical properties. Measurements on the bulk material, while indicating properties such as total numbers of charge carriers or vacancies present, have provided little direct knowledge of the microscopic defect structure. The attempt to understand the properties of these important materials must be based on knowledge of atomic processes which are not easily observable, but these atomic processes are often amenable to simulation. One such approach is atomistic simulation which provides a powerful method for understanding the relationship between microscopic and macroscopic phenomena. Here, atomistic simulation can be used to support, modify or refute theoretical models of atomic processes. Once a theoretic model is developed, simulation can be used in tandem with experiment to clarify results and suggest mechanisms. The role of simulation thus changes with the development of the model, firstly to shed light on the relationship between the fundamental interactions between atoms and the gross properties and structure of the material, secondly to use that knowledge in explaining and interpreting ambiguous experimental data, and finally to predict results not accessible to experiment.

This range is reflected in the procedures used to develop models. The atomistic method starts from the premise that at the atomic level the interactions underlying both simple and complex materials are the same, though the macroscopic properties may differ greatly in complexity. The method must start with some

reliable data in order to establish the model, which includes not only the atom-specific parameters, but if necessary the form of the model. The data can be of a well-characterised material or derived from ab-initio calculations. In either case the properties used to derive the model must include the properties relevant to the type of predictions made by the model. In practice a wide range of data is sufficient to completely determine the parameters used.

One form of atomistic modelling which has the largest body of developed parameters for ionic materials, and thus well positioned to make predictions of complex solids, is static simulation. In this field the potentials for binary oxides are the most tested due to the ubiquity of oxide materials and the presence of good experimental data. These potentials may be used to extend the model beyond the structures they were fitted to in two ways; firstly by using the potential to model different structures, namely the local structures of point defects, interfaces and different phases; and secondly to apply the potential in conjunction with other potentials from different oxides to model extrinsic defects and more complex oxides.

1.2 Previous work

1.2.1 Experimental techniques

1.2.1.1 Introduction

Knowledge about the bulk environment gained from experiment usually gives us averaged properties of materials such as average structures and concentrations. For example X-ray diffraction experiments can elucidate the bulk structure and determine site occupancies [Cheremisinoff (1989)]. A collimated beam of X-rays is diffracted by the periodic array of ions in the crystal lattice. From measurements of the angles of constructive interference the interlayer spacings of the ions, and hence the crystal structure, can be found to a high degree of accuracy. To obtain all of the reflections the angle of incidence is varied by either rotating the crystal, using a powdered sample or by using an incoherent source. Refinement of the experimental structure and electron density of manganese titanate performed with this method [Kidoh *et al.* (1984)], gave interatomic distances accurate to $1x10^{-3}$Å. The occupancies were determined, showing significant cation disorder. Although knowledge about local structures can only be inferred from these results using a microscopic model e.g.

assuming random distributions or clustering of defects, there are some techniques that can give insight into local structures, e.g. site selective laser spectroscopy could determine the local environment around defect species in the bulk. Electrical conductivity measurements have traditionally been used to determine defect concentrations by varying the pressure and temperature. For example electrical conductivity was used to measure the defect structure of strontium titanate [Balachandran and Eror (1982)]. The variation of conductivity with $p(O_2)$ allows the use of mass-action equations for defect equilibria, in determining the defects concentrations, however in practice there is often ambiguity due to the combinations of defects possible. For phase transitions calorimetry, differential thermoanalysis and high-temperature X-ray diffraction can give us the most information. High-temperature X-ray diffraction measures the change in crystal structure while the sample is heated through the phase transition. Calorimetry can measure enthalpies released during transformations of different phases to or from a common state, thus determining the enthalpy of transformation from one phase to the other. Calorimetric experiments performed on manganese titanate [Ross (1989)] found the enthalpy of the phase transition from the ilmenite to the lithium niobate structure at room temperature to be 8.359 +/- 2.575 kJ/mol, in agreement with phase equilibria measurements (5.3 +/- 1 kJ/mol). Phase transitions can be monitored using differential thermoanalysis

(DTA), which measures the different thermal responses of a sample and a reference material during heating. Differences which occur can also be related to chemical reactions, catalytic activity or adsorption processes undergone by the sample. However for investigation of heterogeneous catalysis and other surface-specific properties, surface-sensitive techniques are most effective.

1.2.1.2 Surface composition

There are many methods of surface analysis. Ion scattering spectroscopy (ISS) allows the atomic composition of the surface layer to be determined by measuring the energy of a reflected beam of ions. It is specific to the surface monolayer, unlike most surface spectroscopic methods, and if used destructively allows depth profiling for the first 3 or four layers. The surface area that is sampled is large, usually ~1 mm^2. A related method is secondary-ion mass spectroscopy (SIMS). This method, which samples the surface layer by analysing ions expelled from the surface under bombardment, is more sensitive than ISS and AES and gives isotopic and chemical information. The ionised atoms and clusters undergo mass spectrometry, allowing isotope resolution and a sensitive analysis (10^{-6} monolayer) of the first few (~5) surface layers [Cheremisinoff (1989)]. As with ISS the surface

analysis is destructive. The nature of reacting species on the surface of a catalyst cannot be determined by these methods, which require a vacuum to operate. Temperature programmed desorption (TPD) can be used under reaction conditions, and measures the identity and rate of desorption of species as a function of temperature from a catalyst which has been exposed to the reactant gases. Temperature programmed desorption was used [Bowker (1981)] to identify the formation of a formate intermediate on the polar surface of zinc oxide during methanol synthesis. The coincident hydrogen and carbon monoxide peaks in the desorption spectrum at 570K were taken as evidence of a common intermediate. Auger electron spectroscopy (AES) is an method of elemental analysis which can be used quantitatively, and is complementary to and often used in conjunction with X-ray photoelectron spectroscopy, giving information about the composition of near-surface layers. More specific techniques are available which can probe the structure as well as the composition of the surface.

1.2.1.3 Surface structure

Interfacial structure and chemistry influences the behaviour of most materials as grain boundaries often play the dominant role in determining transport mechanisms

and physical properties as well as chemical behaviour. In particular the efficacy of heterogeneous catalysts relates to the microscopic surface structure. Experiments can show which surfaces are involved in catalysis, and to a lesser extent how the surfaces interact with the reacting species. The most common methods of analysis are spectroscopic; involving the bombardment of the surface with photons, electrons or ions, and measurement of the energy of emitted particles.

1.2.1.4 Surface spectroscopy

For obtaining knowledge about the chemical environment and valence-band structure, X-ray photoelectron spectroscopy (XPS) and UV photoelectron spectroscopy, respectively, are commonly used. XPS measures the energy of electrons given off when the target is bombarded with X-rays. The electron is ejected from the core or inner-shell orbitals, thus the energy primarily gives information about the elements present, although a small chemical shift in binding energy can be observed. The electrons quickly lose energy from collisions with atoms, thus XPS gives information to a depth of about 10 Angstroms. Using X-ray photoelectron spectroscopy Goodby and Pemberton (1988) have shown copper exists predominantly as Cu^0 metal on mixed copper/zinc oxide catalysts, and using AES suggested it was

present as copper particles. A powerful method for determining the local structure around an atom is extended X-ray absorption fine structure (EXAFS). This measures the change in absorbance caused by interference due to back-scattered waves from nearby atoms when an electron is being excited. The interference yields path-lengths and thus distances to nearby atoms, providing local surface information. Details of intermediate reactants can be obtained using infrared spectroscopy and temperature-programmed desorption. Infrared absorption spectroscopy can measure electron transitions at a defect and electron-phonon coupling. Where paramagnetic species are involved electron-spin resonance can yield information, though this is less often applicable. Low energy electron diffraction (LEED) experiments - necessarily performed under ultrahigh vacuum - can provide structural information on uniform surface terraces and periodic arrays of defects, but the lateral spatial resolution of LEED limits the structural information which can be interpreted from local or aperiodic defects such as steps, ledges, facets and kinks. Reflection high energy electron diffraction (RHEED) can give detailed surface structure. Electron Energy Loss spectroscopy (EELS) resolves vibrational and electronic excitations, giving information on surface optical phonons. Scanning methods which enable resolution up to ~5A are scanning and transmission electron micrography. These methods require a conductive surface and can examine a wide range of detail (from micrometer

to nanometre) of surfaces and also grain-boundaries [Chaing and Yakagi (1990)]. Zinc oxide is used in the synthesis of methanol, but the nature of the active site is not known with certainty. A combination of scanning electron microscopy, X-ray diffraction and adsorption calorimetry were used by Bolis et al. (1989) to conclude that the surface defects, in particular steps and edges, causes the reactivity by providing coordinatively unsaturated zinc ions. The role of copper, added to improve catalysis, is uncertain. More recently developed methods resolving atomic-scale detail are atomic force microscopy (AFM) and scanning tunnelling miscroscopy (STM), although there is controversy about the effect of the probe on the surface. Scanning tunnelling microscopy on strontium titanate [Matsumoto et al. (1992)] showed steps corresponding to one unit cell height occurred on the (0,0,1) surface. AES can also be used as a scanning technique, called the scanning Auger microprobe (SAM), which achieves resolutions of about 1 μm. As well as surface analytic techniques, the morphology of single crystals often provides information on surface processes. Single crystal studies of zinc oxide show that different surfaces have distinct catalytic activity. The catalytic activity of zinc oxide samples of different crystallite morphology convinced Bowker (1983) that chemisorption occurred only on the (0,0,1) and (0,0,-1) surfaces. Studies on the morphology of barium sulphate and isostructural crystals [Buckley (1935), Davey (1991) and Benton (1993)] show ions

and molecules in solution adsorb differentially onto the distinct surfaces of the barite class, thus affecting growth. Both ionic strength and supersaturation have been shown to determine the growth rates of different surfaces of this material [Hopwood and Mann (1991)], allowing control of the crystal morphology by suitable choice of additives to the growth media.

The advent and improvement of surface sensitive optical techniques such as AES, SEM and LEED, and the introduction of STM and AFM has allowed more extensive experimental investigations of the role of impurities to take place. These techniques can now be coupled with atomistic simulations to give a better picture of the effects of both iso- and aliovalent impurities on ceramic bulk and surface properties.

1.2.2 Theoretical results

The theoretical descriptions of atomic transport traditionally used for the interpretation of experimental data are statistical theories, based on simple geometric ideas, e.g. assuming 'obvious' interstitialcy mechanisms [Kroger (1964)]. These ideas are most successful when dealing with highly ionic systems, and it has often been possible to verify the underlying assumptions, about defect structure for

example, , with careful experimental studies. When approaching more complex systems a quantitative theory of the properties of individual defects is required to lead us to the most appropriate model. The quantitative modelling of point defects in solids was introduced by Mott and Littleton (1938) who calculated the relaxation of a cubic lattice in response to a charged defect. However the modelling of crystals took off with the application of the Ewald method [Ewald (1921), Tosi (1964)] to determine the electrostatic potential in a crystalline environment (see chapter 2). Once the development of the HADES code [Lidiard and Norgett (1972)] allowed modelling of crystals, attention turned to determining other parameters for real systems, namely the ionic charges and non-electrostatic (short-range) interactions. One successful compilation of potential parameters for oxides was developed for a range of oxides by Lewis and Catlow (1985), allowing materials containing different cations to be modelled. The development of codes able to model surfaces and include the effects of ionic polarisability enables the effects of surface relaxation, step formation and segregation to be described [Mackrodt and Stewart (1990), Lawrence (1989)]. The algorithms underlying these codes are described in chapter 2. More recent models including the effect of temperature using the quasi-harmonic approximation, applied in the code PARAPOCS. One illustration of its application is the successful prediction of negative coefficients of thermal expansion of zeolites

[Tschaufeser (1992)]. With the establishment of reliable potentials and improvements in computing resources, atomistic simulation is increasingly being applied to more complex, less symmetric systems including grain boundaries [Davies (1992)], defect clusters [Cormack *et al.* (1987)] and adsorbed molecules [Titiloye, Tschaufeser and Parker (1992)]. The extension of atomistic simulation to new areas must be accompanied by an improved understanding of the strengths and weaknesses of our potential models, if we wish to have confidence in our predictions. Thus our models must first be tested against experimentally well characterised systems before they are used to model poorly understood properties.

1.3 Aims

The aims of this work are to extend the range of application of binary oxide potentials to model complex oxides, to determine whether potentials from different sources can be used together, and in particular to determine the extent to which static models can be used to predict thermal and kinetic effects. Although modelling time-dependent phenomena with static simulation techniques may appear surprising, activation energies of kinetic mechanisms can be calculated, and can in general determine the potential energy surfaces which all kinetic phenomena have to follow.

Additionally the knowledge of the thermodynamic equilibrium given by static simulation allows a more accurate judgement of which observed effects are kinetically controlled. Thus by modelling ternary oxides we can determine the equilibrium structure, which can demonstrate the extent of transferability of the potential, then by calculating defect and saddle-point energies predict which mechanisms will be active at finite temperatures. By modelling kinetic effects we can test the limits of applicability of the static simulation and determine the range of effects that can be modelled.

The modelling of zinc oxide, used as a catalyst in methanol synthesis, allows the calculation of equilibrium concentrations of defects, including surface steps. This helps us to understand the physical as well as catalytic properties of this material. The interaction of this oxide with an adsorbing molecule (in this case methanol) using a Monte-Carlo methodology shows how ionic and covalent potential models can be combined, and how the structure and energy of an adsorbing molecule can be determined based on a static model. Zinc oxide was chosen to model, as much experimental work is available on its catalytic properties in methanol synthesis, while there is still disagreement on the mechanism. Thus the simulation can determine firstly whether the predicted surface structures are in accord with experiment, secondly whether the calculated adsorption of the methanol follows experimental

data, and finally help determine the feasibility of the proposed mechanisms of catalysis.

Strontium titanate, which has the perovskite structure, has been previously modelled using parameters derived from an electron-gas calculation by Mackrodt and Stewart (1981), who calculated a surface relaxation significantly different to that seen experimentally. As a technologically important material and a model system for a very important class of compounds it is useful to determine our ability to model this using binary oxide potentials. The previous modelling of this material would additionally allow a comparison of the potentials and a test of whether the disagreement with experiment represented a limitation of the model when applied to perovskites or an inaccuracy of the experiment. Therefore we chose to repeat the calculation of the surface structure with empirical potentials derived from the binary oxides, thus testing the transferability of the binary oxide potentials for the ternary oxide bulk structure.

Manganese titanate is a member of the ilmenite family of minerals, and an X-ray determination of its structure [Kidoh *et al.* (1984)] shows significant cation disorder, and also suggests a manganese-manganese interaction due to proximity of the manganese ions, which is not present in the manganese oxide. Thus potentials derived from the binary oxides may be expected to have problems modelling this

material. This represents the first attempt to model the surfaces of ilmenite. The segregation of impurities to the surface can form surface phases, heavily influencing the character of the surface. Hence many technologically important properties may depend on the properties of very complex oxides formed as a surface layer. Furthermore it has recently been shown that manganese titanate undergoes a phase transition to the lithium niobate structure at high temperatures and pressures [Ross (1989)]. Thus the ability of the binary oxide potentials to model each of these structures is a stringent test of their transferability.

Crystal morphologies are determined by kinetic factors except for very small crystallites, yet static simulation can directly only determine the equilibrium morphology via the surface energies. However the surface energy does influence the growth rate of that surface, which determines the resulting crystal habit. The ability of static calculations to predict crystal morphology depends on the relationship of the actual morphology to the equilibrium morphology, and on the ability of the simulation to include kinetic factors. Barium sulphate crystal growth has been recently studied [Hopwood (1992)] as its precipitation is a major cause of scale. Its morphology is significantly affected in differing ways by the presence of various ions during growth from solution. Thus it is a good candidate for the modelling the effects of surface impurities on growth. The morphology of small crystals can be compared with the

calculated equilibrium morphology, while factors which have been proposed to affect growth rates can be calculated for each surface, thereby checking their relevance to the observed growth rates. Examining the growth of crystals from solution at varying supersaturations allow an effective separation of the influence of thermodynamic and kinetic effects on the growth. The ability of static simulations to predict both the equilibrium and kinetic factors controlling morphology can be tested to clarify our understanding of the mechanisms of growth. The simulation of barium sulphate requires the development of a potential for the polyanion, which has not been previously developed and can be determined empirically by fitting to the bulk structure. By simulating barium sulphate surfaces we can determine whether static calculations can be used to predict the morphologies of crystals in non-equilibrium environments.

Chapter 2

Theoretical Methods

2.1 Introduction

The methods used in this thesis are based on the theoretical approach of Mott and Littleton (1938), extended to cope with crystals of any symmetry, and use the Born model [Born and Huang (1954)] of solids to describe atomic interactions. That is, a solid is described as a periodic array of discrete ions, with forces arising from interactions between ions. The components of the lattice energy which are considered are, Coulombic or electrostatic interactions, short-range electron-electron repulsion, Van der Waals interactions, ionic polarisability and bonded nearest-neighbour interactions.

Apart from the Coulombic forces (including dipoles), these interactions are short-ranged and can be evaluated by considering a limited region of the crystal around each ion. The short-range interactions are discussed further in chapter 3. This chapter is concerned with the methods of determining the electrostatic forces within an infinite lattice of ions, and the application of these methods to model pure and

defective crystals.

2.2 The electrostatic sum in periodic structures

The Madelung energy of an ion or group of ions is the energy due to the electrostatic interactions of the ions with each other and the rest of the crystal. However the long-range nature of the Coulombic forces leads to some difficulties in determining this in practice: the energy due to a single interaction varies as 1/r (where r is the separation of the ions), but since the number of ions lying in a spherical shell of radius r is proportional to r^2, the net contribution of a shell of ions to the energy does not obviously decrease with distance. Thus it is not obvious that Madelung energies can be calculated simply by considering Coulombic interactions within a sufficiently large cutoff radius around the ion of interest. In fact an attempt to do this will yield wildly varying energies as the cutoff is increased. This is because the net charge of the sphere will also fluctuate, and it can been shown using Green's Theorem methods [Buhler and Crandell (1990)] that the method of estimating Madelung energies by considering increasingly large regions will give an energy that converges to the Madelung energy only if these regions have no net charge and dipole. Thus the Madelung energy of a lattice site depends on the gross morphology of the crystal as

well as the crystallographic structure. It is possible however that electrostatic energies could be determined by considering increasingly large neutral blocks of ions, but the convergence of this straightforward approach is slow and much faster methods are available which exploit the translational symmetries of the lattice. Somewhat different methods are required for two-dimensional and three-dimensional lattices, and these are discussed in sections 2.2.2 and 2.2.1 respectively.

2.2.1 The energy of the bulk crystal

In order to study infinite crystals it is necessary to apply periodic boundary conditions to a cell, usually taken as the crystallographic unit cell. If U(i,j) is the energy of interaction of an charge q_i with a lattice of point charges q_j, then the Madelung energy can be written as a sum over these interactions.

$$E_{Madelung} = U(\mathbf{i},\mathbf{i}) + \Sigma_{i \neq j} [\, U(\mathbf{i},\mathbf{j}) - \tfrac{1}{2} q_i q_j / r_{ij} \,]$$

where the subtraction is performed to avoid the double-counting of interactions in the unit cell. The electrostatic energy due to the interactions of ion ***i*** with ion ***j*** and its periodic images can be expressed as:

$$U(\mathbf{i},\mathbf{j}) = q_i q_j \Sigma'_n \, | \underline{r}_{ij} + n_1\underline{l}_1 + n_2\underline{l}_2 + n_3\underline{l}_3 |^{-1}$$

where q is the charge on the ion, $\underline{l}$ are the vectors determining the periodic cell, r is the interionic distance, and $\underline{n}$ ranges over $\mathbb{Z}^3$. The prime denotes that if $\mathbf{i} = \mathbf{j}$ the vector $\underline{n} = 0$ is excluded from the sum. This Coulombic contribution to the lattice energy can be calculated by exploiting the periodic nature of the crystal model. The sum over n can be calculated using a method originally due to Ewald (1921).

Given a Coulombic interaction between ions i and j:

$$\Psi(\underline{x}) = \Sigma_n \, 1/|\mathbf{A}\underline{n} + \underline{r}_{ij}|$$

where the matrix $\mathbf{A} = (\underline{l}_1,\underline{l}_2,\underline{l}_3)$ contains the lattice vectors and $n \in \mathbb{Z}^3$ specifies the periodic cell, then the expression can be rewritten using the identity:

$$1/r = 2\pi^{-1/2} \int_0^\infty \exp(-r^2t^2) \, dt$$

giving

$$\Psi(\underline{x}) = 2\pi^{-1/2} \Sigma_n \int_0^{\infty} \exp(-r_{nk}^2 t^2)\ dt$$

where $r_{nk} = |\mathbf{A}\underline{n} + \underline{r}_k|$

By subdividing the interval of integration we can write the interaction as the sum of two terms

$$\Psi(\underline{x}) = \Psi_1(\underline{x}) + \Psi_2(\underline{x})$$

where

$$\Psi_1(\underline{x}) = 2\pi^{-1/2} \Sigma_n \int_0^{\eta} \exp(-r^2 t^2)\ dt$$

and

$$\Psi_2(\underline{x}) = 2\pi^{-1/2} \Sigma_n \int_{\eta}^{\infty} \exp(-r^2 t^2)\ dt$$

The second term corresponds physically to the introduction of a neutralising Gaussian charge distribution around each ion. This charge neutralisation causes the

term to converge quickly with r i.e. become a short-range potential (which can be then be summed directly), and it can be expressed using the complementary error function, defined as:

$$\mathrm{erfc}(x) = 2\pi^{-1/2} \int_x^{\infty} \exp(-s^2)\ ds$$

Whence

$$\Psi_2(\underline{x}) = 2\pi^{-1/2} \Sigma_n \int_{\eta r}^{\infty} (1/r)\exp(-s^2)\ d\,s = \Sigma_n\, \mathrm{erfc}(\eta r)/r$$

The first term, denoting a periodic array of Gaussian charge distributions, can be evaluated by performing a Fourier transform:

Writing $I_1 = 2\pi^{-1/2} \int_0^{\eta} \exp(-r^2t^2)\ dt$

then

$$I_1 = 2\pi^{\frac{1}{2}} \int_0^{\eta} \int_{-\infty}^{\infty} (2t\pi^{\frac{1}{2}})^{-3} \exp(-K^2/4t^2)\ \exp(-i\underline{K}.\underline{r}) d^3\underline{K}\ dt$$

where $K^2 = |\underline{K}|^2$

Substituting $s = -K^2/4t^2$ gives

$$I_1 = \tfrac{1}{2}\pi^{-2} \int_{-\infty}^{\infty} (1/K^2) \exp(-K^2/4\eta^2) \exp(-i\underline{K}.\underline{r})\, d\,^3\underline{K}$$

Here we note that if I_1 is summed over all lattice vectors then

$$\Sigma_l \exp(-i\underline{K}.\underline{r}_l)$$

is zero unless $\underline{K}$ is 2π times a reciprocal lattice vector. Thus the integral can be rewritten as a sum over reciprocal lattice vectors. However if we sum over all lattice vectors we will include interactions we wish to exclude, namely the interaction of an ion with itself and the Coulomb-subtracted interactions such as the core-shell interaction, so this must be separately subtracted off, for which we use the identity for the error function;

$$\int_0^{\eta} \exp(-r^2t^2)\, dt = \mathrm{erf}(\eta r)/r$$

to give

$$\Psi(\underline{x}) = (4\pi/v_c)\Sigma'_K \ (1/K^2) \ \exp(-K^2/4\eta^2) \ \exp(-i\underline{K}.\underline{r}) - \delta_{ij}\mathrm{erf}(\eta r)/r + (1-\delta_{ij}) \ \mathrm{erfc}(\eta r)/r$$

where K is summed over 2π times the reciprocal lattice vectors, v_c is the cell volume, and δ_{ij} is one if there is no same-cell interaction, zero otherwise. The prime on the summation denotes that the $\underline{K} = \underline{0}$ term is not included, as charge neutrality ensures that this term is zero. The exponential decay of the interaction with K^2 ensures this sum converges rapidly in reciprocal space. The real-space component converges more rapidly as η increases, while for the reciprocal component convergence is improved by a small value of η, therefore its value is chosen to ensure both terms are calculated to equal accuracy.

2.2.2 Interfaces, surfaces and planar defects

Efficient mathematical methods for calculating the long-range Coulombic interactions over an slab, infinite in two-dimensions, has been developed by Parry (1985, 1976) who considered a limiting case of the Ewald summation. Heyes *et al* (1977) give a fuller treatment of the long range Coulombic potential and forces, including the effect of a resultant dipole moment perpendicular to the surface which

was initially neglected by Parry. By considering the crystal to be composed of a stack of planes, this method enables the calculation of the energies of free surfaces, grain boundaries and stacking faults to be made. Periodic defects at the interface can be introduced provided there is no net charge or dipole across the interface.

The coulomb contribution to the Madelung energy of the layer is given by;

$$U_{Madelung} = \tfrac{1}{2} \Sigma_i q_i \Sigma_j q_j \Sigma_{\underline{l}} 1/|\underline{r}_{ij} + \underline{l}|$$

where l ranges over two dimensions. Writing

$$V_{ij} = \Sigma_{\underline{l}} 1/|\underline{r}_{ij} + \underline{l}|$$

we can evaluate V_{ij} using the same integral form of $1/|r|$ used in the Ewald sum.

$$1/r = 2\pi^{-1/2} \int_0^{\infty} \exp(-r^2t^2)\, dt$$

which gives

$$V_{ij} = \Sigma_l 2\pi^{-1/2} \int_0^{\infty} \exp(-(\underline{r}_{ij} + \underline{l})^2 t^2)\, dt$$

Following Tosi (1964) by introducing a positive quantity G we divide the integration path into two parts (0,G) and (G,∞). This permits us to write V_{ij} as the sum of two integrals, as in the Ewald method:

$$V_{ij} = V_1 + V_2$$

where

$$V_1 = \Sigma_l 2\pi^{-1/2} \int_0^G \exp(-(\underline{r}_{ij} + \underline{l})^2 t^2)\, dt$$

and

$$V_2 = \Sigma_l 2\pi^{-1/2} \int_G^{\infty} \exp(-(\underline{r}_{ij} + \underline{l})^2 t^2)\, dt$$

We can transform the summation of the first term into reciprocal space by taking advantage of the two-dimensional periodicity of the plane, while the second is evaluated in real space. The reciprocal space part consists of two terms, a term

equivalent to $\underline{k}\neq 0$ and a $\underline{k}=0$ term. The $\underline{k}=0$ term can be neglected in the Ewald method due to the constraint that the charge distribution in the crystal must be neutral. For a surface the $\underline{k}=0$ term will always have a finite value, although in certain cases e.g. an unrelaxed $\langle 1,0,0\rangle$ MgO surface, it will be independent of the perpendicular distance u_{ij}. The magnitude of this term will be directly affected by the degree of relaxation i.e. the change in u_{ij}, at the interface, but it must be implicitly included in the relaxation.

Resolving the vector $\underline{r}_{ij}$ into two components, $\underline{u}_{ij}$ perpendicular to the interface and $\underline{p}_{ij}$ in the plane,

$$\underline{r}_{ij} = \underline{u}_{ij} + \underline{p}_{ij}$$

the reciprocal lattice contribution to V_{ij} is given by:

$$\Psi^G = \pi/A \left[-2u_{ij}\mathrm{erf}(Gu_{ij}) - 2(\exp(G^2u_{ij}^2))/(\pi^{\frac{1}{2}}G)\right] + (\pi/A) \Sigma_{k\neq 0}(B+C)\exp(i\underline{k}.\underline{p}_{ij})/k$$

where A is the area of the unit cell, and

$$B = \exp(ku_{ij})\ \mathrm{erfc}(k/(2G) + Gu_{ij})$$

$$C = \exp(-ku_{ij})\ \mathrm{erfc}(k/(2G) - Gu_{ij})$$

The upper interval of the integral gives the real space contribution to V_{ij}

$$\Psi^R = \Sigma_{\underline{l}}\ \mathrm{erfc}(G(\underline{r}_{ij} + \underline{l}))/(\underline{r}_{ij} + \underline{l})$$

The term V_{ii} is calculated by carrying out the real lattice summation without the singular term $\underline{l} = 0$, and by subtracting from the reciprocal lattice contribution the term $2G/\pi^{\frac{1}{2}}$ to remove the self interaction term.

The value of the Gaussian half width parameter, G, is determined by minimising the total number of terms in the real and reciprocal space summation to the required accuracy for the energy calculation. If the optimization is carried out for small u_{ij} where most of the work in the summation is done, the appropriate value of G is

$$G = (\pi/A)^{\frac{1}{2}}$$

2.3 Application of Madelung energies in theoretical methods

Determining the energy of a periodic structure allows us to gain information about using several different methods. The methods used in this thesis are energy minimisation, and Monte-Carlo. These are discussed in sections 2.3.1 and 2.3.2.

2.3.1 Energy minimisation

The minimum energy configuration determined from static calculations corresponds to the crystal structure at zero Kelvin, neglecting the zero-point energy. However, where empirically derived potential sets are used the parameters are implicitly already corrected for the effects of temperature at which the experimental data (used in fitting) was taken. Thus the apparently static model can shed light on room-temperature behaviours. Energy minimisation can be performed on any structure for which an energy can be calculated, however most practical methods used, including the ones described here, require at least the first and preferably the second derivatives of the energy to be given in addition. Here we describe the important features of the minimisation technique used in this thesis. The efficiency of

this approach allows us to consider large numbers of ions explicitly.

The general method of energy minimisation is a procedure for locating a configuration which is at an energy minimum, i.e. solving the equilibrium condition:

$$\partial U(\underline{x}) / \partial x_i = 0$$

This is achieved in this work using a Newton-Raphson variable matrix method which requires first and second derivatives in the minimisation procedure. It must be appreciated that with all gradient-based methods the minimum located is the nearest one to the starting point (or more accurately, contains that point in its basin of attraction). Where there may be several minima it is prudent to try a variety of initial configurations to sample more minima or confirm their absence. This feature can be exploited in the calculation of metastable structures and in determining relative stabilities of different phases. For most structures considered in this thesis the initial structure is close to the minimum, and the minimised structure can be seen to be unique from geometrical considerations. Confirmation of final structures is made by repeating calculations from several starting points.

To minimise the lattice energy $U(\underline{x})$ with respect to $\underline{x}$, we first expand U to second order [Born and Huang (1954)]:

$$U(\underline{x} + \underline{\delta}) \cong U(\underline{x}) + \underline{g}^T.\underline{\delta} + \tfrac{1}{2}\underline{\delta}^T.\mathbf{W}.\underline{\delta}$$

where δ is the displacement of a given ion, g is the force acting on the ion

$$g = \partial U / \partial x$$

and $\underline{W}$ is the second derivative matrix;

$$W_{ij} = \partial^2 U / \partial x_i \partial x_j$$

hence at equilibrium

$$\partial U / \partial x = 0 \cong g + \mathbf{W}.\underline{\delta}$$

from which we can approximate $\underline{\delta}$ as

$$\underline{\delta} \cong -\mathbf{W}^{-1}.g$$

The energy can thus be obtained by updating the coordinates by $\underline{\delta}$ over a number of iterations. The inherent difficulty lies in evaluating the second derivative matrix **W**, especially when considering surface calculations in which over a thousand variables are not uncommon. This problem is partially relieved by approximating the inverse of the matrix, then updating the approximation after successive iterations and only recalculating **W** after a set number of iterations.

$$\underline{\delta} = -\lambda \,.\, \mathbf{H} \,.\, \underline{g}$$

H, the Hessian is initially set to be equal to $\mathbf{W}^{-1}$ and λ is a linear parameter. Therefore for the k+1 iteration the new coordinate positions are given by:

$$\underline{x}_{k+1} = \underline{x}_k + \underline{\delta}_k$$

in which

$$\underline{\delta}_k = -\lambda_k . \mathbf{H}_k . \underline{g}_k$$

then by using an approximation developed by Davidson (1959) and Fletcher

and Powell (1963) the Hessian for the next iteration can be estimated by:

$$\mathbf{H}_{k+1} = \mathbf{H}_k - (\underline{\delta}_k.\underline{\delta}^T{}_k)/(\underline{\delta}^T{}_k.\underline{\delta}_k) - (\mathbf{H}_k.\underline{\delta}_k.\underline{\delta}^T{}_k.\mathbf{H}_k)/(\underline{\gamma}^T{}_k.\mathbf{H}_k.\underline{\gamma}_k)$$

where

$$\underline{\gamma}_k = \underline{g}_{k+1} - \underline{g}_k$$

Then from the new **H** and g, the $\underline{\delta}$ for the next iteration can be calculated. This approach therefore only requires recalculation of the first derivatives g and is much less time and memory consuming than recalculating the second derivatives every iteration.

Imperfect structures present a problem, as the periodic nature of the model is lost, and different methods must be applied depending on the nature of the defect. One approach is to superimpose a localised defect on the perfect structure and determine the response of the perfect structure, thus calculating the energy as a difference from that of the perfect structure. The problem of relaxation was overcome by Norgett (1974) by developing the technique of partitioning the crystal into two regions when considering bulk crystal defects. This has now become the routine

method for calculations on bulk defect energies. For extended defects, the Parry method (1975) for two-dimensional summation of the Coulomb interactions has been transposed by Tasker (1978) into a computer code, MIDAS, enabling the calculation of planar defects in ionic crystals. Point defects at ionic crystal interfaces present an additional set of problems which are related to the effect of the charged defect on the outer regions of the crystal and it's interaction with the vacuum. This has led to the development of a code, CHAOS, [Duffy and Tasker (1983)] to deal with these problems. The theory behind these computer codes is discussed below.

2.3.1.1 The bulk crystal

The periodic nature of the crystal allows calculations to be performed on a single translational unit or cell, by using periodic boundary conditions. If the energy is expressed in terms of two-body interactions φ, then the total energy of an ion i is given by the sum of these interactions over the whole crystal:

$$U_i = \Sigma_n \Sigma_j \varphi_{ij}(\underline{r}_{ij} + \underline{n}.\underline{l})$$

where n ranges over all triples of integers, and l is the matrix of lattice vectors.

The two-body interaction is separated into a Coulombic part and a short-range part. The Coulombic contribution is calculated via the Ewald method, and short-range energies are included for all interactions between ions (and their periodic images) occurring within the short-range potential cutoffs.

Since only one periodic cell must be minimised, the number of parameters to be adjusted are small compared to surface and defect calculations. The simplest approach is to calculate the minimum energy position at constant volume, by keeping the lattice vectors fixed and just minimising the ionic coordinates. In addition, minimising the energy with respect to the lattice vectors under a constant external pressure can also be performed. In each case minimisation is performed by a simple application of the Newton-Raphson iterative method; this requires the calculation of the first and second derivatives of the energy with respect to the coordinates as explained above. The iterative cycle continues until the gradients are smaller than a predetermined value, or a limit on the number of cycles is reached without finding a minimum. In a successful calculation the final co-ordinates represent a minimum-energy crystal structure.

The THBREL code implements this energy minimisation technique to determine lattice energies and ionic coordinates for a perfect crystal. Point defects can be introduced, but are then repeated throughout the crystal due to the periodic

boundaries. By constructing supercells of varying sizes, defects can be introduced at different concentrations and the defect formation energies calculated, and extrapolated to infinite dilution if required. However more efficient methods of determining defect energies for defect concentrations corresponding to infinite dilution exist and are discussed below.

2.3.1.2 Point defects in the bulk crystal

The methodology of partitioning the crystal under consideration into effectively two regions, an inner one which includes the defect and an outer continuum, is used both for bulk and interface problems. For the calculation of bulk defect energies the crystal is partitioned into three spherical regions around the defect, (i) an inner *region I* in which all the ions are treated explicitly in the relaxation, (ii) an outer *region II* in which the effect of the defect is estimated using a continuum approximation and (iii) an intermediate *region IIa* in which the ions are held fixed and interact with the ions in region I (see figure 2.3.1.2.1). Thus region IIa must have a width greater than the real-space cutoffs. The minimised bulk coordinates must be known in order to give initial coordinates for the crystal. The accuracy of this approach is reliant on the fact that the relaxation away from the bulk structure

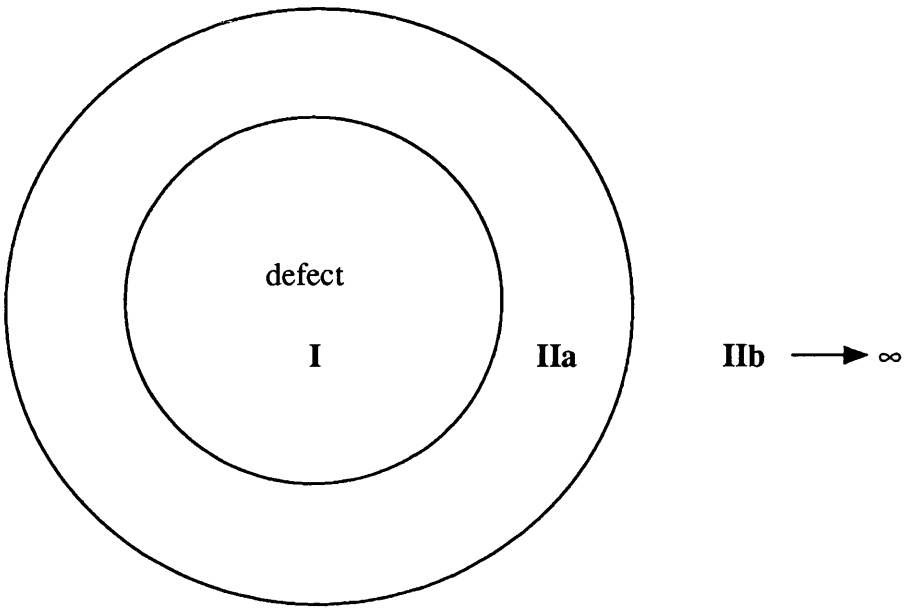

Figure 2.3.1.2.1: "Two-region" strategy for defect calculations. Region I is the explicitly relaxed region including and surrounding the defect. Region IIa is constructed for short-range interactions. Region IIb extends to infinity.

decreases fairly rapidly away from the defect. The interaction of region I with the outer part of region II is approximated to be the interaction between charge induced dipoles which solely involve the defect, and therefore region I must be large enough for this approximation to be valid. The defect energy is then the difference between the energy of the defect free or perfect lattice and the lattice containing the defect.

With this method the total energy of the system can then be written as the sum of three terms:

$$U(\underline{x},\underline{y}) = U_1(\underline{x}) + U_2(\underline{x},\underline{y}) + U_3(\underline{y})$$

where $U_1(\underline{x})$ is the energy of the inner region, $U_2(\underline{x},\underline{y})$ is the interaction between the two regions and $U_3(\underline{y})$ is the total energy of the rest of the crystal. $\underline{X}$ and $\underline{y}$ are vectors that represent the coordinates of the respective ions in regions I and II. $U_3(\underline{y})$ is approximated as a quadratic function of y for small displacements:

$$U_3(\underline{y}) = \tfrac{1}{2}\,\underline{y}^T . A . \underline{y}$$

Substituting this expression into the previous equation and assuming the equilibrium condition; y=*y* for equilibrium values of y, i.e. the forces acting on those

ions in Region II we have:

$$\partial U(\underline{x},\underline{y}) / \partial \underline{y} \,|_{y=y} = \partial U_2(\underline{x},\underline{y}) / \partial \underline{y} \,|_{y=y} + \mathbf{A}.\underline{y} = 0$$

leading to the following expression for the total energy $U(\underline{x},\underline{y})$;

$$U(\underline{x},\underline{y}) = U_1(\underline{x}) + U_2(\underline{x},\underline{y}) - \tfrac{1}{2}\partial U_2(\underline{x},\underline{y}) / \partial \underline{y} \,|_{y=y} \cdot \underline{y}$$

The defect energy can now be found by iteratively minimising the net force on each ion in region I until it is zero i.e.

$$\partial U(\underline{x},\underline{y}) / \partial \underline{x} \,|_{y=y} = 0$$

as the expression for the total energy $U(\underline{x},\underline{y})$ only contains terms which involve interactions with region I or those between regions I and II.

The treatment of the long range Coulombic interactions which extend into region II is via a continuum approximation developed from the classical polarisation theory of Mott and Littleton (1938). In this the displacements are due solely to the electric field produced by the total charge of the defect based at the defect origin. The

polarisation $\underline{P}$ at a distance $\underline{r}$ is thus given by;

$$\underline{P} = \tfrac{1}{4}\pi^{-1} (1 - 1/\epsilon_0) Ze\underline{r} / r^3$$

which leads to an r^{-4} interaction term in the energy which is reduced as the size of region I increases, note also the dependence on ϵ_0 (the static dielectric constant).

The theory outlined above is adopted in the CASCADE (**C**ray **A**utomatic **S**ystem for the **CA**lculation of **D**efect **E**nergies) code which is derived from the HADES (**H**arwell **A**utomatic **D**efect **E**valuation **S**ystem) code and optimised for the Cray series of computers.

2.3.1.3 Minimisation of interfaces

Efficient mathematical methods for calculating the long-range Coulombic interactions over an infinite crystal, developed by Parry (1976) and Heyes *et al* (1977), have enabled the development of a general-purpose program for calculating energies of free surfaces and interfaces between similar or dissimilar crystals. The surface simulation program requires the lattice vectors and the initial co-ordinates of

the ions and their shells, the cutoff values and the region sizes, and from this calculates the minimised positions of all the species in the interfacial regions.

On modelling surfaces two-dimensional periodicity is exploited to simplify the calculation. This is achieved by using a two region approach, the inner region I (which consists of the closest planes of atoms to the surface) is allowed to relax explicitly, whereas ions in the outer region II (the rest of the crystal) are fixed in the bulk structure, and allowed only rigid translations. For a calculation of, for example, a grain boundary two inner regions are placed together with two outer region on each side. A surface calculation has just one region I (surface) and region II (bulk). By repeating calculations with progressively larger regions, the sizes of the regions necessary for accurate derivation of the surface or lattice energy can be found. Subtracting the energy calculated using just one block, (representing the surface) from half the energy calculated using both blocks (modelling the bulk) yields the surface energy. This procedure is related directly to the definition of surface energy as the energy required to cleave a crystal.

The crystal is considered as a stack of planes and assumed to be periodic in two dimensions parallel to the interface. The relaxation of region I adjacent to the interface allows reconstruction of the surface by enabling the ions to relax to their equilibrium configurations. This surface region can include periodic defects, such as

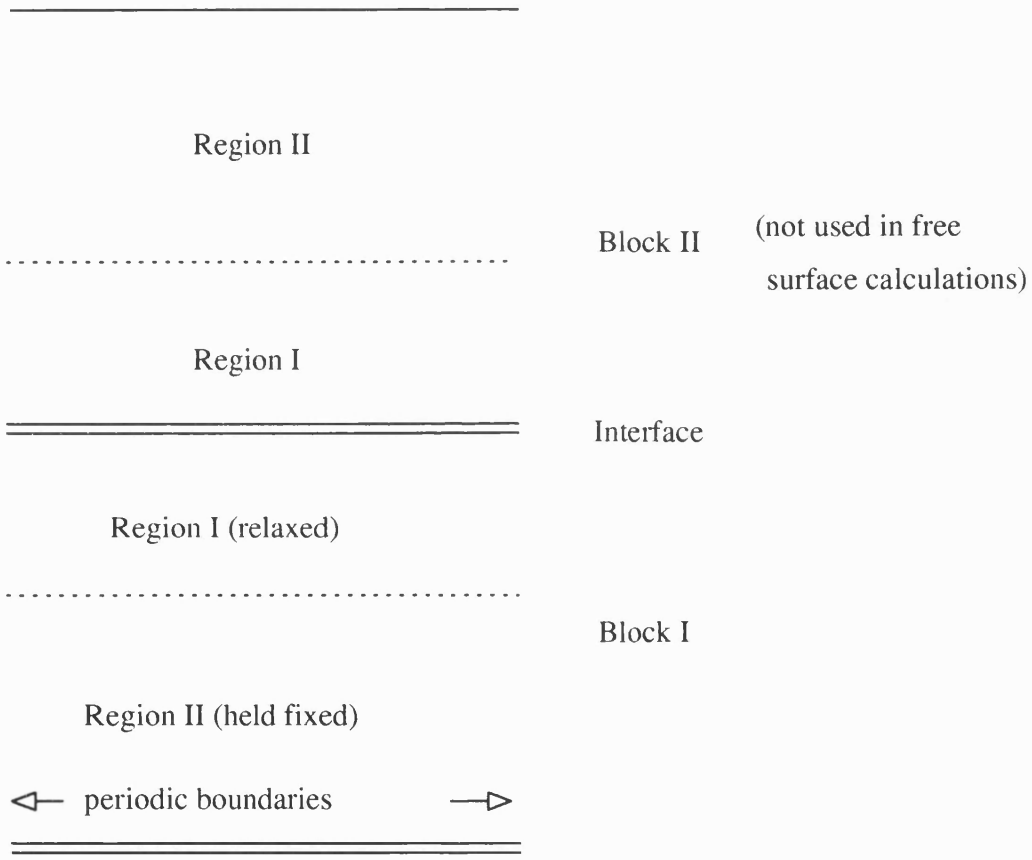

Figure 2.3.1.3.1 Schematic of crystal interface model

steps, vacancies or adsorbed molecules. Region II models the bulk environment, where the ions are held fixed relative to each other but the region may move as a whole. This allows for dilation or contraction of the crystal while ensuring ions in region I are constrained by the underlying bulk structure. The fixed region II implies that the surface vectors cannot change, thus energies calculated by this method are therefore energies at constant area.

The MIDAS (**M**inimisation of **I**nterfacial **D**efects **A**nd **S**urfaces) code [Tasker (1980)] which adopts the approach outlined above may be manipulated in a number of ways to generate stacking faults, twist boundaries and tilt boundaries. The inclusion of defects and impurities at the interface is only possible if the net charge of the defect or impurity is zero.

The interface or surface energy U^s per unit area can thus be determined by the sum:

$$U^s = \Sigma_{\lambda=1}^{m} [U(\lambda) - U(m)] / A$$

where U(i) is the energy of layer i, and i=1 is the layer adjacent to the interface while layer m is in the bulk environment.

In order to produce an equilibrated surface structure we have to calculate the

resultant force acting on ion i in region I due to its near neighbours. The component in the Cartesian direction $\alpha \in \{x,y,z\}$ of this force is given by the first derivatives of E_n with respect to $\underline{r}_i^{\alpha}$, the α component of $\underline{r}_i$

$$\frac{dE_n}{d\underline{r}_i^{\alpha}} = q_i \sum_{j \neq i}^{N} q_j \left(\frac{d\phi_{ij}^{G}}{d\underline{r}_i^{\alpha}} + \frac{d\phi_{ij}^{R}}{d\underline{r}_i^{\alpha}} \right)$$

where the reciprocal lattice contribution is resolved into two parts, one corresponds to the perpendicular component of $\underline{r}_i^{\alpha}$ ($\underline{u}_i^{\alpha}$), the other corresponding to the parallel component $\underline{p}_i^{\alpha}$

$$\frac{d\phi_{ij}^{G}}{d\underline{r}_i^{\alpha}} = \frac{d\phi_{ij}^{G}}{d\underline{u}_i^{\alpha}} + \frac{d\phi_{ij}^{G}}{d\underline{p}_i^{\alpha}}$$

with

$$\frac{d\phi_{ij}^{G}}{d\underline{u}_i^{\alpha}} = \frac{\pi}{A}\frac{\underline{u}_{ij}^{\alpha}}{u_{ij}}\left[-2\mathrm{erf}(Gu_{ij}) + \sum_{\underline{k}\neq 0} \exp(i\underline{k}.\underline{p}_{ij}(B-C)) \right]$$

$$\frac{d\phi_{ij}^{G}}{d\underline{p}_i^{\alpha}} = \frac{\pi}{A}\sum_{\underline{k}\neq 0} \frac{\underline{k}^{\alpha}}{k} \exp(i\underline{k}.\underline{p}_{ij})(B+C)$$

The real lattice contribution to the force is given by

$$\frac{d\phi_{ij}^{R}}{d\underline{r}_i^{\alpha}} = -\sum_{\underline{l}} \frac{\underline{R}_{ij}^{\alpha}}{R_{ij}^{2}}\left[\frac{\mathrm{erfc}(GR_{ij})}{R_{ij}} + \frac{2G}{\pi^{1/2}} \exp(-G^2R_{ij}^{2}) \right]$$

The Newton-Raphson method of minimisation used in MIDAS requires not only the first derivatives given here but also the second derivatives as given by Harding (1988).

2.3.1.4 Defects near interfaces

The inclusion of charged defects makes the calculation of point defect energies near interfaces more difficult than the calculation of the energies of extended planar defects. The CHAOS computer code (Computer simulation **HA**des **O**n

Surfaces) developed by Duffy and Tasker to deal with point defects at interfaces is based around the Hades code. As described earlier the point defect energies in a bulk crystal are determined by comparison of the energy for a perfect crystal with that obtained for the crystal containing the point defect. The perfect crystal energy and structure of surfaces is obtained from MIDAS. The spherical crystal region is then constructed as a series of circular discs lying parallel to the interface, with radii, which decrease with increasing distance from the origin.

The calculation of the defect energy is more complex and less efficient than in a 3-dimensional problem as the planes parallel to the interface must be summed explicitly. This is overcome by using the Parry method as in MIDAS. The calculation of the ionic displacements and the energy of the continuum (region II) must also be modified when there is an interface. In HADES the energy of the continuum is calculated by a discrete r^{-4} summation using the Mott-Littleton method, but this does not allow for any structural variation around the planar defect. In CHAOS the energy is calculated by a combination of a discrete sum of planar integrals around the interface and a volume integral over the remainder of the crystal. The planar integrals take explicit account of the dilation of the crystal at the interface. Thus:

$$E_{IIb} = -\frac{Q^2}{2}\left[\sum_{p\epsilon I,IIa} \sum_{k} q_k K_k \int_{(R_{IIb}^2 - r_b^2)^{1/2}}^{\infty} \frac{1}{(r^2+r_p)^2} 2\pi r dr \right.$$

$$\left. + \frac{1}{2}\sum_{k} q_k K_k \int_{R_{IIb}}^{\infty} \frac{1}{r^4} 4\pi r^2 dr \right]$$

where r_p is the perpendicular distance between the origin and plane *p*.

The other important consequence of charged defects at surfaces is the interaction of the defects with their image charges. When the interface is between two materials having different dielectric constants the image charge is given by [Jackson (1962)]:

$$q_i = q_{def}\left(\frac{\epsilon_1 - \epsilon_2}{\epsilon_1 + \epsilon_2} \right)$$

where q_{def} is the net charge of the defect. In general we shall only be considering free surfaces, therefore ϵ_2 is set to 1, the value for free space. The field due to the image charge must be included when calculating the displacements of ions in region II and the polarisation energy of region IIa. The image charge is situated half an interplanar spacing outside the last plane of ions as this is consistent with the method for calculating the energy of the outer continuum, where the polarisation is assumed to be caused by the total defect charge concentrated at the origin.

2.3.2 Monte-Carlo

The technique of Monte-Carlo is a method of determining thermodynamic properties based on the principles of statistical mechanics. If a system in equilibrium can be in one of N states, then the mean value of a property A is:

$$< A > = (1/Q) \Sigma_i A_i \exp(-E_i/kT)$$

where E_i is the energy of state *i* and Q is given by:

$$Q = \Sigma_i \exp(-E_i/kT)$$

However the average usually cannot be calculated by a direct summation. Any attempt to integrate over configuration space using numerical quadrature is futile for non-trivial systems due to the combinatorial explosion. Attempts to determine the average from Molecular Dynamics simulations often suffer from problems of ergodicity; that is, whether the system is constrained in a small region of configuration space by potential barriers. The average can be estimated with random

sampling, however the overwhelming majority of sampled points will carry very little weight due to their large energy. This however can be greatly improved with weighted sampling. Given L samples, suppose that state i occurs w_i often, i.e. w is the weighting function. Then

$$< A > = (1/L) \Sigma_{i \epsilon L} A_i / w_i$$

with $L = \Sigma_i w_i$

The variance of $< A >$ can be shown to be [Frenkel (1989)]:

$$\sigma^2_A = (1/L^2) \{ <(A/w)^2> - <A/w>^2 \}$$

This is at a minimum when $w_i \propto A_i$. Thus for thermal averages a weighted sampling system, such that states with larger Boltzman factors are favoured, is preferred. Ideally the weighting should be proportional to the Boltzman factor. The problem is then to be able to sample states in this proportion. Metropolis *et. al* (1954) developed an importance-sampling scheme which allows efficient sampling of this sort, by developing acceptance criteria for adopting new states derived from previously accepted states.

Considering a number of states, present in equilibrium proportions, then the number of transitions out of any state must be balanced by transitions in to maintain the equilibrium. The Metropolis algorithm makes the stricter "detailed balance" assumption that transitions between any pair of states are in balance. With the further assumption that the relative frequency of trial moves between two states is proportional to the states' relative abundance, then the equation

$$P_{ij} / P_{ji} = \exp((E_j - E_i) / kT)$$

holds, where P_{ij} is the probability of accepting a trial move from state i to j. The Metropolis algorithm defines the probability as:

$$P_{ij} = \exp((E_j - E_i) / kT), \quad \text{if } E_j \prec E_i$$

$$P_{ij} = 1, \quad \text{if } E_j \succcurlyeq E_i$$

which satisfies that equation. Other definitions have been used but have not shown much advantage. Thus the Metropolis algorithm proceeds as follows:

Make a trial move from the current state. If the energy of the new state is

lower than the current energy, accept the move and make this state the current one. Otherwise generate a random number uniformly in [0,1], and accept the new state if the number is smaller than the Boltzman ratio given above. If the trial move fails, the old state is sampled again.

Note that few restrictions are placed on how the trial move is generated, merely that trial moves can equally be generated in each direction between two states, however there are practical influences on it. If the trial move is largely unconstrained, then a large proportion of the moves will create high-energy states and will be rejected, requiring more trial moves to generate sufficient states. However if the changes allowed are small, more moves must be made to sample a reasonable amount of configuration space, and convergence of the statistics will be slow. Most find an move acceptance of 10%-50% to be a reasonable compromise [Allen and Tildesley (1987)].

Monte-Carlo techniques were applied in this work with the development of a program to model the physisorption of small molecules onto oxide surfaces. In our calculations the states were positions (translations and rotations) of the molecule on the surface of the oxide. The procedure was to generate new positions of the molecule by random movements, calculate the change of energy and then use the corresponding probability to decide whether to make the move according to the

Metropolis formula. Care must be taken to generate a uniform distribution of orientations. Further details of its use are given in chapter 4. The use of the Metropolis formula enables us to calculate average energies of adsorption and probable adsorption positions simply from the mean average of the states that are selected. The program was used for calculations of methanol on zinc oxide, but was developed in a general way so that different adsorbed species and substrate can easily be specified in the input. The main Monte-Carlo routine, used for generating configurations and selecting moves is given in Appendix A, and can easily be coupled with the THBREL suite of routines.

Chapter 3

Potential Models

3.1 Introduction

The modelling of simple ionic solids can be performed using quantum mechanical simulations of the solid state [Pisani (1988)], but for more complex systems, surfaces, and defects in crystals, atomistic simulation based on the Born model has proven to be highly effective [Born and Huang (1954)]. The solid is modelled as a collection of discrete ions interacting with each other. The manner in which the forces between the ions depend on the types and positions of the ions is given by the *potential model.* The potential model is defined by parameterised analytical expressions where the accuracy of its parameters are the most important factors in determining the validity of the results of the simulation [Jackson (1990)]. There are a variety of techniques used to obtain ionic potentials, which can be divided into two broad groups; namely empirical methods, and non-empirical or quantum mechanical methods.

3.2 The Born model of solids

The simulation techniques used in this work rely on the Born model of solids, which define the sum of the interactions between the ions which compose the crystal and can be used to determine the structure and properties of a crystal. We therefore need to model the interactions between individual ions to implement this model, and for this we use potential models which:

(1) give the interaction energy of any pair of ions as a function of separation of the ions and their type. This is divided into two components:

(a) an electrostatic interaction, for which the ions are usually considered to have their classical ionic charges; an exception to this is when dealing with complex anions, whose covalent character prevents this approach. The derivation of the electrostatic interaction is described in chapter 2.

(b) a short-range interaction, representing the mutual electron repulsion and dispersion interactions between the ions.

(2) allow non-central forces, parameterised as three- and many-body short-range interactions which may be required when dealing with, for example, water, silicates and hydrocarbons.

The expressions used to model the short-range potential used in this thesis

include the Born-Mayer exponential expression, representing the repulsion of overlapping electron clouds, and an additional attractive term, originally introduced by Buckingham, to model dispersive van der Waals interactions.

$$\varphi(r_{ij}) = A_{ij}\exp(-r_{ij}/\rho_{ij}) - C_{ij}r_{ij}^{-6}$$

This form of short-range potential is known as a Buckingham potential. The repulsive Born-Mayer term can be reformulated in terms of the ionic radius **a** and softness **b** of each ion [Gilbert (1968)].

$$\mathbf{V}(r_{ij}) = (\mathbf{b}_i + \mathbf{b}_j)\exp((\mathbf{a}_i + \mathbf{a}_j - r_{ij}) / (\mathbf{b}_i + \mathbf{b}_j))$$

The Buckingham potential does show a domination of the attractive term over the repulsive at distances much smaller than interionic separations, but this distance should not be accessible in most calculations.

Alternative expressions describing the non-Coulombic component of the pairwise interactions between atoms are

(1) The Lennard-Jones (12-6) or (9-6) form, given by

$$\varphi(r_{ij}) = \mathbf{B}_{ij} r_{ij}^{-12} - \mathbf{C}_{ij} r_{ij}^{-6}$$

or by

$$\varphi(r_{ij}) = \mathbf{B}_{ij} r_{ij}^{-9} - \mathbf{C}_{ij} r_{ij}^{-6}$$

respectively, which predate the Buckingham form and are still used for computational ease due to their very simple analytic form.

(2) The Morse potential, which is often used to described the pairwise interaction between covalently bonded atoms.

$$\varphi(r_{ij}) = \mathbf{A}_{ij}(1.0 - e^{-\mathbf{B}ij(rij - Cij)})^2 - \mathbf{A}_{ij}$$

This allows direct use of the equilibrium bond distance, potential well depth and force constant as parameters. Where a Morse potential is used for the pairwise interaction the angle dependant component of the covalent bond is given by a three-body term, expressing the restoring force as a harmonic function of angle.

$$\Phi_{ijk}(\Theta_{ijk}) = \mathbf{D}_{ijk}(\Theta_{ijk} - \Theta_0)^2$$

The lattice energy **U** of a crystal can then be expressed as the sum of pairwise and many-body terms over all ions in the crystal:

$$\mathbf{U} = \Sigma_{i \neq j} (\mathbf{q}_i \mathbf{q}_j / 4\pi\epsilon_0 r_{ij}) + \Sigma_{i \neq j} \mathbf{A}_{ij} \exp(-r_{ij}/\rho_{ij}) - \Sigma_{i \neq j} \mathbf{C}_{ij} r_{ij}^{-6} + \text{three-body} + \text{higher terms}$$

where $\mathbf{q}_i$, $\mathbf{q}_j$ are the charges of the ions, r_{ij} is the separation of the ions and $\mathbf{A}_{ij}$, ρ_{ij} and $\mathbf{C}_{ij}$ are parameters to be determined for interactions between ions of each type. Three-body terms may be required for modelling silicates and polyanions; torsional and higher terms are not usually included unless hydrocarbons are being modelled.

The Coulombic interaction can be calculated precisely for an infinite crystal using the Ewald summation technique [Ewald (1921)] discussed in chapter 2. The short-range potentials are used to calculate all pairwise interactions within the cutoff distance, which is usually chosen to be the distance for which the contribution of the short-range force is significant (shorter values cause discontinuities in the energy and its derivatives as ions cross the cutoff distance). Thus all central forces contributing to the Born model can be specified by giving the ionic charges, the values of the

short-range parameters and the short-range cutoff distance. As noted above the many-body terms are used extensively to model the angle dependencies in covalent systems and hence are restricted to relevant neighbouring ions. However in ionic and in partially ionic systems many-body interactions arise from the interaction of the ion charges with polarisable electron charge clouds. Hence the extent to which an ion is polarised will depend on its environment. The resulting non-central forces cannot be modelled as a nearest-neighbour bond due to the long-range nature of dipolar interactions. One of the most successful models for reproducing this effect is the shell model, discussed below.

3.3 Ionic Polarisability

The basic ionic model described above assumes all ions are unpolarisable, and for that reason has difficulties modelling properties dependent on the dielectric constant such as formation energies of vacancies and aliovalent defects. The most popular models which have been developed to model polarisability are the Point Polarisable Ion model, and the Shell model.

3.3.1 The Point Polarisable Ion model

Early attempts to include polarisation led to the development of the Point-Polarisable Ion (P.P.I.) model where the polarisability α of each ion is introduced as an additional parameter, allowing a point dipole to be induced by the local electric field. The defect energies calculated with this model are found to be too small [Norgett (1971)] because the model cannot take account of the distortion and movement of the electron clouds, thus tends to overestimates the polarisation energy. The polarisation energy of a pair of ions *i* and *j* with charges **q** and polarisabilities α at a separation **r** is given by [Moelwyn-Hughes (1961)]:

$$P(r) = (q_i q_j / 2r) [(\alpha_i + \alpha_j) / r^3 + 4\alpha_i\alpha_j / r^6]/(1 - 4\alpha_i\alpha_j/r^6)$$

This clearly leads to a catastrophic failure of the model when ions are within a distance **d** given by

$$\mathbf{d}_{ij} = (4\alpha_i\alpha_j)^{1/6}$$

Their interaction energy diverges, giving infinite polarisation. Subsequently

the shell model was used to model charge displacement explicitly, and as well as providing a more realistic picture, it does not fail in this manner. It has been widely adopted and has used in preference to the Point Polarisable Ion model in this thesis.

3.3.2 The Shell model

The shell model developed by Dick and Overhauser (1958) successfully describes the polarisation and the physical distortion of the ion in response to an electric field. The ion is assumed to be composed of a core, representing the nucleus and core electrons, and a shell, representing the outer electrons. The core and shell carry charges which sum to the ionic charge, and are connected by a harmonic spring with force constant $\boldsymbol{k}$, allowing polarisation of the ion. Therefore the polarisability α of the ion is given by

$$\alpha_i = \mathbf{Y}^2_i / (\boldsymbol{k}_i + \mathrm{r}_i) \quad \text{or} \quad \alpha_i \approx \mathbf{Y}^2_i / \boldsymbol{k}_i$$

where $\mathbf{Y}_i$ is the shell charge and r_i is the core - shell separation of ion i. The short-range forces are considered to act through the shell, thus the core responds only to the local electric field. No Coulombic forces act between the core and shell of the

same ion.

This simple model has shown itself to be adequate in modelling defects and surfaces despite its simple form. The polarisability may be thought to differ between bulk and surface sites due to differences in coordination number and Madelung potential, but previous calculations [Kenway (1991)] showed no advantage in tailoring the shell parameters to each environment.

A refinement of this model called the *breathing shell model* allowing harmonic variation of the ionic radius can account for Cauchy violations $C_{44} > C_{22}$, unlike the simple shell model, but otherwise shows little advantage over the shell model. A more recent development includes ellipsoidal distortions of the ion, allowing quadrupolar interactions [Healy (1993)]; this effect is significant with large ions such as sulphide and silver. These models have more parameters to be fitted and are computationally difficult to implement. In this thesis the unmodified shell model is used throughout.

3.4 Derivation of the short-range potential

The parameters required for the short-range potential may be obtained in two fundamentally different ways. First, by fitting the parameters so that calculated

properties reproduce the known crystal properties of the bulk crystal, i.e. the parameters are said to be derived empirically. Second is to calculate the interaction energies between ions directly with a minimum of reference to experimental work, here the parameters are said to be derived non-empirically. Each method has advantages which are described below.

3.4.1 Non-empirical methods

The non-empirical methods use approximate quantum mechanical calculations to determine ionic interactions. The most common approach uses the electron-gas approximation based on density functional theory to derive the potential between two ions. These interactions can be calculated for crystals for which there is little experimental data available, enabling parameters to be fitted to poorly experimentally characterised compounds, although in order to determine Madelung well depths assumptions about the crystal environment must be made. The electron-gas method uses density functional theory to determine the energy of the system from its electron density distribution. The electron density of the system is assumed to simply be the sum of the electron densities of the isolated ions, determined from Hartree-Fock calculations. This is a reasonable approximation for highly ionic crystals but in more

covalent systems where significant electron rearrangement occurs this approximation is not valid. A Madelung potential, calculated from the assumed or experimentally observed structure, must be included to simulate the crystal environment - this is particularly important for the oxide ion which is unstable in free space.

The calculated potential may be fitted to the form of a Buckingham potential or some other convenient form, or may be interpolated from the raw data. The dispersive interactions cannot be calculated with the electron-gas method and hence parameters for the shell model must be determined empirically where used.

It is more computationally expensive but increasingly common to perform Hartree-Fock calculations, usually with the self-consistant field formalism, on clusters of ions and then determine potential parameters from the calculated potential-energy surfaces. Problems lie in including the effect of the long-range Coulombic contribution correctly in small clusters, but the current development of periodic boundary SCF codes [Gillan (1989)] promises to overcome this problem.

3.4.2 Empirical methods

Potential model parameters derived empirically require good experimental data on crystal properties of relevant compounds. The cell dimensions, ion

coordinates, elastic and dielectric properties of binary compounds (usually oxides and halides) provide a reliable way of fitting the parameters as they are often well characterised, but the experimental error or disagreement between experimental sources may be too great to derive a unique set of parameters in which case additional data is required.

To find the parameters for an ion or set of ions, the computer model is implemented with trial values of the potential parameters, and the crystal properties calculated from the model are compared to the known properties of the compound. By repeatedly adjusting the parameters and comparing the calculated and experimental properties, an iterative procedure can adjust the parameters to minimise the difference between the calculated and known properties. Usually the final disagreement is well within the experimental error. Simple compounds are used to minimise the number of parameters to fit in one calculation, thereby improving the convergence of the procedure and stability of the final parameters. The relevance of the data to the parameters being fitted must be considered, for example the crystal structure of magnesium oxide is of no use in deriving shell parameters as the ion sites are centrosymmetric, hence there will be no ionic polarisation in the perfect crystal. The high frequency dielectric response would be most pertinent data for determining shell parameters, while the short-range parameters are most dependent on the detailed

structure, specifically nearest-neighbour distances.

Often assumptions are made which further restrict the degrees of freedom that are allowed. Usually small cations are assumed to be unpolarisable as the calculated polarisability is minimal. The model may be simplified further as the cation-cation short-range interactions are found to be negligible in most oxides due to the small cation sizes, hence are omitted. The accuracy of the calculated properties despite these restrictions shows the correctness of the model.

By fitting to bulk crystal properties we only sample the short-range potentials at discrete separations, and where interactions occur at distances closer than those found in perfect crystals, such as with many interstitial defects, we rely on the form of the potential to give the correct value. Comparison of the Buckingham potential form with the data produced by non-empirical methods [Kenway (1991)] shows the exponential term is a good choice for this region of the potential.

3.5 Potentials derived for molecules

When the surfaces of catalytically active ceramics are modelled, their interaction with molecules such as carbon monoxide and dioxide, methanol and small hydrocarbons is often of interest. Research into the properties of peptides and

proteins has also led to a need for a representation of the internal energy of larger molecules. These requirements have been met by the derivation of potential parameters for functional groups and bonds applicable to many molecules, by fitting to the properties of many small molecules including the observed vibrational frequencies, dipole moments and rotational barriers. The Morse potential is used for bonded interactions, with a harmonic term plus a periodic torsional term ψ modelling the bond-bending forces, where

$$\psi_{ij} = \mathbf{A}_{ij}\,(1 + \mathbf{s}_{ij}\,cos(\mathbf{n}_{ij}\Theta))$$

and Θ is the angle of torsion. A further harmonic term models out-of-plane bending of planar groups. In addition cross-coupling between modes is included - for example coupling of bond-stretching and angle-dependent modes.

The potential model of methanol used in this thesis used bond bending and stretching parameters from this derivation [Vetrivel *et al.* (1989)]. The coulombic forces were calculated using the charge distribution of the molecule determined from a geometry-optimised Hartree-Fock calculation. The non-bonded oxygen - oxygen short-range forces were taken to be the same between the methanol and oxide ions as for the oxide - oxide short-range interaction.

3.6 Potentials for oxides

The potentials for oxides used in this thesis all have the full ionic charges on each atom. This determines the long-range coulombic contribution to the potential, so as there are no three-body terms only the short-range potential remains to be found. Mixed oxide potentials require more parameters to be fitted than binary oxides while more experimental data exists for binary oxides, hence potential parameter sets are first derived for binary oxides. The potentials for mixed oxides are then derived from the potentials for binary oxides, as described below. This enables both the testing of the binary oxide potentials by predicting the mixed oxide properties and the determination of mixed oxide structures and properties in the absence of good experimental data.

3.6.1 Potentials for simple oxides

The short-range forces in ionic oxides are dominated by the cation - oxide and the oxide - oxide interactions. The small cation size usually means that the cations are too far apart to interact through short-range forces. If the oxide ion sites have

similar environments in different oxides, for example with octahedral co-ordination, the oxide - oxide interaction potential should be similar. This assumption was developed by Lewis and Catlow (1985) in which a Buckingham potential and a shell potential were assumed transferrable between many oxides, therefore when developing a new binary oxide potential with this potential only the cation - oxide interaction need be determined.

3.6.2 Potentials for complex oxides

This theme of transferability can be used for modelling complex oxides. By using a common oxide - oxide potential and neglecting cation - cation interactions, the parameters required to model complex oxides, which may not be well characterised, can be drawn from the component binary oxide parameters. For example, to model $SrTiO_3$, potential parameters are needed to model the Sr - O, the Ti - O and the O - O interactions, but these can be determined separately by modelling SrO and TiO_2. If the O - O potentials are the same, the potentials can be transferred directly to $SrTiO_3$. Therefore the development of transferrable potentials - those which can be successfully transferred from one structure to another - is an additional aim of the fitting procedure.

3.6.3 Use and Limitations of oxide potentials

The use of each potential should be limited to ions known to have the same valence as the fitted or calculated ion. Empirically derived potentials are restricted by the lack of good experimental data for many binary compounds. Non-empirically derived potentials must be used with a rigid ion model (i.e. without ionic polarisation), or must include empirically derived polarisability. Often rigid-ion models are developed for use in Molecular Dynamics calculations which can reproduce the static dielectric constant by fitting the short-range potential, despite this the rigid nature of the ions mean that the response of the lattice to charged defects will be inadequate. For ions which may have significant quadrupole moments a quadrupolar shell model will be required for accurate defect energy calculations.

Where the experimental data is obtained at room temperature, the empirical potentials implicitly incorporate the effects of that temperature on the structure, whereas the non-empirical potential should give the crystal structure at zero kelvin directly. Due to the inability to calculate the shell parameters, non-empirically derived potentials are only used directly where the rigid-ion model is acceptable, for example in modelling fluorides, otherwise they are combined with an empirical

derivation of the shell model parameters. Where experimental data is scarce, non-empirical methods are preferred, but for well characterised materials the empirical derivation is superior.

3.7 Potentials for the Inorganic-Organic interface

The interaction of small molecules such as methanol, or larger hydrocarbons in contact with oxide surfaces cannot be modelled using purely ionic potentials. However potentials for organic molecules which neglect all electrostatic components of the interaction are unable to model chemisorption adequately. For example the interaction of longer hydrocarbons with zeolite cavities requires a model of a covalent molecule with internal degrees of freedom interacting with an ionic framework. To model this the synthesis of potentials from the separate ionic and covalent potentials is required. One such approach which has been quite successful in a number of studies is due to Kiselev (1981, 1985).

3.7.1 Kiselev potentials

Potentials determined by Kiselev (1981) use the Lennard-Jones form to express the interaction of noble gases and small polar molecules at low concentrations with zeolites or graphitized carbon black. The Lennard-Jones potential parameters are calculated from the polarisabilities α and diamagnetic suseptibilities χ of atom **i** of the sorbed molecule and atom **j** of the lattice framework using the approximate quantum-mechanical Kirkwood-Muller formula [Kirkwood (1932), Müller (1936), Salem (1960)]:

$$\mathbf{C}_{ij} = -6\, m_e c^2 \alpha_i \alpha_j / \left((\alpha_i/\chi_i) + (\alpha_j/\chi_j) \right)$$

where m_e is the mass of the electron, and c is the speed of light. By substituting in the Kirkwood relation:

$$\chi = e^2 (a_0\, n\, \alpha)^{1/2} / (4\, m_e\, c^2)$$

where e is the electronic charge, n is the number of electrons in the atom and a_0 is the radius of the 1st Bohr orbit, we obtain

$$C_{ij} = {}^{3}/_{2}\ e^2\, a_0^{1/2}\, \alpha_i\alpha_j / (\alpha_i/n_i + \alpha_j/n_j)$$

for the r^{-6} term. The other parameter is calculated from the equilibrium radii **r** of the atoms involved.

$$\mathbf{B}_{ij} = {}^{1}/_{2}\, C_{ij} (r_i + r_j)^6$$

The polarisibilities and radii are taken from experimental data.

3.7.2 Applications to zeolites

When modelling zeolites each cation site was given a charge proportional to its occupancy. In order to obtain electroneutrality it was therefore necessary to assign partial charges to the framework oxygen ions. To model the electrostatic interaction of the framework with the molecule, the experimental values of the dipole and quadrupole moments of the molecule were used to assign a point dipole and quadrupole at the centre of the molecule.

The calculation of Henry's constants from this model gives values larger than

experiment, so Kiselev (1985) applied a fitting factor β to the adsorbate polarisabilities (and hence the same factor to the magnitudes of the Lennard-Jones short-range interactions) to obtain agreement with adsorption data. This was justified to overcome the inadequacies of the Kirkwood-Muller formula and the effects of the zeolite cavity on polarisibility. The values of β determined were close to unity and similar for different gases in the same zeolite, suggesting the values could be applied to other adsorbed molecules.

3.7.3 Limitations in use

The calculated heats of adsorption are nearly proportional to the polarisability of the adsorbate, hence the quality of the results depends closely on the quality of the experimental data or calculation determining the polarisability. The assumption that the short-range potential is independent of valence and that the Van der Waals radius is the same for atoms in different molecules has limited validity. Where molecules with internal degrees of freedom are modelled, the correct statistical calculations of adsorption energies require large amounts of computational effort. The testing of these potentials requires better experimental determinations of Henry's constants than are available at present.

3.8 Summary

The Born model, with its short-range and Coulombic components has been described. The Buckingham and Lennard-Jones forms of the short-range potential have been introduced. The need for polarisability was explained and the P.P.I. and shell models of polarisation have been compared. Both empirical and non-empirical methods of deriving potentials have been considered and the limitations and strengths of each have been described. The fitting procedure for simple and complex oxides was described. The development of potentials for molecules on oxides and in zeolites has been introduced. The derivation of each potential used in this work will be described in the section where the potential is introduced. In the following chapters the application of these models to a range of materials and their surfaces are described.

Chapter 4

Zinc Oxide

4.1 Introduction

The aim of the work in this chapter is to apply the techniques discussed earlier to model the surface structures and ultimately the reactivity of ZnO. However there is still considerable uncertainty as to the nature of the nonstoichiometric defects in ZnO and even whether ionic models are appropriate. Thus the potential models for zinc oxide are introduced and the bulk crystal properties are calculated and then compared with experimental results to test their reliability. Before considering the surface and the possible surface defects it is important to establish the relative energies of the defects in the zinc oxide bulk. These are calculated and compared with those inferred from experimental observations.

One of the major motivations for considering zinc oxide is its important technological application as a catalyst, chiefly used with copper. Hence the solution

energy of copper oxide in zinc oxide, and its segregation energy to the various surfaces was determined. As a first step in determining the selectivity of the zinc oxide surfaces to the physical adsorption of methanol, calculations are performed with an ab-initio potential derived for methanol [Titiloye (1991)] to calculate the adsorption energy and orientation of the molecule on the (0,0,1) surface. Although the work is still preliminary it represents the first inclusion of a Monte-Carlo module introduced into the CASCADE/THBREL suite of codes. Indeed in the simulation of inorganic solids community the use of Monte-Carlo methods is comparatively rare.

4.2 Previous work

The surfaces of zinc oxide are experimentally the most widely studied of the wurtzite semiconductors and provide a good base for comparison with theoretical calculations. ZnO polymorphs are of great technological interest - used for varistor devices [Cerva (1988)] as well as a catalyst in methanol synthesis [Frost (1988), Au (1989)]. In addition theoretical work by Jaffe, Pandey and Kunz (1991) suggests that the metastable rocksalt-structure phase may have interesting transport and optical properties useful for semiconductor devices. Zinc oxide with the zinc-blende structure

is stable at high temperatures and is observed in thin films [Liu (1986)] but in bulk is unstable with respect to the predominant low-temperature wurtzite structure.

Zinc oxide is widely used as a catalyst in methanol synthesis, but the mechanisms involved have not been unequivocally determined. The catalytic activity of ZnO has long been known to depend greatly on the method of preparation [Natta (1955)], and single crystal studies which have shown differences in the catalytic behaviour of different crystal planes suggest that the effect of the preparative techniques is to enhance the occurrence of specific surfaces. The zinc terminated (0,0,0,1) polar face of zinc oxide is considered to be the main source of activity in polycrystalline catalysts [Bowker (1983), Akher (1984, 1985)], with the reconstructed 2x2 surface important in carbon monoxide and hydrogen adsorption [Griffen (1982), Peng (1991)]. The addition of a copper component to improve the catalyst is common but its role in the catalysis is not well understood. There is still much controversy as to whether the active sites are (i) reduced copper particles with the zinc oxide acting only as a support [Chinchen (1984, 1986, 1987)], (ii) that dissolved Cu^{2+} in the zinc oxide is more important [Klier (1982)], or (iii) that the active sites are on ZnO and the copper is used only to act as a source or sink of charge for the reaction [Frost (1988)]. A more recent view is that the zinc oxide is only necessary to supply adsorbed

hydrogen ions to the copper clusters [Burch (1990, 1990)]. Even the existence of a synergy between the copper and zinc oxide is unclear.

Recent experimental efforts to determine the nature of the catalytic activity of zinc oxide surfaces have concentrated on the polar surfaces as the most likely area of activity. In particular Bowker and co-workers [Bowker (1981)] used temperature programmed desorption to identify that the formation of a formate intermediate on the polar surfaces is of pivotal importance in methanol synthesis. The coincident hydrogen and carbon monoxide peaks in the desorption spectrum at 570K are given as evidence of a common intermediate. The hydrogenation of this long-lived intermediate by mobile surface hydrogen atoms is postulated to give rise to formate species, then to methoxy species and finally methanol, which desorbs. Further work [Bowker (1983)] on samples of different crystallite morphology, which had different proportions of polar surface, convinced them that chemisorption occurred only on the polar surfaces. However, more recently Bolis *et al.* (1989) used a combination of scanning electron microscopy, X-ray diffraction and adsorption calorimetry to conclude that the surface morphology, including steps and edges, causes the difference in reactivity by providing coordinatively unsaturated zinc ions.

Separate confirmation of a common intermediate containing one carbon atom

in the synthesis of methanol and higher alcohols was given by the results of Elliott and Pennella [Elliot (1988)] who found this was required to explain the isotope mix in the product ethanol. When ^{13}C methanol was added to the feed of hydrogen and carbon monoxide over a mixed copper/zinc oxide catalyst, the occurrence of both doubly labelled and unlabelled ethanol implied a common precursor for methanol and ethanol synthesis.

Studies of both defective polar surfaces and the (1,0,-1,0) surface were performed by Au *et al.*(1988). Their conclusions were that carbon dioxide acted as a supplier of surface oxygen on polar surfaces, with both the dioxide and monoxide forming a surface carbonate structure that could be hydrogenated to formate. On the stoichiometric surface a surface carbonate was formed by carbon dioxide at room temperature, and heating yielded an adsorbed formate species that was stable up to 540K [Petrie (1990) and references therein]. Thus there is evidence that both surfaces may be active in methanol synthesis. Using X-ray photoelectron spectroscopy Goodby and Pemberton [Goodby (1988)] have characterised the oxidation state of Cu on the surface of a mixed $Cu/ZnO/Al_2O_3$ (33/66/1 % wt.) catalyst. After extensive reduction in a hydrogen atmosphere, the surface oxidation states of copper inferred from XPS spectral data were 93.0 % (+/- 5.0 %) Cu^0 and 7.0 % (+/- 5.0 %) Cu^{1+}. The

surface Cu/Zn surface ratio decreases from 0.28 to 0.13, which they suggested was due to segregation of copper particles. However, the changes produced by methane/steam reformation are more dramatic, with Auger and XPS data indicating a single oxidation state corresponding to Cu^0 with no Cu^{1+} present, or indicating a new physical structure with a Cu/Zn ratio of 0.17. Since hydrogen gas is more reducing than methanol/water and no attempts to exclude oxygen were made with the latter, these results suggest the presence of a separate Cu^0 phase.

There are several proposed mechanisms for the decomposition (and synthesis) of methanol over zinc oxide. The first step in decomposition is adsorption onto the surface, and dissociation of the hydroxyl hydrogen. For synthesis from carbon monoxide and hydrogen, the initial step is usually considered [Sengupta (1987)] to be the adsorption of CO onto an oxidised polar surface. The CO can then be desorbed at higher temperatures to leave anion vacancies [Bowker (1985)] which are the active sites for the chemisorption of CO_2 [Au (1988)] and subsequent reaction with H_2. It has been shown [Bowker (1988)] that none of the CO goes to form methanol directly. The intermediate species is probably formate [Bowker (1981)] which is pivotal for both methanol and ethanol formation [Elliot (1988)] and decomposition, and which has also been shown to be formed on the hexagonal plane [Au (1988)]. Although

modelling of the reactants at the ZnO surface is still beyond the scope of the simulation techniques, the calculation of the surface structures can be performed, in particular the reactivity of surface oxygen can be modelled and at least support or reject possible mechanisms.

4.3 The Perfect Crystal Structure

Before applying a model to the calculation of the defects and surfaces of zinc oxide, we must first be confident that it can model the perfect lattice accurately. Therefore the study of zinc oxide was started by calculating properties of the perfect lattice. Having calculated parameters of the perfect lattice, the defect structure was investigated by calculating the energies of various intrinsic defects in the bulk material and at various surfaces. The bulk defect structure of zinc oxide has been previously calculated by Mackrodt (1980) applying potentials derived using non-empirical electron gas methods with the Born model. The methodology is discussed briefly in chapter 3. Thus calculation of the perfect crystal also allows comparison of non-empirical and empirical methods. Surface energies of the low-index non-polar surfaces were calculated as detailed below, and the segregation

energies of copper to these surfaces were determined. Finally, the adsorption of methanol onto the catalytically active surface was modelled.

Initially two potentials were considered, from Parker (1983), and from Catlow and Lewis (1985), and from the comparison of the perfect lattice properties calculated in each case (see table 4.3.1), it can be seen that the agreement to experiment is similar for both. The Catlow and Lewis potential was chosen for these calculations, as the availability of other potentials from the same publication allowed the consistent calculation and comparison of defect energies.

The experimentally determined structure of zinc oxide is the hexagonal wurtzite structure, which is similar to the 'diamond-like' zinc-blende structure. If envisaged as layers of a buckled hexagonal net, wurtzite has 2 different layers A-B-A-B, shown in Figure 4.3.1, whereas zinc blende has 3 different layers A-B-C-A-B-C, shown in Figure 4.3.2. The zinc-blende structure has a higher (cubic) symmetry, though ions in both structures have the same nearest-neighbour environments.

The properties of zinc oxide were predicted for both the wurtzite and the zinc-blende (diamond-like) structure. Table 4.3.1 compares the two potentials' properties to experiment for the wurtzite structure. The properties for the zinc-blende

Figure 4.3.1 Wurtzite structure

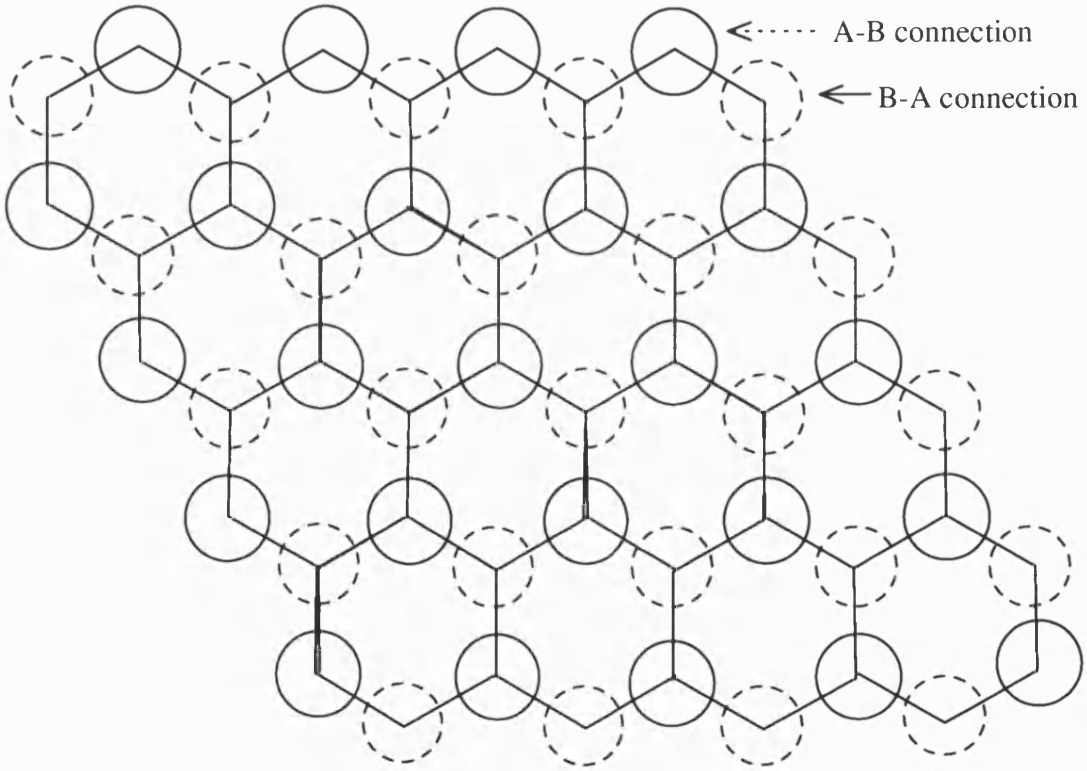

Figure 4.3.2 Zinc-blende structure

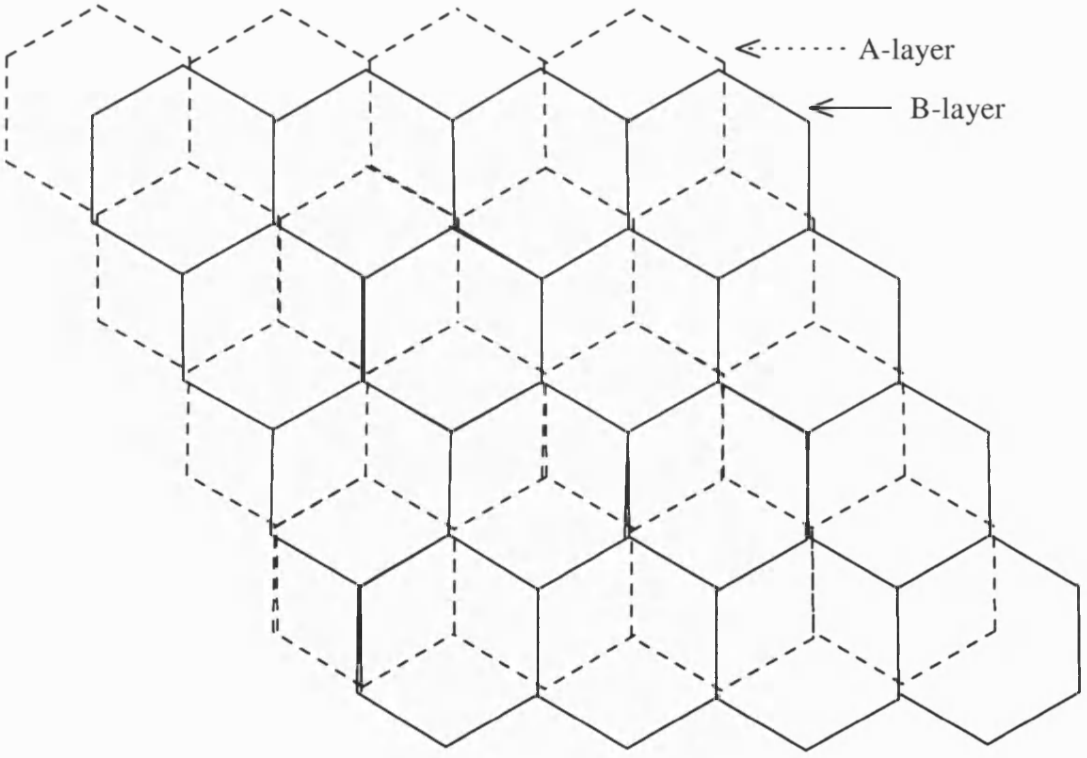

Table 4.3.1

Experimental and Predicted Properties

Experimental	Wurtzite(Catlow)	Wurtzite(Parker)	
Lattice Constant (Angstroms)			
3.2499	3.2499	3.2499	
Lattice vectors			
0.965 -0.259 0.000	0.960 -0.257 0.000	0.969 -0.259 0.000	
-0.259 0.965 0.000	-0.257 0.960 0.000	-0.259 0.969 0.000	
0.000 0.000 1.602	0.000 0.000 1.562	0.000 0.000 1.577	
Lattice energy (eV)			
-42.06	-39.65	-39.26	
Elastic constants (10^11 Dyne/cm-2)			
20.90	23.76	22.87	(1,1)
12.00	9.50	9.07	(1,2)
10.50	8.54	8.16	(1,3)
21.80	21.48	20.77	(3,3)
4.41	7.66	7.39	(4,4)
4.43	7.13	6.90	(6,6)
Static dielectric constants			
8.67	7.84	7.97	(1,1)
11.26	11.07	11.28	(3,3)
High frequency dielectric constants			
4.05	2.56	2.53	(1,1)
4.12	2.69	2.65	(3,3)

polymorph were predicted using the Catlow potential, these are shown in table 4.3.2. The fact that the naturally occurring structure of wurtzite was calculated to be more stable than the zinc blende gives us confidence that the potential can differentiate between small changes in the geometry, particularly as the energy difference is very small. Zinc oxide does not normally adopt the zinc-blende structure, but it has been shown to be stable under high pressures. Zinc sulphide is found in both forms. This fact implies that the energies should be similar for both forms, in fact the zinc-blende structure has a calculated lattice energy only 0.085 eV more positive than the wurtzite (see tables 4.3.1 and 4.3.2).

4.4 Bulk defect properties

The formation energies of the dominant intrinsic bulk point defects were modelled. Previous calculations of the energies of these defects were unable to resolve their relative stabilities [Catlow (1982)].

Bulk point defect energies were calculated using CASCADE, which calculates the defect energy as described in chapter 2. The two different sites for each interstitial defect were investigated, i.e. one octahedral site and one tetrahedral site.

Table 4.3.2

Predicted Properties of the Zinc Blende Polymorph of ZnO

Lattice Constant (Angstroms)
4.5108

Lattice vectors

1.00	0.00	0.00
0.00	1.00	0.00
0.00	0.00	1.00

Lattice energy (eV)
-39.57

Elastic constants (10^11 Dyne/cm^2)

(1,1)	17.14
(1,2)	11.72
(4,4)	11.49

Static dielectric constant

(1,1)	8.67

High frequency dielectric constant

(1,1)	2.6

As the calculations were limited to a maximum number of ions that could be treated explicitly (Region I) the effect of region size on defect energies was also considered. The Kroger-Vink notation used in tables 4.4.1 and 4.4.2 describes point defects with the notation $\mathbf{A_B^C}$, where **A** is the species added or created, and **B** is the species replaced or site used; **C** shows the charge change relative to the non-defective crystal, a dash (') for each negative charge, and a dot (·) for each positive, with an X (^{X}) for a neutral defect. The letters V and i are used to indicate a vacancy or interstitial site.

For example,

V_{Zn}'' is a Zn^{2+} vacancy with effective charge of -2

$O_O^{\cdot}$ is O^{1-} substituting for O^{2-}, giving a net charge change of +1.

We can calculate the energies of Schottky and Frenkel defects (Table 4.4.2) using tabulated electron affinities and ionisation energies [Tasker (1979)] given in table 4.4.3. In these calculations we assumed that the polarons were small i.e. the electronic defects were located on one atom. However, given the small band width this may be a major approximation.

To determine, for example, the ($Zn_i^{\cdot}$,V_{Zn}') in Table 4.4.2, the following terms are required:

Table 4.4.1. CASCADE defect calculations on zinc oxide

Defect Type	E_{def}(kJ/mol)	Kroger-Vink Notation
Octahedral O^{2-}interstitial	-1458.67	O_i''
Tetrahedral O^{2-} interstitial	-1337.94	O_i''
Octahedral O^{1-} interstitial	1.99	O_i'
Tetrahedral O^{1-} interstitial	79.20	O_i'
Octahedral Zn^{2+} interstitial	-1384.13	$Zn_i^{\cdot\cdot}$
Octahedral Zn^{1+} interstitial	92.86	$Zn_i^{\cdot}$
Tetrahedral Zn^{2+} interstitial	-1257.50	$Zn_i^{\cdot\cdot}$
Tetrahedral Zn^{1+} interstitial	158.07	$Zn_i^{\cdot}$
O^{1-} substitution	1722.05	$O_O^{\cdot}$
Zn^{1+} substitution	1713.61	Zn_{Zn}'
O^{2-} vacancy	2261.02	$V_O^{\cdot\cdot}$
Zn^{2+} vacancy	2208.76	V_{Zn}''

Table 4.4.3. Energies required for defect calculations (kJ/mol) [Atkins]

Reaction	Name	Energy (kJ/mol)
$Zn^{1+} \Rightarrow Zn^{2+}(g) + e^-$	2^{nd} Zn ionisation energy	1734
$O^{1-}(g) + e^- \Rightarrow O^{2-}(g)$	2^{nd} O electron affinity	844
$^1/_2\ O_2(g) \Rightarrow O(g)$	$^1/_2$ (O-O) bond energy	248.5
$e^- + O(g) \Rightarrow O^{1-}(g)$	1^{st} O electron affinity	-141.1

a) The energy for a Zn^{1+} interstitial (from table 4.4.1), and

b) $Zn^{2+}_{(l)} \Rightarrow Zn^{2+}_{(g)} + V_{Zn}''$ [Energy of vacancy]

c) $O^{2-}_{(g)} \Rightarrow O^{1-}_{(g)} + e^-$ [- O^{1-} electron affinity]

d) $O^{1-}_{(g)} + O^{2-}_{(l)} \Rightarrow O^{1-}_{(l)} + O^{2-}_{(g)}$ [from table 4.4.1]

e) $Zn^{2+}_{(g)} + e^- \Rightarrow Zn^{1+}_{(g)}$ [- 2nd ionisation energy]

The formation of oxygen interstitials may be written as:

$$^1/_2\, O_{2\,gas} \Rightarrow O_i'' + 2\,h^{\cdot}$$

and zinc vacancies form as

$$^1/_2\, O_{2\,gas} \Rightarrow ZnO_{lat} + V_{Zn}'' + 2h^{\cdot}$$

Schottky defects are calculated to have the lowest energy of the intrinsic defects, but the high values for the energies suggest a very low intrinsic disorder. There does not appear to be any direct determinations of defect formation energies in the literature, although there is evidence for the type of defect found, i.e. zinc

interstitials [Cox (1987)]. The energies calculated for these defects are significantly higher than the other calculated and experimentally derived values [Mackrodt (1988), Kroger (1954)], shown in table 4.4.2.. This shows either a limitation of this potential, or the error in assuming small polarons. Thus the results suggest that although the model is reliable in giving the structure and energy of the bulk material, it will overestimate energies when modelling the electronic defects. The energies calculated suggest that in real samples the defects present will be dominated by extrinsic defects or due to non-stoichiometry. The energies calculated for the intrinsic defects do not represent the defect distribution of undoped zinc oxide, as the chemical potential of oxygen will vary with partial pressure (pO_2). Table 4.4.4 shows the calculated energies of defect reactions involving oxygen. At high pO_2 the intrinsic defects are dominated by holes assumed to reside on oxygen, while at low pO_2 the dominant point defects are zinc interstitials compensated by electrons on zinc sites. Zinc oxide is normally an extrinsic *n*-type semiconductor with several active donors; to examine the intrinsic defects measurements of the Hall effect on high purity crystals in a reducing atmosphere have been made, concluding that the mobile species are zinc interstitials [Hutson]. However for a stoichiometric crystal the Schottky defect should dominate

Table 4.4.2. Energies of various bulk defects (kJ/mol) per defect

Defect	Calculation*	Experiment*	Current work
$(V_{Zn}'', V_O^{\cdot\cdot})$	567	547	644
$(V_{Zn}', V_O^{\cdot})$	459	390	-
(V_{Zn}^x, V_O^x)	546	607	-
$(Zn_i^{\cdot\cdot}, V_{Zn}'')$	741	-	825
$(Zn_i^{\cdot}, V_{Zn}')$	430	426	673
$(O_i'', V_O^{\cdot\cdot})$	557	-	802
$(O_i', V_O^{\cdot})$	242	-	746

(*) Mackrodt (1988) and references therein

Table 4.4.4 Half cell defect reactions dependant on $p(O_2)$ per e' or $h^{\cdot}$

Reaction	Energy (kJ/mol)
$\frac{1}{2}O^{X}_{O} \Rightarrow \frac{1}{4}O_2 + \frac{1}{2}V''_{o} + e'$	654.81
$\frac{1}{2}ZnO \Rightarrow \frac{1}{4}O_2 + \frac{1}{2}Zn^{\cdot\cdot}_{i} + e'$	744.96
$ZnO \Rightarrow \frac{1}{2}O_2 + Zn^{\cdot}_{i} + e'$	1233.09
$O^{X}_{O} \Rightarrow O^{\cdot}_{O} + e'$	878.05
$\frac{1}{4}O_2 + \frac{1}{2}Zn_{Zn} \Rightarrow \frac{1}{2}ZnO + \frac{1}{2}V''_{Zn} + h^{\cdot}$	-332.74
$\frac{1}{2}O_2 \Rightarrow O'_{i} + h^{\cdot}$	109.39
$Zn^{X}_{Zn} \Rightarrow Zn'_{Zn} + h^{\cdot}$	-20.4
$\frac{1}{4}O_2 \Rightarrow \frac{1}{2}O''_{i} + h^{\cdot}$	-253.64
Most favourable complete reactions	
$ZnO + Zn^{X}_{Zn} \Rightarrow {}^{1}/_{2}\,O_2 + Zn^{\cdot}_{i} + Zn'_{Zn}$	1212.69
$O^{X}_{O} + {}^{1}/_{2}\,O_2 \Rightarrow O'_{i} + O^{\cdot}_{O}$	987.44

4.5 Perfect Surfaces

The catalytic activity of zinc oxide is intimately connected with the surface topology. The presence of steps and surface defects may play an important role, therefore knowledge of the surface energies of various surfaces may help us understand the different catalytic properties of zinc oxide prepared in different ways. The surfaces of ionic crystals have been classified by Tasker (1979) into 3 types:

(i) those which are composed of neutral stoichiometric layers in the plane of the surface;

(ii) surfaces in which the layers parallel to the surface are nonstoichiometric, usually leading to a net charge on the layer, but the layers can be grouped so that a periodic repeat unit with no net dipole can be formed; and

(iii) those in which the layers have net charges and the repeating unit always causes a dipole normal to the surface, whichever possible termination is considered i.e. for any choice of plane perpendicular to the surface cleaving the crystal - leading to a dipolar surface for a simple termination of the stacking sequence (see figure 4.5.1).

Figure 4.5.1 **Surface Types**

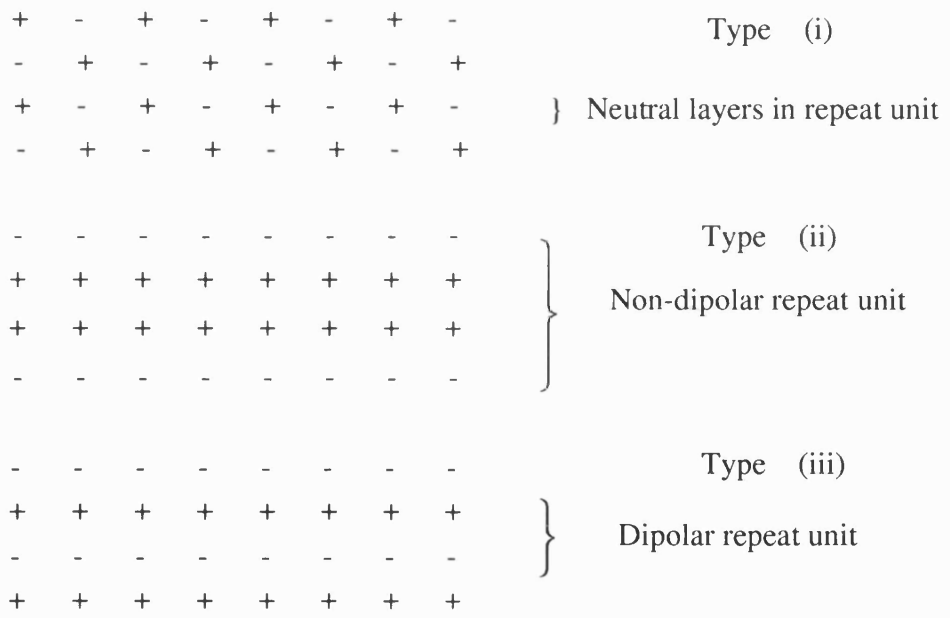

These different surface terminations are relevant because any dipole normal to the surface generated by the stacking sequence leads to a divergent surface energy, so is not acceptable. This is not a computational problem but a physical limitation. Therefore any potentially dipolar surface must have the dipole neutralised by compensating reconstructions, defects or adsorbed foreign species. Thus nominally dipolar surfaces can be simulated but because of the constraints on their relaxation and/or defects, are generally less stable. Type (i) surfaces do not create a dipole across the surface, these surfaces are generally the most stable of the three types. Type (ii) surfaces depend on the particular inter-layer separation to avoid a dipole. Thus these surfaces are more likely to create a dipole in the surface region on relaxation, which will cause a shift in the Madelung potentials throughout the crystal. These surfaces may be less stable than type (i) surfaces if the terminating layer contains an excess of relatively small unpolarisable cations, which are more destabilised by the surface environment. The least stable surfaces are type (iii) surfaces, as these require the introduction of defects and the disruption of the surface layer or large amounts of surface reconstruction to stay non-dipolar.

Zinc oxide surfaces are of type (i) for (*h,k,0*) orientations, and are of type (iii) when not parallel to the axis of hexagonal symmetry. The approach was to calculate

first the structures and energy of various simple stepped (*h,k,0*) surfaces as these in general will be most stable, and then consider point defects on these surfaces, finally model the (0,0,1) surface as the archtypal dipolar surface.

4.5.1 The (*h,k,0*) surfaces

Surface calculations were performed with the MIDAS computer code (see chapter 2), with several different region sizes. The surface energies, their relaxation, and hence the expected morphology of zinc oxide crystallites were determined from calculations of the low-index surfaces' structure. The calculation of the defect energies on these surfaces allow the defect structure of these surfaces and the segregation energies of the defects to be determined.

Surface energies were calculated from these results, and the energies of the simply terminated surfaces are shown in table 4.5.1. The energies vary in an erratic way, and the graph of energy versus distance in Figure 4.5.2 shows minima for step distances of about 5 and 8 Angstroms. These energies show a tendency towards an average value of 1.8 J/m^2 for larger step separations, but do not suggest a clear reason for the oscillating behaviour with distance. An examination of the surface structure

Table 4.5.1 Surface energies for 'levelled' steps

Index	Regions	Surface energy/Area (J/m^2)
(1,-1,0)	(5,10)	1.12
	(6,10)	1.12
(1,-2,0)	(7,20)	1.17
	(8,20)	1.17
(1,-3,0)	(6,18)	1.83
	(7,18)	1.82
	(6,16)	1.82
	(9,16)	1.82
(1,-4,0)	(10,20)	1.84
	(11,20)	1.64
	(15,30)	1.57
	(16,30)	1.57
(1,-5,0)	(10,20)	1.50
	(11,20)	1.49
	(12,20)	1.49
	(13,20)	1.48
	(15,30)	1.48
	(16,30)	1.48
(1,-6,0)	(15,30)	1.84
	(16,30)	1.84
(1,-7,0)	(15,30)	1.74
	(16,30)	1.74
(1,-8,0)	(20,40)	1.66
(1,-9,0)	(20,40)	1.81
	(21,40)	1.81

shows the large surface energies are caused by vacancies in the surface layer and isolated surface ions, present due to the method of generating the surface structure.

These surfaces do not contain the steps inherent in the hexagonal structure, but are calculated by taking all ions below a given height to give the most level surface, as the MIDAS program considers the unrelaxed surface to be an abrupt termination of the bulk structure (see Figure 4.5.3). As illustrated in Figure 4.5.3, this has the consequence of removing an ion at the top of the step (excluded ion) and leaving an under-coordinated ion below (added ion). The results (figure 4.5.2) show surface energies for these 'levelled' steps. However this does not give the most 'natural' termination as some of the surface ions are largely coordinatively unsaturated e.g. at the edge of the step, which may be important consideration for zinc oxide which is often thought to be a more covalent solid than the other first row transition metal oxides. Therefore we repeated the calculations on the more highly coordinated hexagonal steps.

The approach for increasing the surface coordination was to add explicit defects so as to obtain the simplified steps with fewer 'dangling bonds' (solid lines in figure 4.5.3). The relaxation of the steps is shown in Figure 4.5.6. The maximum displacement of an ion from its bulk position is 0.27 Å, which occurs on the exposed

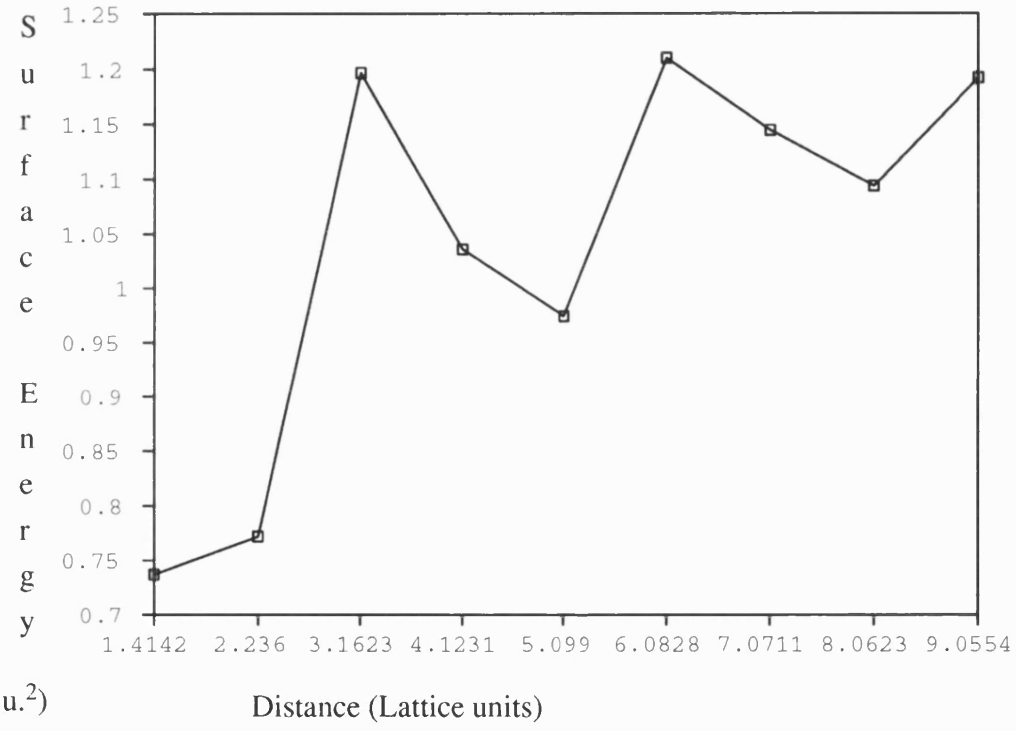

Figure 4.5.2 Plot of step distance against surface energy

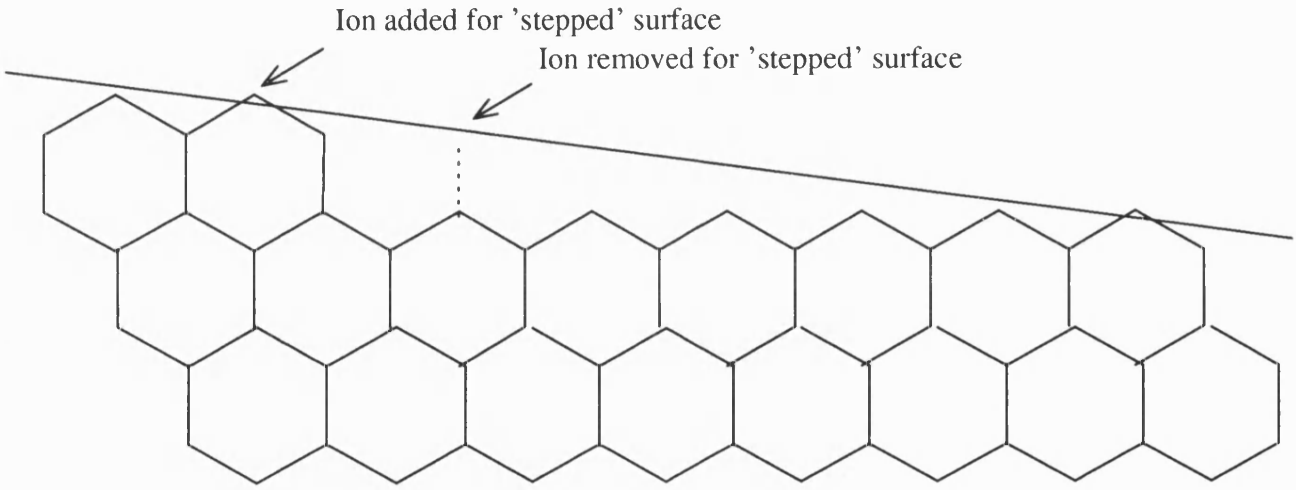

Figure 4.5.3 Difference between levelled and stepped surfaces

corner of an isolated step. Comparing this to the interionic separation of 1.95 Å, we can see this is a significant distortion of the structure. The results of the modified surfaces (Table 4.5.2) show lower surface energies (see Figure 4.5.4). The surface energies decrease slowly moving from the (1,-2,0) to higher index surfaces, as shown in Figure 4.5.4. The stabilisation of the stepped surfaces by removing unsaturated ions is striking. Instead of the surface energies varying between 1.1 J/m^2 and 1.9 J/m^2, the surface energies vary much more smoothly, lying between 1.1 and 1.2 J/m^2. The modified surfaces were stabilised by up to 0.66 J/m^2. The (1,-1,0) surface is the most stable, but the energies for different step separations are so similar to suggest that on the macroscopic scale the *(h,k,0)* surfaces will contain a mixture of these separations, i.e. clusters and widely separated steps. Indeed, the surface energies of these cuts with defects are sufficiently close (see Figure 4.5.5) that in addition to randomly separated surfaces there is likely to be a significant defect concentration, ideally suited for catalytic activity.

4.5.2 Step-step interactions

The corrected surface energies show a smoother and much smaller variation of energy with step distance than the 'sliced' surfaces and most importantly are more stable. There is a significant interaction between adjacent steps even at distances

Table 4.5.2

Surface energies with simplified steps

Index	Number c defects	Area (A^2)	Surface energy (J/m^2)
(1,-1,0)	0	16.37	1.14
(2,-1,0)	0	28.41	1.17
(3,-1,0)	1	43.41	1.17
(5,-1,0)	1	75.20	1.16
(7,-1,0)	2	107.63	1.16
(9,-1,0)	3	140.16	1.15

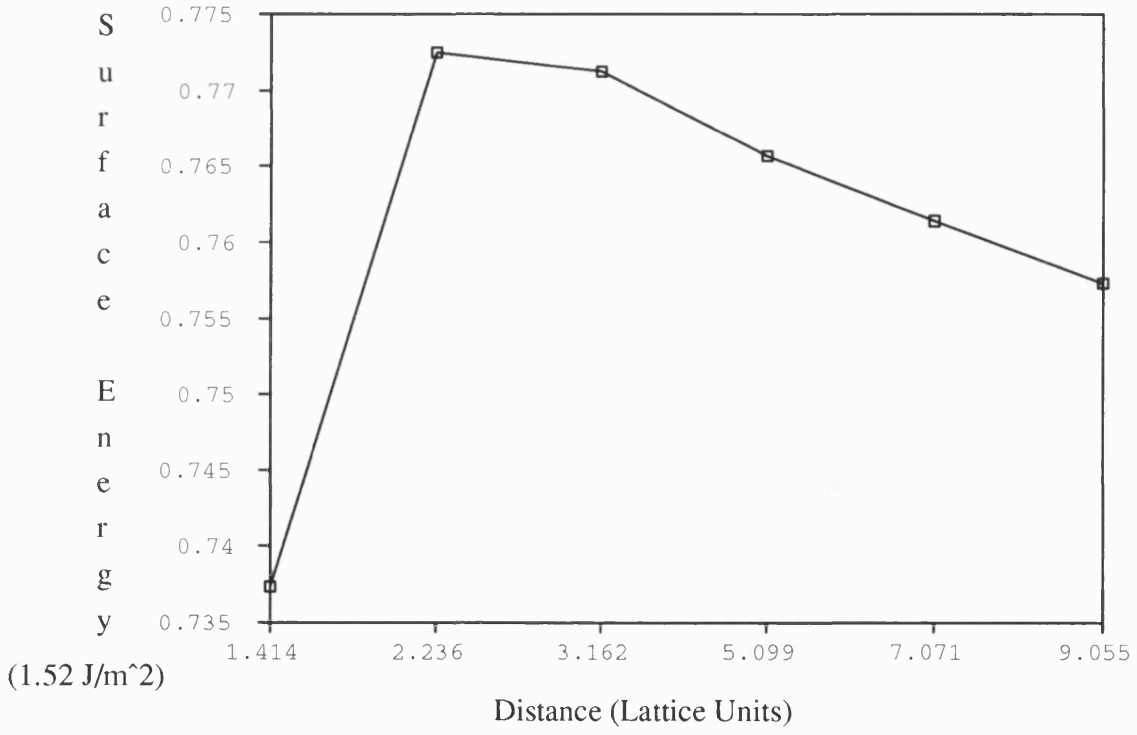

Figure 4.5.4 Plot of Surface Energy against Distance

Figure 4.5.5 Comparison of energies

'Sliced' and 'Stepped' surfaces

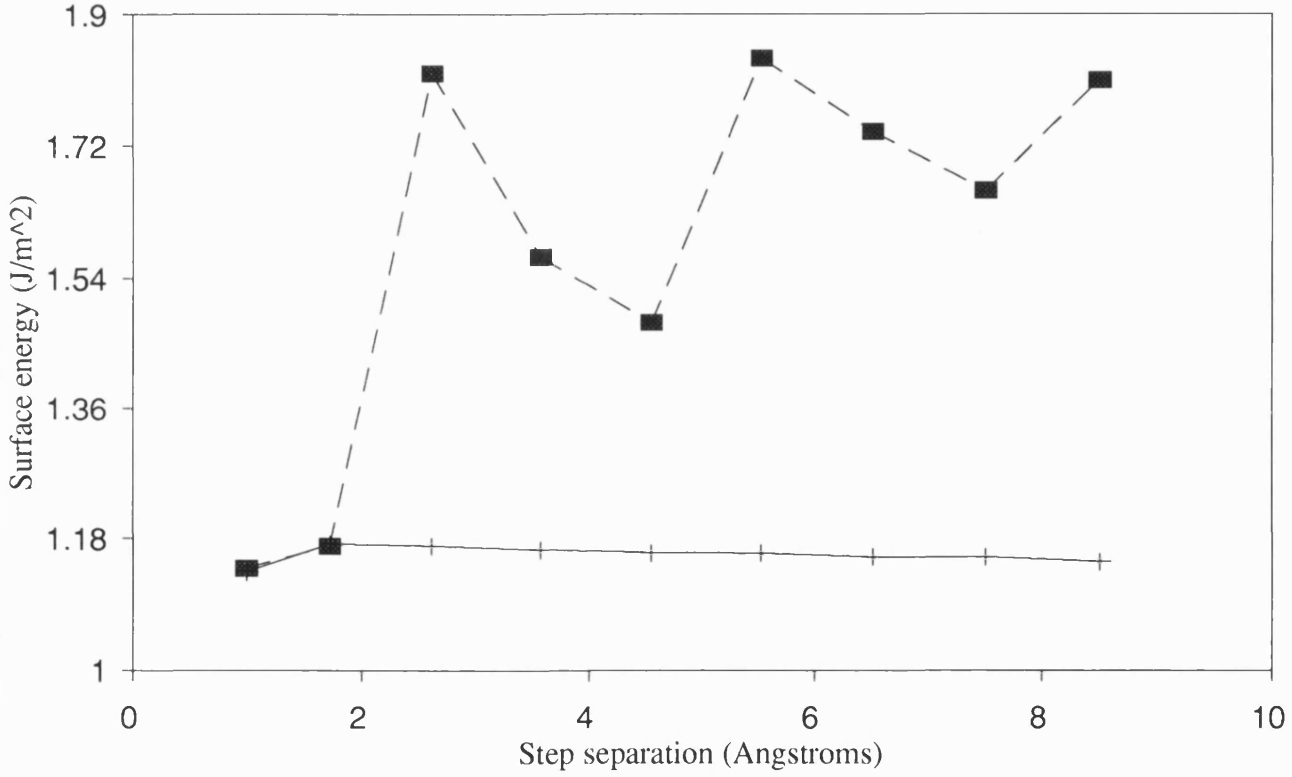

Figure 4.5.6 Relaxation of stepped surfaces (exaggerated)

a) (1,-2,0) surface

Maximum displacement = 0.24 Å

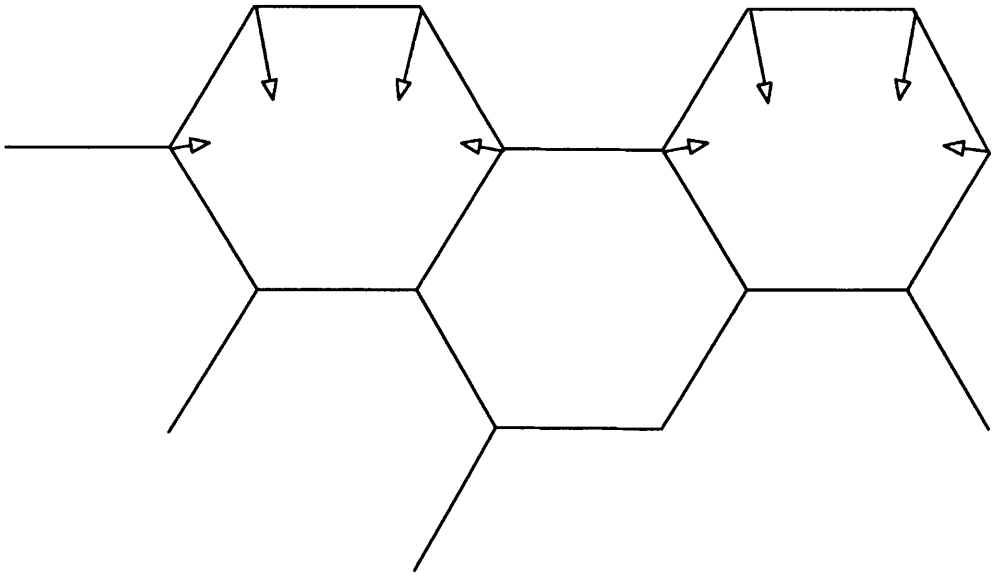

b) an isolated step

Maximum displacement = 0.27 Å

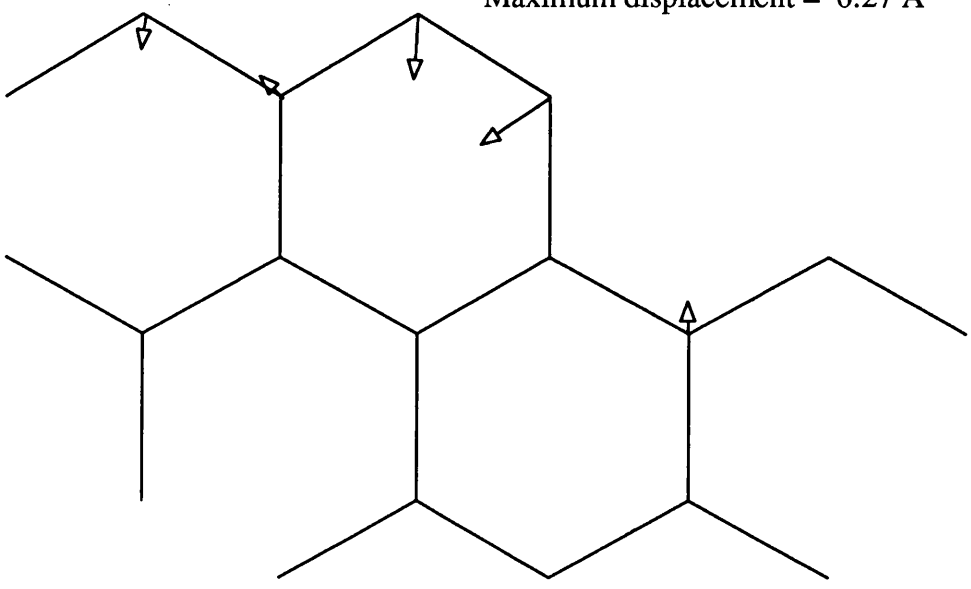

greater than 9 unit cells (~40 Angstroms), the computational limit. However even at this distance the energies show the approximately $^1/_r$ interaction of the steps expected at large distances. For surfaces with steps a distance **d** apart, at large distances the surface energy per unit area can be considered to be composed from 3 energies: the energy of the unstepped surface; the formation energy of the steps; and the energy due to interaction of the steps, where the latter two energies are per unit length of step:

$$E = E_0 + (E_f + E_i)/\mathbf{d}$$

where E_0 is the surface energy of the unstepped surface per unit area, E_f is the step formation energy per unit length, E_i is the step interaction energy per unit length and (1/**d**) is the length of step per unit area (the step density).

The interaction energy at large distances is inversely proportional to the step separation **s**:

$$E_i \approx k_i/\mathbf{s}$$

thus since the mean step separation equals the step density, we have

$$E \approx E_0 + E_f/\mathbf{d} + k_i/\mathbf{d}^2$$

The energy E_0 is obtained directly, and the values of the step formation energy E_f and the interaction parameter k_i can be determined from a series of surface energies at different step densities. The values derived from the above results are:

$E_0 = 1.14$ J/m^2,

$E_f = 1.47\text{x}10^{-11}$ J/m, and

$k_i = -1.45\text{x}10^{-21}$ J

Notice that the step-step interaction is attractive. The relative magnitudes of the interaction and formation energies can be judged by considering the (2,-1,0) surface, where the steps are 5.6 Angstroms apart. The equation suggests the step interactions contribute $-4.6\text{x}10^{-3}$ J/m^2 to the energy of this surface, while step formation adds $2.6\text{x}10^{-2}$ J/m^2. For the (9,-1,0) surface with steps separated by 27.6 Angstroms, the energies are respectively $-1.9\text{x}10^{-4}$ J/m^2 and $5.3\text{x}10^{-3}$ J/m^2. Thus the interaction energy has little effect even at close distances since it would only

dominate the step formation energy at distances of about $k_i/E_f \approx 1$ Angstrom. This would only be significant with high concentrations of steps. The step-step attraction also implies that the steps, if sufficiently common, will tend to be grouped in terraces on the surface rather than appearing in isolation. This prediction could be tested using atomic force microscopy.

4.5.3 The *(0,0,1)* surfaces

The dipolar (0,0,1) surface structure was next calculated assuming the presence of compensating surface defects to remove the dipole by modifying the repeat unit as shown in diagram 4.5.7. The charges of the terminating layers on complementary surfaces are adjusted using charged defects to create a non-dipolar repeat unit. The zinc oxide (0,0,1) surface is further complicated because on neutralising the dipole the modified complementary surfaces are not identical. This is due to the lack of a centre of inversion, S_n axis or mirror plane perpendicular to the *c* axis in the wurtzite structure so the defects introduced cannot be chosen to produce 2 similar surfaces, as can be done with other dipolar surfaces such as the (1,1,1) surface of NaCl-type crystals. Hence the total surface energy may be considered as the

Figure 4.5.7 Possible (*0,0,1*) surface compensating defects

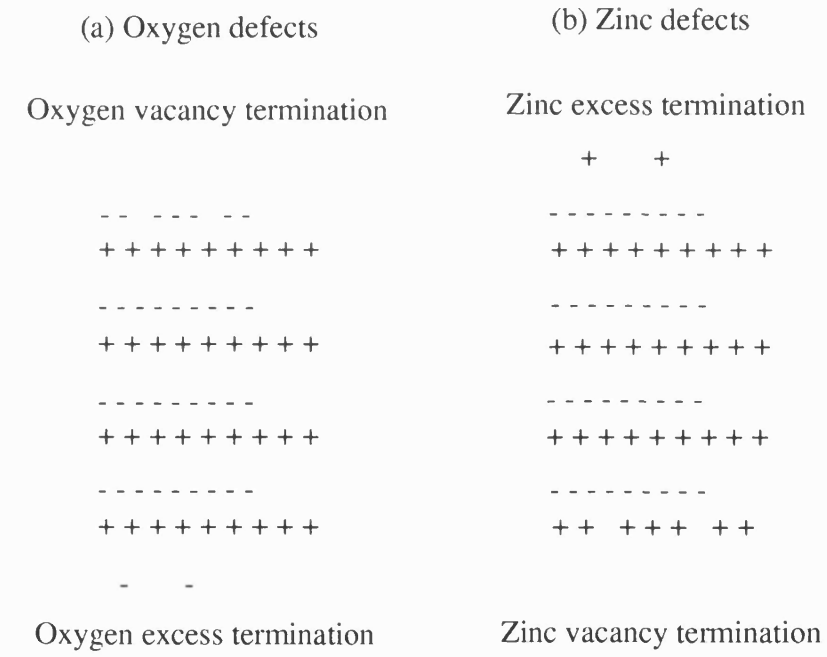

average of both terminations. Particularly as it may be anticipated that on the macroscopic scale each surface will be composed of 50 % of each.

The dipolar nature of the simple termination of the (0,0,1) surface necessitates the presence of charged defects to nullify the dipole which would otherwise cause divergence of the surface Madelung energies. The method chosen to introduce these defects was to choose the terminating surface layer to be only partially complete. The lack of a centre of inversion also means that the net defect charge required to remove the dipole is unlikely to be a simple fraction of the ionic charge. The charge required in this case is ≈ 0.22 of the ionic charge, thus requiring $2/9^{ths}$ of the surface layer to be removed. This is calculated by considering the dipole generated by one unit cell in the <0,0,1> direction, and then determining the charge that must be moved one periodic repeat distance in that direction to remove the dipole. Hence the charge depends on the relaxation and structural details of the crystal structure. Restricting the defects considered to vacancies, the required surface can be created in two ways; firstly by transferring zinc atoms from the zinc-terminated (0,0,1) surface to the oxygen terminated surface; or by transferring oxygen atoms from the oxygen-terminated surface to the zinc-terminated surface. The energies of these surfaces are shown in table 4.5.6. Two features are immediately noticeable; firstly

that the energies are significantly larger than for the non-dipolar surfaces; secondly that this reduced stability is almost entirely due to the energies of the surface with added ions, which are not adjacent to other ions in the same layer. It is plausible that the surface energy could be reduced if either the ions were allowed to form clusters or islands on the surface, which the small repeat unit in the simulation cannot model, or if these 'excess' ions could be replaced by defects *within* the terminating layer. Therefore the calculation for the oxygen-defect surfaces was repeated with each O^{2-} defect ion replaced by 2 Zn^{1+} ion substitutions in the zinc terminating layer and each O^{2-} vacancy replaced with an O^{1-} interstitial and an O^{1-} substitution in the oxide terminating layer. Together with the electron affinities given previously in table 4.3.3 the modified surface energy can be calculated and is shown in table 4.5.3 and is found to be far less stable than the vacancy stabilised surfaces. The greater stability of the vacancy-defective surface suggests that the catalytic activity of the polar surfaces, as with the step sites on (1,n,0) surfaces is due to the presence of coordinatively unsaturated ions; although the bulk defect calculations show that the relaxation around charged defects is underestimated in this model. The relaxed structure of the most stable oxygen-vacancy polar surface is shown in Figure 4.5.8. The exposed zinc ions, and the remaining oxygens on the surface have rearranged by moving sideways,

Figure 4.5.8

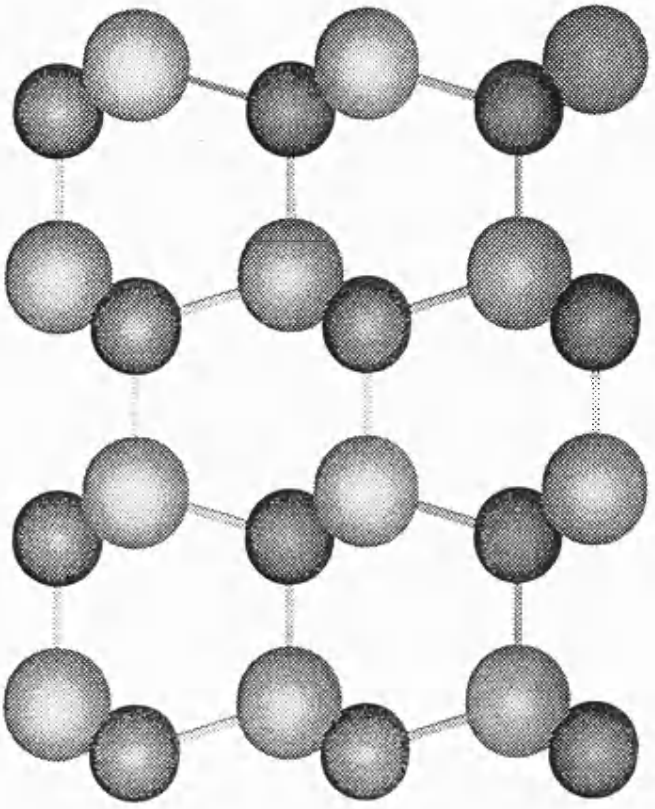

<0,0,1>

Before relaxation

(0,0,1) [oxygen vacancy] surface

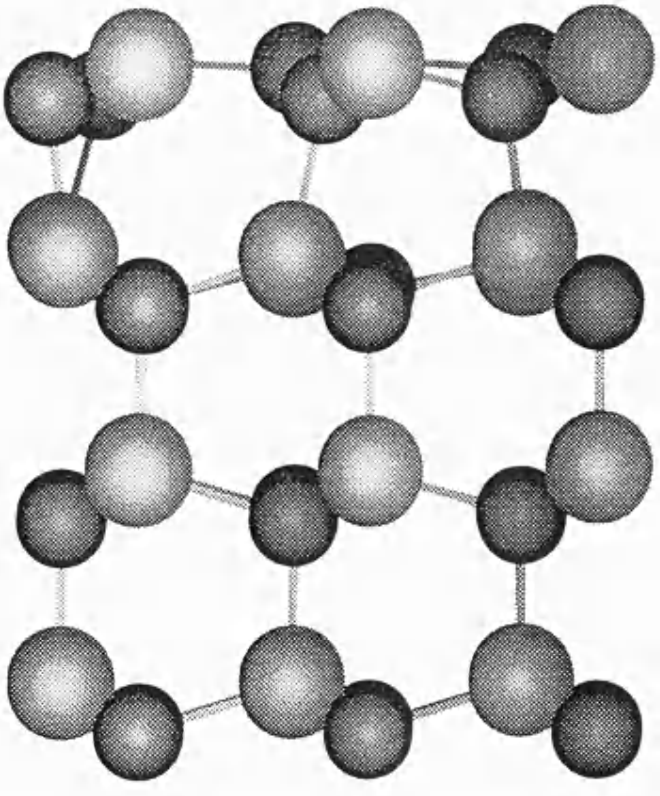

After relaxation

and the zinc ions in particular have been pulled downward. The largest movements are about 0.46 Å from the bulk positions, about twice the amount of relaxation compared to the non-dipolar surfaces. The energies of the possible surfaces given in Table 4.5.6 are $\approx$ 1 J/m^2 greater than those of the stepped surfaces, however this is probably an overestimate of the energy as the defects can form clusters, as mentioned about. Even with clustering this surface will be much more reactive than the prismatic faces, as there are a significant proportion of highly coordinatively-unsaturated ions present, which would otherwise only occur at step sites. The oxygen vacancies will be particularly important for the catalytic process of chemisorbing oxygen-carrying intermediates and reactants.

Comparison of the surface energies of the 'fully coordinated' steps with those where step sites are vacant suggests the source of the reactivity of the step sites, as identified by Bolis (1989), is that the difference in surface energies are comparatively small and that under reaction conditions they are likely to be accessed. This can be assessed by considering the point defect formation energy at the surface.

4.6 Intrinsic surface defects

The catalytic activity of the zinc oxide surfaces is often ascribed to the presence of defects at the surface. In particular the (0,0,1) surface must contain defects to neutralise the dipole, and is also the most catalytically active [Bowker *et al.* (1983), Klier (1982)]. The surface defects were calculated using the CHAOS code, which calculates defect energies assuming infinite dilution of the defect. The calculations were performed for several sites on the stepped and dipolar surfaces. Once the surface defect energies have been calculated, a comparison with the bulk defect energies tells us whether the defects will segregate to that surface and their concentration. The individual defect energies, shown in Table 4.6.1, are calculated with respect to isolated ions 'at infinity'. The solid-state equations detailed in that table suggest that the defect most easily formed at the surface is the Zn^{1+} substitution. From Table 4.6.1 it can be seen that the zinc and oxygen vacancies and the substitutions all have negative segregation energies to the non-dipolar surface (1,k,0) where k is odd. In contrast to the (1,2,0), surface which has positive energies, and the dipolar (0,0,1) which has a small positive, almost zero driving force. This is also reflected in the Zn^{1+} and O^{1-} substitution defects which show almost no segregation to

Table 4.6.1

Defect formation and segregation energies (kJ/mol)

Type	Defect site				
	(0,0,1)	(1,-3,0)	(1,-4,0)	(1,-5,0)	Bulk
Zn2+ vac					2201.64
Top site	2217.87	491.00	2287.35	420.45	
Seg. En.	16.23	-1710.64	85.71	-1781.19	
Niche	2217.87	917.24	2287.35	885.64	
Seg. En.	16.23	-1284.39	85.71	-1316.00	
Zn1+ sub					1721.23
Top site	1719.20	179.13	1689.35	42.05	
Seg. En.	-2.03	-1542.10	-31.88	-1679.18	
Niche	1719.20	472.95	1689.35	730.80	
Seg. En.	-2.03	-1248.28	-31.88	-990.43	
Ox2- vac					2254.94
Top site	2271.30	43.74	2319.12	43.74	
Seg. En.	16.36	-2211.20	64.18	-2211.20	
Niche	2271.30	1069.99	2319.12	1169.23	
Seg. En.	16.36	-1184.95	64.18	-1085.70	
Ox1- sub					1733.63
Top site	1727.41	390.75	1694.70	425.02	
Seg. En.	-6.22	-1342.88	-38.93	-1308.61	
Niche	1727.41	719.20	1694.70	719.20	
Seg. En.	-6.22	-1014.43	-38.93	-1014.44	

the dipolar surface, and have the most negative segregation energies to the non-dipolar surfaces (1,k,0) where k is odd, with the Zn^{1+} segregation favoured by about 200 kJ/mol. Thus under the reducing conditions conducive to Zn^{1+} formation this defect should dominate the prismatic surfaces. Furthermore these conditions should produce $Zn_i^{\cdot}$ defects (see Table 4.4.4). Thus we would predict that a negative surface charge due to $Zn_{Zn}^{'}$ defects on the prismatic faces will be balanced by a positive $Zn_I^{\cdot}$ space charge in the crystal at low pO_2. This is in qualitative agreement with observations. At high oxygen partial pressure the dominant defects are predicted to be $O_i^{'}$ and $O_O^{\cdot}$, leading to a positive surface charge due to oxygen substitution defects with a negative space charge due to oxygen interstitials. Clearly more calculations are needed, with other potentials to confirm these results.

4.7 Cu^{2+} impurities in the bulk and at the surface

The catalytic activity of mixed copper-zinc oxides could be due to islands of copper on the surface of zinc oxide, or sites of single substituted copper ions. Possibly clusters of copper ions could influence the catalytic activity of zinc oxide without playing a direct chemical role. The modelling of copper on low index

surfaces can tell us about the extent of segregation of copper, and any stabilization of defect surfaces that may occur. Under reaction conditions the species Cu^{1+} and Cu^{0} are active [Goodby and Pemberton (1988)], so segregation of these species could also be usefully modelled. However the preparation of these materials is to mix the divalent salts and once formed to reduce to Cu^{1+} and Cu^{0}. Thus we wish to identify the locations of the Cu^{2+} sites.

Calculations showed the two sites in Figure 4.7.1, labelled the 'niche' and the 'top' site, as being the most 'enclosed' and 'exposed' positions respectively for substitution of Cu^{2+} on stepped surfaces, these sites showing where coordination had the largest effect on the segregation energy, with other sites having intermediate energies.

The segregation energies for these sites on the various stepped zinc oxide surfaces were derived by the calculation of the bulk and surface energies separately, using the computer codes CASCADE and MIDAS respectively.

These results assume Langmuir behaviour (i.e. that there is no interaction between the defects) and a simple two-site model, with no intermediate sites or additional layers. The results show that segregation to the surface is generally favourable, with the exception of one site. Top sites are always preferred with

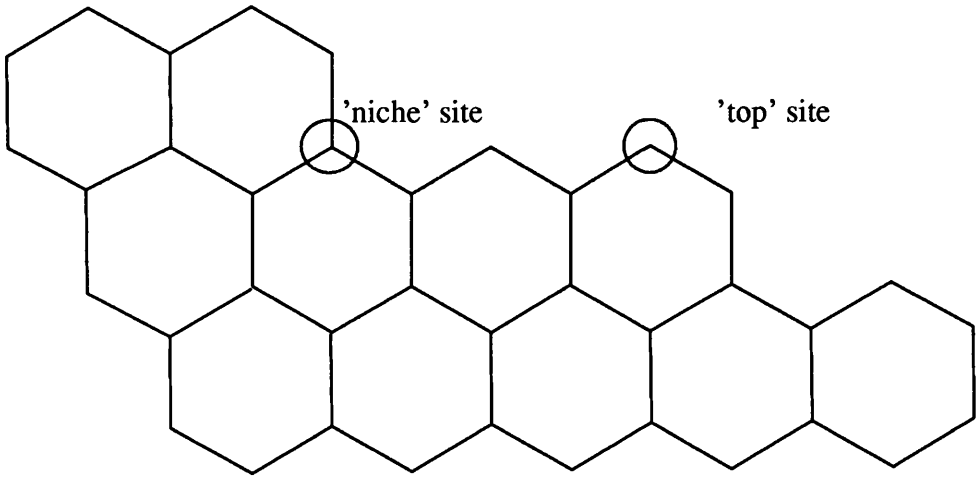

Figure 4.7.1 Substitution sites for copper on zinc oxide

segregation energies of about -60 kJ/mol, with the more favoured surfaces having the most closely spaced steps.

4.8 Segregation of Cu^{1+} to low index surfaces

A possibly active copper species is thought to be Cu^{1+}, so a comparison of the energy of formation of the Cu^{1+} and Cu^{2+} substitution defects and their segregation energies to the favoured low-index surfaces was made. The (1,1,0) and (1,-1,0) surfaces each contain two types of sites, as shown in figure 4.8.1. Note that when using hexagonal miller indices the surfaces (*1,k-1.0*) and (*1,-k.0*) are equivalent. Thus (*1,1.0*) and (*1,-2.0*) represent the same surface. The formation energies of substitution defects at the upper and lower sites were calculated using CHAOS, for each surface and each ion type, and the segregation energies determined by comparison with the bulk defect formation energy calculated using the CASCADE code. The extent of relaxation around the defect accounted for a stabilization of the final defect by about 600 kJ/mol for all of the cuprous ion defects but the cupric ions were stabilised by under 20 kJ/mol. However the segregation energies for all cuprous ion defects showed large positive segregation energies. Copper ions will segregate to the most

Table 4.7.2

Segregation of Cu2+ to stepped surfaces of ZnO

Segregation energy (kJ/mol)		
Index	Niche	Top
(1,-1,0)	-12.36	-60.78
(1,-2,0)	-6.63	-57.46
(1,-3,0)	150.99	-24.11
(1,-5,0)	-7.06	-57.23
(1,-7,0)	-6.90	-57.26
(1,-9,0)	-6.97	30.22

Table 4.7.1

Copper (II) substitution defects
CASCADE energies (kJ/mol)

A(g) + B(ZnO) -> A(ZnO) + B(g)

Zn site	Net defect charge	Energy of bulk substitution
Cu	0	30.66

Surface substitution energies

	Surface Index			
	(1,1,0)		(1,-1,0)	
	Top	Niche	Top	Niche
Unrelaxed	-8.17	29.59	-5.86	21.98
Relaxed	-25.17	23.95	-21.22	10.50

Figure 4.8.1 Surface sites on the (1,-1,0) and (1,1,0) surfaces

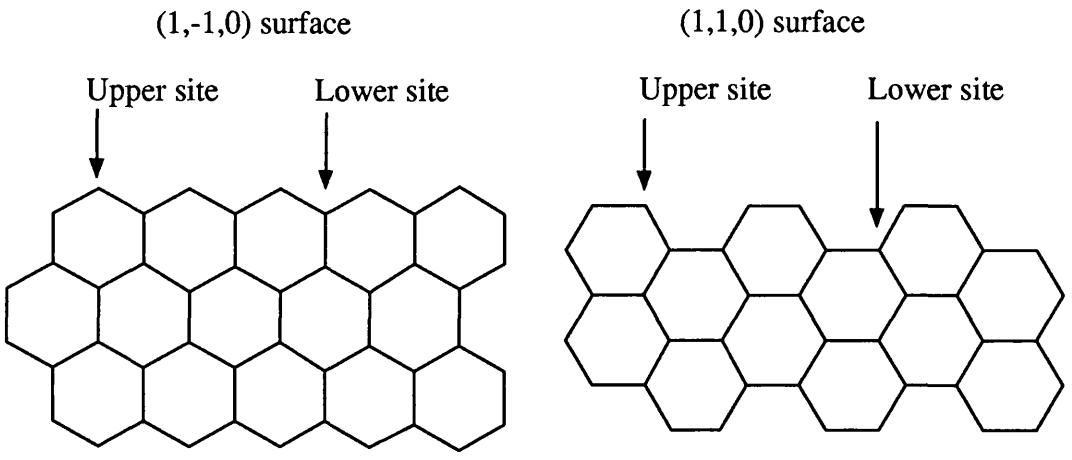

exposed sites on both surfaces, so cupric ions will be present under equilibrium conditions, and cuprous ions may be formed and play a role in catalysis at the surface under non-steady reaction conditions. The more confined cation sites do not favour copper and therefore doping of zinc oxide by copper should not create a copper oxide surface layer. This is an important result for catalysis as this ensures that the copper atoms will remain dispersed unless it receives sufficient heat treatment to allow the atoms to diffuse. However the calculations suggest that cuprous ions are not stable on the surface, and thus do not play a part in the initial chemisorption. This is in agreement with recent work on the mixed copper/zinc oxide catalysts which find no evidence for Cu^{1+} [Millar *et al.* (1993)].

The role of copper metal particles cannot be addressed in this simulation, however the idea that separate copper particles alone catalyse methanol synthesis does not explain the catalytic properties of zinc oxide alone - a mechanism involving the influence of copper on the zinc oxide catalyst seems more likely. One suggested mechanism for the enhancing effect of copper is that it results in extensive defect creation on the oxide surface [Millar (1993), Frost (1988)] which provides sites for carbon dioxide adsorption. These calculations support this idea as they show that the copper stabilises steps which have been implicated as reaction sites for methanol

synthesis, hence this work suggests that in the presence of copper a larger number of steps will be formed on the surface, improving the catalytic properties.

4.9 Adsorption of Methanol on the polar surface

Another important component of studying the reactivity of catalyst surfaces is their interaction with gaseous species. Energy minimisation of a molecule on a zinc oxide surface may only find a local minimum in potential energy, but in the case of physical adsorption the molecule will be comparatively loosely bound and hence will experience interactions with more than just the minimum energy site. Therefore we also tried modelling the adsorption using a Monte-Carlo approach described in chapter 2. For this calculation I developed a computer code module which attaches to the static simulation code THBREL to perform the Monte-Carlo simulation using the Metropolis algorithm. The use of the Metropolis formula allows the calculation of average energies of adsorption and probable adsorption positions simply from the mean average of the states that are selected. The partial charges assigned to the methanol's atoms and the geometry of the methanol molecule was obtained non-empirically from a Mullikan analysis of a geometry-optimised ab-initio

Table 4.8.1

Copper (I) substitution defect energies (kJ/mol)

A(g) + B(ZnO) -> A(ZnO) + B(g)

A/B	Defect charge	Bulk defect energy
(a) Cu1+ for Zn2+	-1	1793.76
(b) O1- for O2-	1	1746.33
(a) + (b)	0	3540.09
(a) + (b) adjacent	0	3473.55

CASCADE Surface Cu1+ substituting for Zn2+ energies

	Surface Index			
	(1,1,0)		(1,-1,0)	
	Top	Niche	Top	Niche
Unrelaxed	2325.30	2393.21	2291.55	2440.05
Relaxed	1721.77	1801.22	1683.32	1849.68

Defect segregation energies

	Surface Index			
	(1,1,0)		(1,-1,0)	
	Top	Niche	Top	Niche
Cu1+	-71.99	7.46	-110.44	55.92

calculation [Titiloye (1992)], and were held fixed in the simulation. The surface interaction was modelled in the program using three-dimensional periodicity, requiring 'infinite slabs' to represent the surface. The results showing energies of adsorption at different temperatures are given in Table 4.9.1. The static energies of the zinc oxide slab and methanol separately were -63216 kJ/mol and -2223 kJ/mol respectively. As Figures 4.9.1 and 4.9.2 show, the methanol in the minimum energy (0 Kelvin) position is positioned with the oxygen directly above a zinc in the surface.

The calculated energies depend on the potential between the lattice ions and the atoms in the methanol. The methanol oxygen was considered to interact with the crystal with the same short-range potential as the lattice oxide ions, and the Coulombic interactions were based on the ab-initio calculated partial charges of the methanol. It was assumed that the interactions involved no bond-breaking. More quantitative results would require improved, perhaps ab-initio, potentials for small molecules and their interaction with ionic species.

The Monte-Carlo program is based on static simulation code, which enables the potential types and methodology of static calculations to be used directly and allows direct comparison with static calculations, and the application of standard static potentials avoids the development of potentials specifically for this calculation

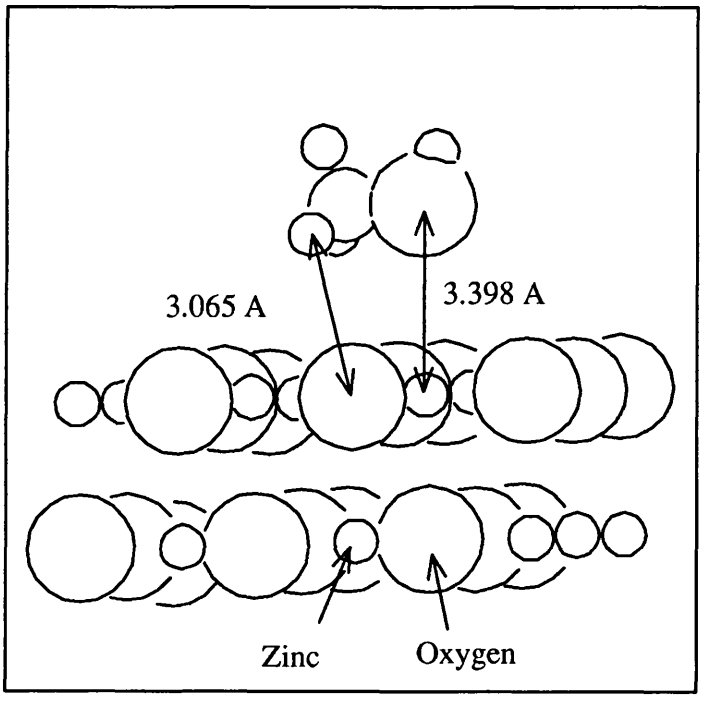

Figure 4.9.1 Methanol zero kelvin orientation: Side view

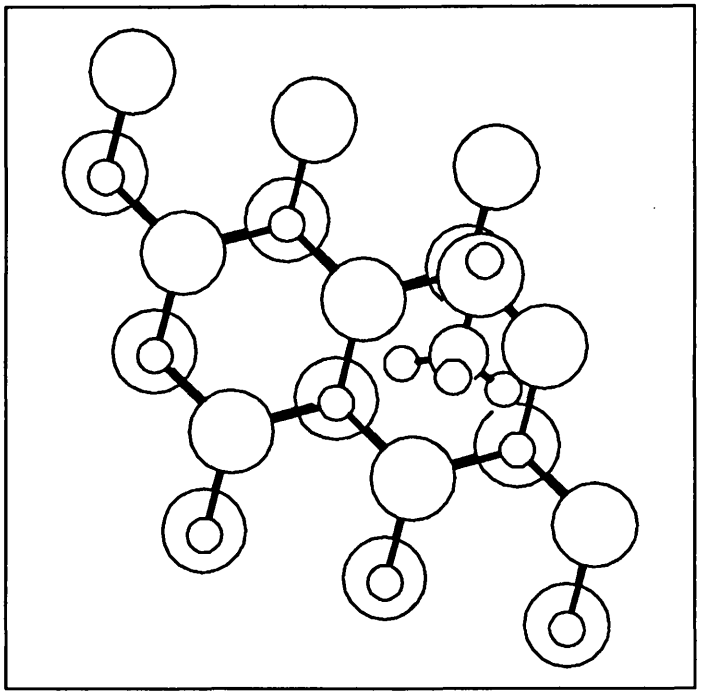

Figure 4.9.2 Methanol zero kelvin orientation: Top view

which saves much effort, provided always that the potentials are adequate in the greater range sampled by Monte-Carlo techniques. The Monte-Carlo calculations show a decrease in the energy of adsorption with temperature (Table 4.9.1), but the difference in the results of the two calculations performed for 130K show that a much greater number of iterations will be needed to produce reliable results. With a sufficient number of iterations the most probable orientation of the methanol for each position on the surface can be determined. This is principally due to the fact that the potentials and the method of calculating the energy are more complex than those usually used in Monte-Carlo programs coupled with insufficient computing resources means that I have not obtained enough results to calculate other statistics. However the ability to move from static simulation to calculating properties at different temperatures using this technique can further the usefulness and improve the generality of our potential models. It is apparent that there were an insufficient number of iterations to obtain good statistics, due to the large number of ions required and the limited computing resources available.

4.10 Summary

These results suggest the most common intrinsic defects in the bulk are Zn^{1+} interstitials although the energies are very large, indicating a low concentration. However the negative segregation energies to all surfaces will lead to a large surface enhancement. The energies of copper substitutions show that copper will segregate preferentially to step sites on all surfaces, which are accepted as the catalytically active sites, and hence may significantly enhance the catalyst. Thus these calculations predict that part of the function of copper is to stabilise the step surfaces, and that the ions on segregating will be isolated. Thus will lead, on reduction, to finely divided copper sites. However the modelling of islands of copper metal on the surface which is also considered a plausible cause of its catalytic activity, was not attempted due to the problems of combining ionic crystal and metal potentials. The preferential segregation of Cu^{2+} to step sites has a stabilising effect on the more highly stepped surfaces, thereby increasing the proportion of active sites. The catalytic activity of copper could be then be due to this effect, without playing a direct role at the active site.

From the calculation of bulk defect energies we get a rough value of the band

gap of zinc oxide. The value obtained using these results is too high at 867.7 kJ/mol, experimental evidence gives a more reasonable value of 330 kJ/mol [Landholt-Bornstein]. One reason for this result may be that the small polaron model used in these calculations, where the electronic defects are localised on a lattice site. is unable to model these defects correctly. Using the results of available electron gas calculations of the zinc oxide short range potential to fit potentials may lead to more accurate results for these electronic properties.

The modelling of the prismatic faces show a smooth variation of surface energy with Miller index, indicating that to a good approximation the surface can be thought of as steps added to the (1,-1,0) surface, with some slight attractive interaction between the steps. The polar surface shows a significantly higher formation energy which cannot be ameliorated by the addition of intrinsic defects, confirming the experimental observation that the prismatic faces dominate the morphology and suggesting that the polar surface contains many unsaturated surface sites.

The Monte-Carlo results show the minimum energy configuration of methanol surface. The orientation of the molecule suggests that chemisorption is accompanied by movement of the hydroxyl from the methyl group and attachment to a surface zinc

ion. By the further application of Monte-Carlo techniques accurate energies of adsorption to the stepped and copper-containing surfaces can be determined for methanol and other small molecules at different temperatures, and for the interactions between these adsorbed molecules, and with the use of a potential model that remains valid over a transition state, we could then even examine the mechanisms and rates of reaction directly.

The Monte-Carlo method allows the use of potentials and code that was previously only applied to static calculations, to be used for the calculation of statistical properties at specific temperatures, densities or pressures. The potentials that were developed to yield static energies should give excellent results in Monte-Carlo calculations.

In the following chapter we attempt to extend the range of applications by considering the surface structure and stability of complex oxides with the structure ABO_3.

Chapter 5

Ternary Oxides

5.1 Introduction

The aim of this chapter is to apply the simulation methods described in chapters 2 and 3 to model the surfaces of materials having the perovskite and ilmenite structures. In each case one compound was taken as a model system. Not only is it valuable to investigate the surface properties of ternary oxides in their own right, but many earlier studies on the binary oxides have shown that even low levels of dopants will segregate to their surfaces. There is, therefore, the possibility of the formation of ternary oxides at the binary oxide surfaces and hence the surface properties of the binary oxides may be controlled by the surface properties of the ternary oxides. In addition, the application of potential parameters derived from simple structures to more complex structures can provide a stringent test of the transferability of the potential, and when applied to ternary oxides, this allows us to test the limits of applicability of the Born model. The particular oxides studied were those from the perovskite and the ilmenite mineral classes for which previous experimental and

simulation data are available.

The perovskites represent an important class of mineral. We have chosen to model strontium titanate as it provides a good test of calculations on the bulk and surface structures, has important catalytic properties and has been previously studied computationally [Mackrodt (1990)]. The surface properties have also been most closely studied because of its use as a substrate, particularly for high T_C superconductors [Huang (1993), Catana (1993), Amrein (1993)]. The approach, as outlined earlier, is to transfer the potentials from the binary oxides to calculate the bulk structure, then to model the surface structure and surface relaxation, and finally to compare the results with other computational and experimental work.

Ilmenite is also an important class of minerals, frequently studied by earth scientists as it is a structure adopted by magnesium silicate, which constitutes much of the earth's mantle. The predominant phase of magnesium silicate at high pressure and temperature in the earth, however, has the perovskite structure. As with perovskite, ilmenite has the stoichiometry ABO_3. However, ilmenite is closely related to the corundum structure (differing from it only in the identity of the cations), which has been modelled successfully [Catlow *et al.* (1982)]. One problem with modelling ilmenite compared to the perovskite and lithium niobate structures is that the relative stability is sensitive to the cationic charges and relative cation radii

[Leinenweber (1991)], and thus calculations on this structure may be considered problematic for models using parameters derived assuming formal ionic charges from simple binary oxides. In contrast to perovskites the ilmenites have hexagonal symmetry and there is no centre of inversion at the ion sites, thus the structural details of the perfect crystal will be dependent on the ionic polarisabilities. Manganese titanate has the ilmenite structure at room temperature and has recently been shown to transform to the lithium niobate structure at higher temperatures and pressures [Ross (1989)]. Therefore applying empirical potentials derived from room-temperature data to manganese titanate with each of these structures should expose the limitations of the low-temperature assumptions and the ability of the potentials to compare structures across phase transitions.

5.2 Strontium titanate

Materials with the ABO_3 perovskite structure encompass many examples of compounds with interesting properties, including ferroelectric [Tilley (1977)], piezoelectric [Muller (1986)], superconducting [Schooley (1964)], and non-linear optical [Tschudi (1986)] effects. Many of these properties depend on the precise defect chemistry, which is intimately related to the impurity concentration,

stoichiometry., interfacial structure and other microscopic phenomena which ultimately determine the bulk properties. Atomistic simulation can probe this level of structure and provide some insight into the microscopic processes leading to the bulk properties of interest. Strontium titanate has the perovskite structure with strontium and titanium occupying the A and B sites respectively, and was chosen, because of good experimental data, as a representative perovskite to model.

5.2.1 Previous Work on Strontium Titanate

Strontium titanate adopts the perfect perovskite structure with cubic symmetry above 106 K [Muller (1971)] (see figure 5.2.2.1). The strontium and oxygen ions together form an arrangement of cubic close packing, i.e. the strontium is twelve-coordinated by oxygen and the oxygen is adjacent to four strontium ions and eight oxygen ions. With respect to the cubic cell, the strontium occupies the cell vertices and the oxygen occupies the face centres, while the titanium is located in the octahedral interstices of the oxygen sublattice. Below 106 K strontium titanate undergoes an orthorhombic distortion. The potentials used in this work were derived from fitting to room-temperature data, and thus model the 300K structure. These calculations were prompted by the results of earlier calculations by Mackrodt and

Stewart (1990) which showed substantial relaxation of the (1,0,0) surfaces inward to the crystal. In contrast, experimental results [Bickel *et. al.* (1989)] have suggested a slight relaxation outward. Since Mackrodt and Stewart have used non-empirically derived potentials in their calculations, my investigation of the relaxation with empirical potentials would provide a comparison of the two approaches. The most stable surfaces generally tend to be close packed, or equivalently have weaker short-range binding forces in the normal direction. There are two naturally close-packed directions in the perovskite structure: layers normal to the <1,0,0> direction and to the <1,1,1> direction. In the <1,1,1> direction the layers are composed of strontium and oxygen, with interlayer titanium ions (see figure 5.2.2.2). These layers have net charges, and thus are type III layers according to the Tasker classification. An attempt to model a surface using one of these layers as the terminating layer would lead to a surface dipole, necessitating the introduction of surface defects which would disrupt the terminating layer. The <1,0,0> direction shows layers composed alternately of SrO and TiO_2. These closed packed layers are neutral and are thus able to terminate a surface without creating a dipole. The experimental observations were made on the (1,0,0) surface, which have the closest-packed surface layer and experimentally are the dominant surfaces, and therefore the theoretical calculation also modelled these surfaces. The computer

model started with the bulk terminated structure and we observed the extent and direction of movement of the ions during the surface relaxation. Experimental work showed there to be surface reconstruction to yield a (2x2) structure observed [Anderson (1990)] after annealing at 800 °C. Therefore, it was important to perform calculations on a surface 2x2 supercell to determine if any reconstruction could be seen with static simulation. Normal to the {1,0,0} direction the crystal is composed of alternating neutral Sr-O and Ti-O layers, thus there are two possible terminations for the (1,0,0) surface, with the terminating layer composed of either strontium and oxygen or titanium and oxygen. Both of these terminations were modelled.

5.2.2 Results

The calculated unit cell had a lattice constant of 3.98 Ångstroms (see table 5.2.2a), while Bickel (1989) found a lattice constant of 3.82 +/- 0.15 Ångstroms. The literature value [Wyckoff (1963)] of 3.91 Ångstroms would imply the calculated value overestimates the crystal dimensions by 1.7%.

For both surfaces the perpendicular relaxation of the surface oxygen with respect to the cation, and the first two inter-layer separations, were determined and

Table 5.2.2a

Strontium titanate
calculated unit cell

Lattice vectors (Angstroms)

3.9768	0.0000	0.0000
0.0000	3.9768	0.0000
0.0000	0.0000	3.9768

Coordinates of species

Species	X	Y	Z
Ti core	0.0000	0.0000	0.0000
Sr core	1.9884	1.9884	1.9884
O core	1.9884	0.0000	0.0000
O core	0.0000	1.9884	0.0000
O core	0.0000	0.0000	1.9884
O shell	1.9884	0.0000	0.0000
O shell	0.0000	1.9884	0.0000
O shell	0.0000	0.0000	1.9884

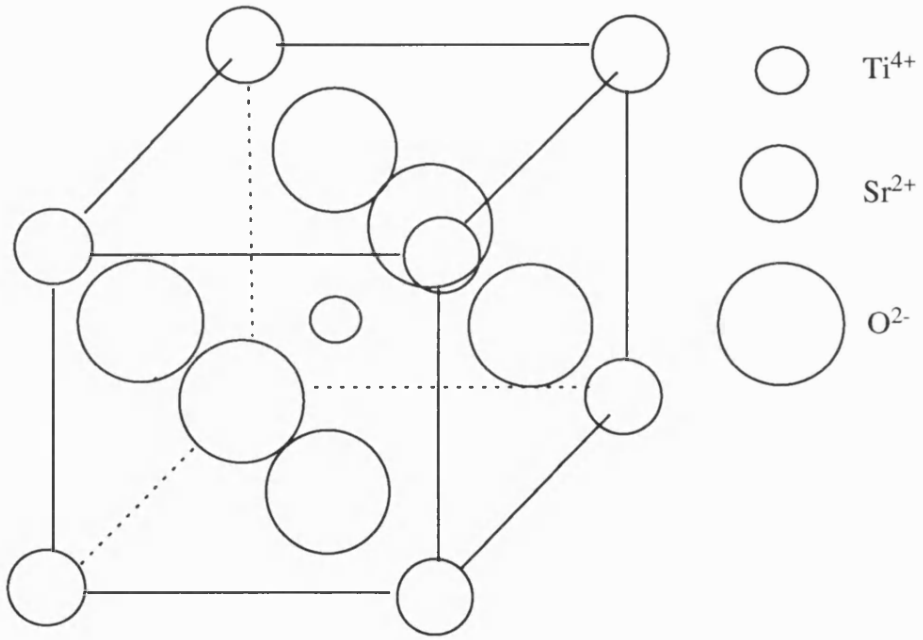

Figure 5.2.2.1 Strontium Titanate unit cell

compared to low energy electron diffraction results and the other calculations on this structure [Bickel (1989), Mackrodt (1990)].

Tables 5.2.2b and 5.2.2c show the relaxation of the surface layers from the bulk terminated positions, measured in Angstroms with respect to the bulk. The positive direction is into the crystal. For both surfaces there is a contraction of the surface layer towards the next layer, with subsequent layers relaxing upwards, yielding a calculated contraction of 7% and 5% for the top two layers of the titanium- and strontium-terminated surfaces respectively. The comparison of inter-layer separations with other work is shown in table 5.2.2d.

The surface energies for the titanium and strontium surfaces are also given. The titanium surface is of slightly lower surface energy. However a stoichiometric crystal requires the same area of each type of surface, so that the surface energy of the (1,0,0) surface should be calculated as an average of the two types of termination. A large difference in the surface energies would favour the creation of defects - probably Ruddleston-Popper layers - while similar surface energies would favour the presence of a mixture of the two types of terminations. In this case, the similar surface energies suggest the terminations would yield a mixed - and hence rough - surface.

The electron diffraction experiment [Bickel (1989)] suggested outward oxygen

Table 5.2.2b

Relaxation of the strontium-terminated surface
(distances in Angstroms, +ve is into the crystal)

Species	Depth	Relaxation
O core	0.0000	0.0540
Sr core	0.0299	0.0839
O shell	0.0438	0.0977
Ti core	1.9149	-0.0195
O shell	1.9232	-0.0112
O shell	1.9232	-0.0112
O core	1.9247	-0.0098
O core	1.9247	-0.0098
O core	3.9211	-0.0017
O shell	3.9230	0.0002
Sr core	3.9288	0.0060
Ti core	5.9079	-0.0034
O shell	5.9091	-0.0021
O shell	5.9091	-0.0021
O core	5.9093	-0.0020
O core	5.9093	-0.0020
O core	7.8976	-0.0020
O shell	7.8977	-0.0019
Sr core	7.8985	-0.0011
Ti core	9.8861	-0.0019
O shell	9.8862	-0.0018
O core	9.8862	-0.0018
O shell	9.8862	-0.0018
O core	9.8862	-0.0018
O core	11.8747	-0.0017
O shell	11.8747	-0.0017
Sr core	11.8748	-0.0016
Ti core	13.8632	-0.0016
O core	13.8632	-0.0016
O core	13.8632	-0.0016
O shell	13.8632	-0.0016
O shell	13.8632	-0.0016

Table 5.2.2c

Relaxation of the titanium-terminated surface
(distances in Angstroms, +ve is into the crystal)

Species	Depth	Relaxation
O core	0.00000	0.00416
O core	0.00000	0.00416
O shell	0.00909	0.01325
O shell	0.00909	0.01325
Ti core	0.07901	0.08317
Sr core	1.92659	-0.05762
O shell	1.97688	-0.00733
O core	1.98609	0.00188
O core	3.96902	-0.00360
O core	3.96902	-0.00360
O shell	3.96994	-0.00268
O shell	3.96994	-0.00268
Ti core	3.97887	0.00625
Sr core	5.95387	-0.00713
O shell	5.95900	-0.00200
O core	5.95976	-0.00124
O core	7.94733	-0.00208
O core	7.94733	-0.00208
O shell	7.94741	-0.00200
O shell	7.94741	-0.00200
Ti core	7.94829	-0.00112
Sr core	9.93555	-0.00224
O shell	9.93603	-0.00176
O core	9.93611	-0.00168
O core	11.92452	-0.00168
O core	11.92452	-0.00168
O shell	11.92452	-0.00168
O shell	11.92452	-0.00168
Ti core	11.92460	-0.00160
Sr core	13.91302	-0.00156
O shell	13.91306	-0.00152
O core	13.91306	-0.00152

Table 5.2.2d

Calculated and experimental (0,0,1) surface relaxations, compared to previous work.

TiO_2 terminated surface relaxation

Species	Bulk	Final disp.(Å)	Expt	Prev.
Oxygen core	0.00	-0.08		
Oxygen shell	0.00	-0.07	-0.08(+/-0.08)	+0.04
Titanium	0.00	0.00	0.00	0,00
Oxygen core	1.99	1.91		
Oxygen shell	1.99	1.90	+2.04(+/-0.04)	+1.6
Strontium	1.99	1.85		

SrO terminated surface relaxation

Species	Bulk	Final disp.(Å)	Expt[1]	Prev.[2]
Oxygen core	0.00	-0.03		
Oxygen shell	0.00	0.01	-0.16(+/-0.08)	+0.14
Strontium	0.00	0.00	0.00	0.00
Oxygen core	1.99	1.89		
Oxygen shell	1.99	1.89	1.802(+/-0.040)	+1.52
Titanium	1.99	1.88		

(1) Experimental work: Bickel (1986)
(2) Previous calculations: Mackrodt (1990)

Surface area of unit cell: 15.814 $Å^2$

Surface energies

Termination	Surface Energy (J/m^2)
TiO_2	1.458
SrO	1.488
Average	1.473

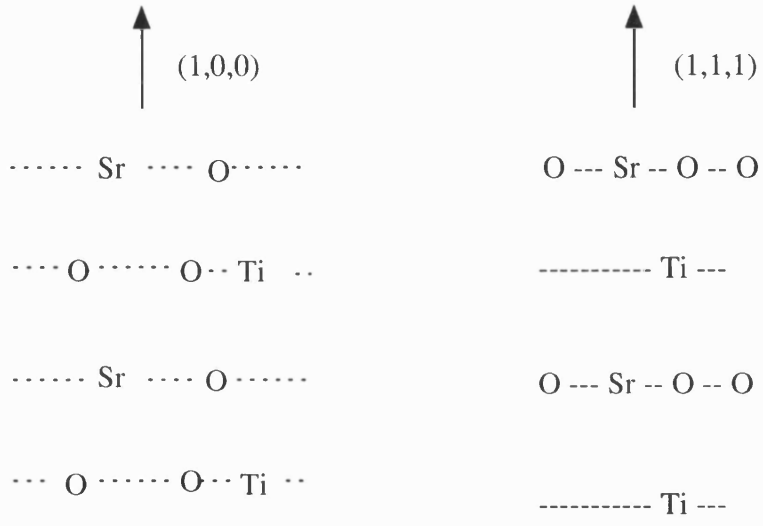

Figure 5.2.2.2 Stacking sequences in different orientations

relaxation for the titanium surface of 0.08 (+/-0.08) Angstroms, and 0.16 (+/- 0.08) Angstroms for the strontium surface. Thus the results of our calculations, shown in table 5.2.2d, lie within experimental error of their results. They find the first two layer separation changes by +2 (+/-2) % and -10 (+/-2) % for the titanium and strontium surfaces. I calculate changes of -1.0 % and -4.5 % with respect to the oxygen shell positions, and 0.0 % and -3.5 % with respect to the oxygen cores for the respective terminations. Thus the contraction calculated for the strontium surface is smaller than determined from the experiment, while the titanium relaxation is consistent with the LEED results. Mackrodt's results show a large (approximately 22%) contraction for both surfaces, in contrast to both the experimental results and my calculations already discussed above.

The simulation results show vertical movement of adjacent layers no larger than 0.15 Angstroms, of the same magnitude as the experimental results. The symmetry of the unit cell constrains the motions of ions in adjacent cells to be identical, so the similar movements could be an artifice of the simulation. To check this, calculations were also performed on larger surface areas (2x2 supercells). These did not show any additional reconstruction. Recent scanning tunnelling microscope (STM) imaging of the (1,0,0) [Matsumoto (1992)] surface after annealing in UHV has found steps with heights of 4.2 Angstroms on the surface, corresponding to a

complete unit cell step. The distance between equivalent oxygen layers can be seen to have expanded by ~7% from the bulk value which is lends support to my conclusion that the unit cell has a net expansion at the surface, further conflicting with the non-empirical potentials calculation of Mackrodt (1990).

Thus the evidence shows that the calculated relaxations for this surface modelled with the empirical potentials are in better agreement with experiment than the non-empirical calculation.

5.2.3 Summary

These results show relaxation of the cations into the surface, reducing the effects of lower coordination on the cations. The titanium terminated surface is calculated to be more stable by 0.03 J/m^2, this small difference would imply the surface exists as a mixture of the two terminations. There is reasonable agreement of my calculated values with the experimental results of Bickel et al., with the exception of the predicted small contraction (about 1 %) of the titanium-terminated surface compared to the small expansion seen. A recent calculation using a shell model derived from bulk phonon dispersion curves [Prade (1993)] shows qualitative agreement with the L.E.E.D. experiment although, as with this work, they find a

decrease in first inter-layer separation in the titanium-terminated surface. They ascribed this to the inaccuracy of using the bulk short-range titanium-oxygen interaction for surface interactions. In contrast Mackrodt's results show large movements of the surfaces inwards. The large difference in the results of the two calculations suggest the non-empirical potential may be less effective in modelling the surfaces of this material.

5.3 Manganese Titanate

Ilmenite occurs naturally as {Iron^{II}, Magnesium, Manganese} titanate and has a structure similar to corundum, which has been modelled successfully [Parker (1983)]. Pure manganese titanate has the ilmenite structure and is of particular interest to earth scientists as it undergoes a transition to the lithium niobate structure at high pressure, unique for a II-IV compound [Ross (1989)]. An important class of minerals exhibit the ilmenite structure at high temperature and pressure and some may undergo similar transitions. For this reason as well this mineral was also modelled, as the ability of current simulation techniques to duplicate the relative stability should be a sensitive test of our potentials. The ilmenite structure is closely related to the structure of corundum, which in the form of α-alumina has been widely studied. Both

of these structures have oxygen ions arranged in approximately hexagonal close packing. The cations then must occupy the 6-coordinate octahedral sites between the oxide layers. The cations can fill two-thirds of these sites, and in corundum these cation octahedra form a face and edge sharing network. The partial occupancy of these sites prevents full hexagonal symmetry and the one-third of empty oxygen octahedra are arranged with hexagonal symmetry in the planes perpendicular to the *c*-axis. The cations in the ilmenite structure occupy the same sites, but the structure differs in that the layers of cation sites perpendicular to the hexagonal axis are alternately filled with the distinct ion types (see figure 5.3.2.1a). The sites are chosen such that adjacent face-sharing octahedral sites contain dissimilar cations. The lithium niobate structure is very similar, differing in only the cation distribution between sites such that the cation layers contain both types of ion, but maintain dissimilar face-sharing octahedra. The similar energies of the ilmenite and lithium niobate structures calculated below suggest the possibility that cation disorder may play a significant role in the defect structure of both phases.

5.3.1 Previous work

Refinements of the experimental structure and electron density of manganese

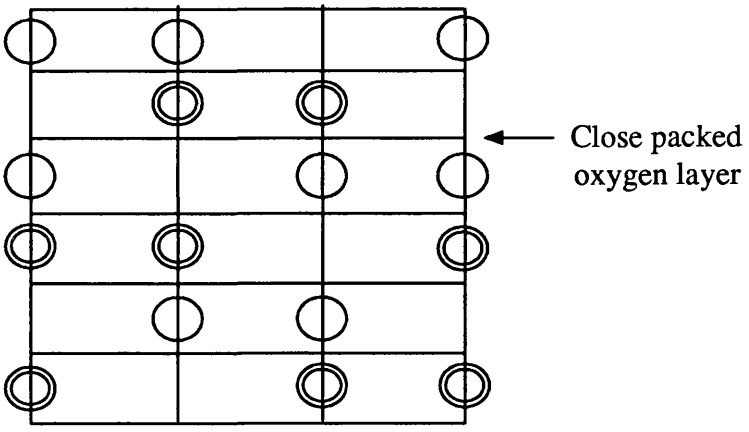

Figure 5.3.2.1a: Idealised cation sites in ilmenite

titanate have been performed with the single-crystal X-ray diffraction method [Kidoh (1984)] and the cell coordinates from that study show that whilst the TiO_6 octahedra are fairly symmetric, the MnO_6 octahedra are distorted. Both cations are displaced towards the vacant octahedral sites. A region of positive electron density between the manganese ions is interpreted as evidence of a significant manganese-manganese interaction. This is consistent with its two-dimensional antiferromagnetic behaviour at low temperatures, in contrast to other antiferromagnetic ilmenites [Todate (1966)]. The determined structure of manganese titanate suggests that some cation disorder exists, giving the approximate formula $(Mn_{0.92}Ti_{0.08})(Ti_{0.93}Mn_{0.06}\square_{0.01})O_3$ [Kidoh (1984)].

The transition from the ilmenite to the lithium niobate structure has been shown to be favoured by both increased temperature and pressure [Ko (1989)]. A similar transition to a lithium niobate phase has also been claimed for $FeTiO_3$ ilmenite at high pressures [Leinenweber (1991)]. Atomistic calculations on manganese titanate with the lithium niobate structure have recently been performed [Ross (1992)], reproducing the experimentally observed lattice parameters to within 2%. However those calculations were not extended to the low-temperature ilmenite structure.

5.3.2 Results

5.3.2.1 Bulk structure

The bulk structure was calculated by applying the empirical potentials derived from the binary oxides [Lewis (1985)] to the ions in the structure as initially determined from X-ray diffraction [Kidoh (1984)] , and allowing relaxation to the calculated minimum energy configuration using the program THBREL. The same crystal structure was also obtained by minimising the ionic coordinates and lattice vectors from the experimental corundum structure. Example input datasets for the ilmenite and lithium niobate bulk structure calculations are given in tables 5.3.2.1a and 5.3.2.1b respectively. The lattice parameters and fractional coordinates for these structures were calculated, and are shown in tables 5.3.2.1c and 5.3.2.1d. Interatomic distances for the ilmenite structure were then calculated from the minimised coordinates and compared to the distances determined by Kidoh. The comparison of these distances, given in Table 5.3.2.1e, shows the largest discrepancies between the calculated and experimental nearest-neighbour distances occur with the manganese - oxygen distances, which are calculated to be 3.5% to 6.3% larger than those found experimentally. The oxygen - oxygen distances are calculated to be less than the

Table 5.3.2.1a

Manganese titanate ilmenite structure input

```
TITLE
MnTiO3 - ilmenite - based on Al2O3 (Corundum)
ENDS
DIME 200000
PRIN BOND 2
THERMAL
CUTO 13.00 1.1 0.05 20.0 20.0 1.0
LATT
     0.203698973692     0.117605657295     0.367943595724
    -0.203698973692     0.117605657295     0.367943595724
     0.000000000000    -0.235211314590     0.367943595724
BASI
OX2- CORE    -0.083283150867     0.117605657295     0.636698574270    0
OX2- CORE    -0.051829945320    -0.109694691641     0.636698574270    0
OX2- CORE     0.079401972325    -0.091535174952     0.429277499360    0
OX2- CORE     0.129291328374     0.031194757860     0.636698574270    0
OX2- CORE     0.047948766778     0.135765173984     0.429277499360    0
OX2- CORE    -0.133172506916    -0.005124275517     0.429277499360    0
MN2+ CORE    -0.001940589271     0.013035241172     0.128619567155    0
MN2+ CORE    -0.001940589271     0.013035241171     0.937356506475    0
TI4+ CORE    -0.001940589271     0.013035241172     0.372849147230    0
TI4+ CORE    -0.001940589271     0.013035241171     0.693126926400    0
OX2- SHEL    -0.082577587058     0.115786380105     0.638818743313    0
OX2- SHEL    -0.050607186962    -0.108174016864     0.638818743313    0
OX2- SHEL     0.078696408516    -0.089715897762     0.427157330316    0
OX2- SHEL     0.127363006207     0.031493360273     0.638818743313    0
OX2- SHEL     0.046726008419     0.134244499207     0.427157330316    0
OX2- SHEL    -0.131244184749    -0.005422877930     0.427157330316    0
ENDS
POTE
SPEC
MN2+ CORE 2.0 1.00
TI4+ CORE 4.000 65.37
OX2- CORE  0.53 15.99
OX2- SHEL -2.53 0.0
ENDS
BUCK MN2+ CORE OX2- SHEL
715.87 0.3464 0.0
ENDS
BUCK TI4+ CORE OX2- SHEL
754.2 0.3879 0.0 0.0
ENDS
BUCK OX2- SHEL OX2- SHEL
22764.0 0.149 27.88 20.0
ENDS
HARM OX2- CORE OX2- SHEL 86.40 00000.0
ENDS
START PLUT
CONP
LIMI 0.0000001
MAXU 1
MAXI 1000
START
STOP
```

Table 5.3.2.1b

Manganese titanate LiNbO3 structure input

```
TITLE
MnTiO3 - LiNbO3 structure - based on Al2O3 (Corundum)
ENDS
DIME 200000
PRIN LATT 0 BASI 1 PLUT 00011 ENGY 1 MINI 0 BOND 1 POTE 1 PHON 0
THERMAL
CUTO 13.00 1.0 0.05 20.0 20.0 1.0
LATT
     0.203846392625     0.117690769656     0.345241371583
    -0.203846392623     0.117690769655     0.345241371583
     0.000000000000    -0.235381539306     0.345241371581
BASI
OX2- CORE    -0.083343423693     0.117690769657     0.597414091779    0
OX2- CORE    -0.080150974480    -0.168921416203     0.597414091774    0
OX2- CORE     0.085324648184    -0.117690769652     0.424793405987    0
OX2- CORE     0.166466234906    -0.022850581156     0.597414091778    0
OX2- CORE     0.039361382210     0.094840188495     0.424793405985    0
OX2- CORE    -0.121714193653    -0.051230646551     0.424793405984    0
MN2+ CORE     0.000990612245    -0.024693742571     0.097272601349    0
MN2+ CORE     0.000990612246    -0.024693742568     0.615134658722    0
TI4+ CORE     0.000990612245    -0.024693742570     0.345025019963    0
TI4+ CORE     0.000990612246    -0.024693742568     0.862887077337    0
OX2- SHEL    -0.083326402359     0.118451952552     0.597300252423    0
OX2- SHEL    -0.080818688872    -0.169287266744     0.597300252418    0
OX2- SHEL     0.085307626851    -0.116929586757     0.424679566632    0
OX2- SHEL     0.167116927964    -0.023245913511     0.597300252422    0
OX2- SHEL     0.038710689152     0.094444856140     0.424679566629    0
OX2- SHEL    -0.121046479262    -0.051596497092     0.424679566629    0
ENDS
POTE
SPEC
MN2+ CORE 2.0 1.00
TI4+ CORE 4.000 65.37
OX2- CORE  0.53 15.99
OX2- SHEL -2.53 0.0
ENDS
BUCK MN2+ CORE OX2- SHEL
715.87 0.3464 0.0
ENDS
BUCK TI4+ CORE OX2- SHEL
754.2 0.3879 0.0 0.0
ENDS
BUCK OX2- SHEL OX2- SHEL
22764.0 0.149 27.88 20.0
ENDS
HARM OX2- CORE OX2- SHEL 86.40 00000.0
ENDS
START PLUT
CONP
MAXI 100
MAXU 20
TIDY 50
START
STOP
```

Table 5.3.2.1c

Calculated structure of MnTiO3 ilmenite

Space Group
R-3(R)

Lattice Constant (Angstroms)
13.00

Hexagonal lattice constants

	Calc.	Expt.	% diff.
a parameter	5.295	5.138	2.965
c parameter	14.348	14.283	0.453

Rhombohedral lattice vectors/Lattice Constant

0.2037	0.1176	0.3679
-0.2037	0.1176	0.3679
0.0000	-0.2352	0.3679

Cartesian coordinates/Lattice Constant

Ion	X	Y	Z
Mn2+	-0.0019	0.0130	0.1286
Mn2+	-0.0019	0.0130	0.9374
Ti4+	-0.0019	0.0130	0.3729
Ti4+	-0.0019	0.0130	0.6931
O2-	-0.0833	0.1176	0.6367
O2-	-0.0518	-0.1097	0.6367
O2-	0.0794	-0.0915	0.4293
O2-	0.1293	0.0312	0.6367
O2-	0.0480	0.1358	0.4293
O2-	-0.1332	-0.0051	0.4293

Table 5.3.2.1d

Nearest-neighbour distances in MnTiO3 - LiNbO3 structure

Lattice Constant (Angstroms)
13.00

Lattice vectors

0.2037	0.1176	0.3679
-0.2037	0.1176	0.3679
0.0000	-0.2352	0.3679

O2-	-0.0833	0.1176	0.6367
O2-	-0.0518	-0.1097	0.6367
O2-	0.0794	-0.0915	0.4293
O2-	0.1293	0.0312	0.6367
O2-	0.0479	0.1358	0.4293
O2-	-0.1332	-0.0051	0.4293
Mn2+	-0.0019	0.0130	0.1286
Mn2+	-0.0019	0.0130	0.9374
Ti4+	-0.0019	0.0130	0.3728
Ti4+	-0.0019	0.0130	0.6931

Neighbours within 3 Angstroms
Ion
Distances from O2- ion

O2-	2.4607

Distance from Mn2+ ion

O2- (x3)	2.4244
O2- (x3)	2.1835

Distances from Ti4+ ion

O2- (x3)	2.0952
O2- (x3)	1.8720

Table 5.3.2.1e

Nearest-neighbour distances in MnTiO3 ilmenite

Ion	Calculated	Experimental [Kidoh 1984]	% diff.
Distances from Mn (Angstroms)			
O (x3)	2.18	2.11	3.47
O (x3)	2.42	2.28	6.34
Distances from Ti (Angstroms)			
O (x3)	1.87	1.88	-0.30
O (x3)	2.10	2.08	0.58
Distances from O (Angstroms)			
Ti (x1)	1.87	1.88	-0.30
Ti (x1)	2.10	2.08	0.58
Mn (x1)	2.18	2.11	3.46
Mn (x1)	2.42	2.28	6.34
O (x1)	2.46	2.58	-4.45

Next-nearest neighbour distances		
Ti	Ti	3.12
Mn	Mn	3.20
Mn	O	3.41
Mn	Ti	3.18
Mn	Ti	3.45
O	O	2.77
O	O	2.89
O	O	2.98
O	O	3.20
O	O	3.32
O	O	3.47

experimental distances by 4.4%, whereas the titanium - oxygen distances are within 0.6% of the experimental values. All of these differences may be explained in part by the assumption made in the calculation of interatomic distances that the 'cores' represent the nuclear positions. In these calculation the cores represent the nuclei and core electrons, therefore the nuclei would be expected to be displaced further towards negative ions and away from positive ions than the distances based on the 'cores' position. This effect would be expected to be larger for the manganese ion than for the titanium due to its larger polarisability.

5.3.2.2 Intrinsic defect structure

Calculations of intrinsic defect energies using CASCADE were carried out on the ilmenite structure, and are summarised in table 5.3.2.2a (note that non-stoichiometric defect energies are calculated with respect to separate ions at infinity). The most stable intrinsic bulk defect is calculated to be the cation disorder defect; that is, the interchange of manganese and titanium cations. This defect is most stable when the sites are adjacent, with a formation energy of 0.7 eV per cation pair. Larger clusters of substitution defects were not examined due to computational limitations, but it is expected that Coulombic interactions and lattice strain would

Table 5.3.2.2a

Defect energies of MnTiO3 ilmenite

Lattice energy (ev)
-151.164

Intrinsic defects

Type	Energy (ev)
O vacancy	19.91
Mn vacancy	23.45
Ti vacancy	82.80
O interstitial	-12.65
Mn interstitial	-16.78
Ti interstitial	-69.85
Ti subst. for Mn	-55.15
Mn subst. for Ti	57.54
MnTi + TiMn subst.	2.39
MnTi+TiMn adjacent	0.70
O Frenkel	7.26
Mn Frenkel	6.67
Ti Frenkel	12.94
Schottky	14.82
O1- interstitial	2.54
O1- subst. for O	17.78
Ti3+ subst.	38.07
Ti3+ + O1- sep.	55.84
Ti3+ interstitial	-32.96
Ti3+ + O1- adj.	55.43

promote clustering of these defects. Next in stability is the manganese Frenkel and then oxygen Frenkel defects (644 kJ/mol and 700 kJ/mol), with the titanium Frenkel and Schottky defects considerably less stable. Comparing the oxygen Frenkel defect formation energy of 700 kJ/mol to the calculated oxygen Frenkel energy of 564 kJ/mol for the similar chromium^{III} oxide [Lawrence (1989)] we can see the formation of this defect is less likely in this material. Note that titanium interstitials and vacancies are calculated to be unstable with respect to displacement of manganese ions, thus where the cation ratio is not stoichiometric manganese defects and cation disorder are calculated to be the compensating defect. However, in the stoichiometric crystal the predominant defect is calculated to be cation disorder, whose low formation energy even with isolated ions implies significant disorder at room temperature. This is consistent with the partial cation site occupancies determined by Kidoh.

5.3.2.3 Lithium Niobate structure

The lithium niobate structure differs from the ilmenite in the ordering of the cation sublattice. Where the ilmenite structure contains dissimilar ions in adjacent cation sites, the lithium niobate structure pairs similar cations. A simple analysis

based on the relative stability of the ideal cation sublattices suggests that the two structures are similar in stability when the A and B ions have the same charge and radius, but with an increasing charge difference between the ions the lithium niobate structure gains in stability over the ilmenite structure. The calculated lattice energies and coordinates for the two structures are shown in Tables 5.3.2.1c and 5.3.2.1d. THBREL calculations performed on manganese titanate for both structures determines the lithium niobate structure as being more stable by 0.31 electron-volts per formula unit, assuming formal charges in the perfect crystal and contrary to the experimental order of stability. The elastic constants for the structures were calculated and are shown in table 5.3.2.3b. The high-pressure lithium niobate structure shows the larger elastic constants of the two structures and its calculated bulk modulus K_S (203 GPa) is larger than the experimentally known value of K_T (158 GPa) [Ross (1992)] (K_T cannot be calculated from static simulation results). Since the existence of cation disorder would reduce the effective charge difference of the two ion sites, modelling ions with formal charges may be a poor approximation. The potential model was therefore adjusted to determine the effects of non-integral charges on the lattice energies. The effect of cation charge on the relative stabilities of the two structures was estimated by adjusting the short-range cation-oxide potentials together with the ionic charges in order to maintain the same equilibrium

Table 5.3.2.3b

Calculated elastic and dielectric constants of ilmenite

Elastic constants (10**11 dyne/cm^2)

c11	c22	c33	c44	c66	c12	c13
34.40	34.40	24.83	3.78	9.07	16.26	6.05

Static dielectric constants

12.91	12.91	16.87

High frequency dielectric constants

1.73	1.73	1.71

Calculated elastic and dielectric constants of LiNbO3 structure

Elastic constants (10**11 dyne/cm^2)

c11	c22	c33	c44	c66	c12	c13
39.27	39.27	30.47	10.02	11.83	15.60	10.84

Static dielectric constants

15.12	15.12	89.76

High frequency dielectric constants

1.78	1.78	1.79

distance and the same force constant, thus allowing the effect of a reduction in the effective ionic charges to be modelled without affecting the equilibrium separation. The relative stabilities of the two structures with reduced ionic charges are shown in table 5.3.2.3c. The calculations show that reduction in ionic charges below 0.9 of the formal charges causes the ilmenite structure to become more stable than the lithium niobate structure, suggesting that the greater stability of the ilmenite structure observed experimentally may be due to lower effective charges or charge differences at the cation sites, which is affected by cation disorder as well as electronic defects.

5.3.2.4 Surfaces of $MnTiO_3$ Ilmenite

Manganese titanate grows preferentially along the <1,0,-1,0> axis [Takei (1981)] and has a distinct {0,0,0,1} cleavage, suggesting this surface is most stable. However the crystal morphology has not been studied in detail. Calculations were performed on many of the surfaces of the ilmenite structure using the MIDAS program [Tasker and Bullough (1980)], and the surface energies of the most stable surfaces are summarised in table 5.3.2.4a using rhombohedral Miller indices. The energies were calculated for unrelaxed and relaxed surfaces, that is for a surface which is a simple bulk termination, and also for the reconstructed surface after energy

Table 5.3.2.3c

Relative stability of the ilmenite and
lithium niobate structures for MnTiO3

Comparison of the lattice energies of the different
structures for MnTiO3 when scaling the ionic charges
down from their formal values. (eV)

Potentials		Ti			Mn	
factor	Charge	A	Rho	Charge	A	Rho
1.00	4.0	754.20	0.38790	2.0	715.80	0.34640
0.95	3.8	754.68	0.37172	1.9	793.88	0.32698
0.90	3.6	766.06	0.35440	1.8	910.69	0.30683
0.85	3.4	792.50	0.33591	1.7	1090.86	0.28601
0.80	3.2	840.84	0.31622	1.6	1382.01	0.26458

	Lattice energies (eV)		
Factor	Ilmenite	LiNbO3	(Ilmenite - LiNbO3)
1.00	-302.33	-302.95	0.62
0.95	-281.30	-282.00	0.70
0.90	-259.56	-261.67	2.11
0.85	-239.00	-238.67	-0.33
0.80	-221.96	-217.54	-4.42

Table 5.3.2.4a

Surfaces of MnTiO3 ilmenite

Space Group
R-3(R)

Regions I & II sizes
6 14

Surface Energies in J / metre^2

Orientation	Unrelaxed	Relaxed
(1,0,-1)	3.2287	0.5705
(1,1,1)	1.6317	0.7928
(1,2,2)	2.9208	1.1073
(1,1,0)	3.5701	1.2524
(0,2,1)	3.1225	1.4275
(1,2,0)	7.2777	1.4486
(1,-2,-2)	4.5207	1.6550
(1,0,0)	4.8706	1.7138
(1,1,-1)	4.6515	1.7484

minimisation. The large reductions in surface energy on relaxation and the re-ordering of the order of stability of the surfaces is striking, showing the necessity of considering relaxation of all low-index surfaces.

The equilibrium crystal morphology can be determined from the relaxed surface energies using Wulff's Theorem [Wulff], and the calculated morphology and relative surface areas of the crystal for the ilmenite structure are shown in table 5.3.2.4b. The morphology of the crystal is shown in figure 5.3.2.4a. The relaxation of the surfaces results in only 3 surfaces being expressed (see figure 5.3.2.4b), and leads to an elongated morphology along the hexagonal axis, in contrast to the flattened morphology that would be created from the unrelaxed surfaces. Calculations were also undertaken to examine the possibility of cation disorder at the surface, since the low energy of this defect in the bulk suggested that reordered cation layers at the surface may be favoured. The energies of the defective surfaces are given in table 5.3.2.4c, together with the defect energies. The disorder was modelled by exchanging the manganese and titanium ions in the two sites nearest the surface. Some of the surfaces are stabilised by the defect, in particular the (1,-2,-2) and the (1,1,-1) which gain over 0.5 J/m^2 in stability. However none of these surfaces are stabilised sufficiently to be expressed in the equilibrium morphology, so I would expect there to be no change apparent in the equilibrium morphology due to this

Table 5.3.2.4b

Relative surface areas of MnTiO3 ilmenite
before and after surface relaxation

Spacegroup: R-3(R)

Unrelaxed morphology

Miller Index (R)	S.E. (J/m^2)	Rel. Area
(1, 1, 0)	3.5701	1.88
(0,-1, 1)	3.2287	32.00
(0, 2, 1)	3.1225	17.52
(2, 2, 1)	2.9208	11.06
(1, 1, 1)	1.6317	37.54

Relaxed morphology (R)

Miller Index	S.E. (J/m^2)	Rel. Area
(1, 1, 1)	0.7928	25.49
(0,-1, 2)	0.5891	20.15
(0,-1, 1)	0.5705	54.37

Bulk stacking sequence

<0,-1,1>	<1,1,1>	<0,-1,2>
O - O	-Mn-	-Ti-
-O-	- O - O - O -	O - O
-Ti-Mn-Mn-Ti-	-Ti-	-O-
-O-	-Ti-	-Mn-
O - O	- O - O - O -	-Mn-
O - O	-Mn-	-O-
-O-	-Mn-	O - O
-Ti-Mn-Mn-Ti-	- O - O - O -	-Ti-

Surface layer

-O-	-Mn-	-O-
-O-		-Mn-
-O-	- O - O - O -	-O-
-O-		-Ti-
-Mn-	-Ti-	-O-
-Ti-Ti-	-Ti-	-O-
-Mn-	- O - O - O -	-O-
-O-		-Mn-
-O-	-Mn-	-Mn-
O - O	-Mn-	- O - Ti -
-O-		-O-
-Ti-Ti-	- O - O - O -	-O-
-Mn-		
-Mn-		

Surface stacking sequence after relaxation

Figure 5.3.2.4b

Table 5.3.2.4c

MnTiO3 surfaces with cation exchange

Index	Cation at Surface	Energies: Pure Surface J/m^2	Energies: Defective Surface J/m^2	Energies: Defect Formation kJ/mol
(0,2,1)	Mn	1.43	1.41	-4.00
(1,-2,-2)	Mn	1.66	1.10	-265.85
(1,0,-1)	Mn + Ti	0.57	0.97	52.39
(1,0,0)	Ti	1.71	1.23	-75.89
(1,1,-1)	Ti	1.75	1.05	-215.10
(1,1,0)	Ti	1.25	1.46	37.75
(1,1,1)	Mn	0.79	1.83	151.62
(1,2,2)	Mn	0.94	3.27	670.73

reordering. There is no obvious relationship between the formation energy of these defects and the order of the cation layers; showing that although the smaller, more highly charged cations will often be substituted by other cations at the surface, this is insufficient to predict the signs of all substitution defect formation energies.

5.3.2.5 Defect segregation

Energies of intrinsic surface defects and their segregation energies were calculated for the most stable surfaces using the CHAOS code. The defects were assumed to lie as near to the surface layer as possible. A summary of the surface defect and segregation energies is given in table 5.3.2.5a. Oxygen vacancies show a tendency to segregate to the {1,1,1} rhombohedral surface only, with a segregation energy of -1.3 eV, whereas cation vacancies tend to segregate to the other surfaces, particularly the most stable {0,-1,1} surface. Oxygen interstitials also segregate most strongly to the {0,-1,1} surface, suggesting this surface will have a cation deficit. Manganese substituting on a titanium site (giving a defect charge of -2) shows a large segregation energy to all surfaces, and having the most negative formation energy, will lead to net negatively charged surfaces and a positive space-charge region extending into the crystal. Titanium substitution on a manganese site however greatly

Table 5.3.2.5a

Surface defect energies

	Bulk	Surface defects			Segregation energies		
Index		(1,1,1)	(0,-1,1)	(0,-1,2)	(1,1,1)	(0,-1,1)	(0,-1,2)
Vacancies							
Mn	23.45	25.62	13.43	22.12	2.17	-10.02	-1.33
Ti	82.80	88.31	67.07	81.35	5.51	-15.72	-1.44
O	19.91	18.58	n/a	19.97	-1.33	n/a	0.06
Interstitials							
Mn	-16.78	3.83	-5.93	-18.60	20.61	10.85	-1.82
Ti	-69.85	-73.69	-46.97	-68.35	-3.83	22.89	1.51
O	-12.65	-12.97	-24.54	-18.95	-0.31	-11.89	-6.30
Substitutions							
Mn for Ti	57.54	3.22	3.26	3.43	-54.33	-54.28	-54.12
Ti for Mn	-55.15	1.80	3.76	0.24	56.96	58.92	55.39
- both -	2.39	5.02	7.02	3.66	2.63	4.63	1.27

prefers the bulk environment, due to the need to maintain full coordination of the small, highly charged cation. Thus the surface most stabilised by defects is the (0,-1,1), which will carry a net negative charge.

5.4 Summary

The model of strontium titanate replicates the experimental bulk lattice constant to within 2.3%, or just outside the experimental error. The calculation of the strontium titanate surfaces relaxations is compatible with the experimental results, while disagreeing with the previous calculations, and no addition reconstruction was found with the use of a surface supercell. The strontium termination was calculated to be the more stable surface by $3x10^{-2}$ J/m^2. The extent of surface relaxation is consistent with L.E.E.D. results [Bickel] for the strontium surface and shows a small contraction of the titanium surface which is not seen in the experiment but is seen in other calculations. However Mackrodt's results are at variance with these results, showing large contractions of the surfaces. Thus the calculation of strontium titanate surface relaxation is compatible with the experimental results, while disagreeing with the previous calculations. No additional reconstruction was found with the use of a surface supercell.

The calculated inter-ionic distances for manganese titanate agrees well with the experimental structure. The most common defect is calculated to be cation disorder with a defect energy of 0.7 eV. Calculation on the manganese titanate structures show that with formal charges the lithium niobate structure is found to be most stable, with the observed ilmenite structure less stable by 0.2 eV. However the ilmenite structure is found to be most stable when the cation charge difference is reduced to 85% of its formal value. Together with the small calculated cation disorder defect energy of 0.7 eV it is concluded that the ilmenite structure is stabilised by cation disorder, which is the predominant intrinsic bulk defects. This result is supported by the experimental determination of the manganese titanate structure by Kidoh which shows a high level of cation disorder. The calculated surface energies suggest many similar surfaces are expressed giving a rounded prolate morphology. Segregation of negative defects to the surface is expected to lead to surfaces containing excess oxygen and carrying a net negative charge, compensated by a positive space-charge region within the crystal.

Chapter 6

Barium Sulphate

6.1 Introduction

Barium sulphate is only slightly soluble in water, and its crystallisation creates a common scaling problem for water treatment systems, especially those in the off-shore oil industry [Rollheim *et al.* (1993)]. In this industry crystallisation occurs from saltwater, hence understanding the effect of other ions, especially alkaline earth ions, in solution on crystal growth would lead to more effective control of scaling. Thus any approach which can model ions at surfaces at the atomistic level can give us an improved understanding of the factors controlling the structure and stability of crystal surfaces. The aim is to use this information to determine the effect of these surface properties on morphology and growth of barium sulphate. The approach we adopted was first to use simulation methods to model the crystal structure and then the different surfaces of barite. Once calculated with some degree of reliability the segregation and the solution energies were determined for several impurities.

The aim of the work detailed in this chapter was not only to model the growth and morphology of barium sulphate crystals, but also to develop a simple strategy that could be rapidly applied to any polyanionic system. Where possible we compared the simulations with the experimental results to check the approach was appropriate and to aid the interpretation of the experimental data on crystal growth at the atomic level. The approach is straightforward: first model the bulk crystal, second apply this model to the surfaces which are involved in crystal growth, and finally consider the effects of important impurities on the structures and morphologies of the surfaces. The specific stages of this work were therefore:

1) Obtain and verify a reliable interatomic potential for barium sulphate.

2) Apply this potential to the modelling of the low index barium sulphate surfaces, to obtain surface energies and structures.

3) Evaluate the equilibrium crystal morphology and its sensitivity to changes in surface energies.

4) Determine the solubility of Mg, Ca and Sr impurities in the bulk crystal.

5) Model the surface energies and geometry of the segregation of Mg, Ca and Sr impurities to the surface of barium sulphate.

6) Calculate the effects on crystal morphology of the addition of impurities.

7) Compare these results with experiment, both to check the calculations and to give insight into the mechanisms of experimentally observed phenomena.

6.2 Experimental work on barite

The crystal structure and predominant habit of barium sulphate is known from mineralogical studies on barite and from studies on single crystals of synthetic and organic origin [Weijnen (1984), Mann (1990)]. The crystal structure of barite was first determined by James and Wood (1925). It has the space-group *Pnma*, showing the structure belongs to the orthorhombic class. All sulphate ions are crystallographically equivalent, as are all barium ions, with the barium and sulphur atoms lying on mirror planes. The unit cell contains a centre of inversion, thus the sulphate groups do not all have the same orientation and all surfaces should have a

non-dipolar termination. The large barium ion is coordinated by 12 oxygens from 7 sulphate groups. Its crystal structure is similar to that of lead sulphate and strontium sulphate, and in fact barium and strontium sulphate form a continuous solid solution series and occur together in minerals, with additional small concentrations of calcium and lead [Hamilton (1974)]. As barium sulphate scale cannot easily be removed chemically efforts are directed to prevention of its deposition. The structure of barite is well characterised and two experimental determinations [Sewada (1987), Hartman (1989)] of the structure are given in Table 6.2.1

Crystal morphology is controlled by the conditions under which the crystal is grown. Barite, either occurring naturally or grown under conditions of slight supersaturation, shows a tabular morphology, often as diamond-shaped short prisms with bevelled edges. Morphological studies on crystals isostructural to barium sulphate [Buckley (1935)] showed early on that the basic habit of this crystal type can be strongly affected by the presence of other ions during growth, and more recent work by Davey (1991) shows that barium sulphate morphology is easily altered by the presence of surface-active molecules. Doubly-charged diphosphonate ions can replace pairs of sulphate ions on the (0,1,1) surface, blocking growth on that surface. These morphological influences can be separated into two types, firstly those which affect the stability of the crystal surfaces, i.e. altering the relative surface free energy,

Table 6.2.1

Experimental structure of BaSO4
Space group Pnma (No. 62)

Ref: Sawada and Takuechi
Cell dimensions (Angstroms)
8.909 5.47 7.188

Atom	Wyck.	X	Y	Z
Ba		0.184	0.250	0.159
S		0.436	0.750	0.190
O	O4	0.592	0.750	0.122
O	O8	0.313	0.750	0.043
O	O14	0.421	0.538	0.313

Cell dimensions (Angstroms)
8.884(4) 5.458(3) 7.153(3)

Atom	Wyck.	X	Y	Z
Ba	4C	0.1846(1)	0.2500(-)	0.1581(1)
S	4C	0.4370(2)	0.7500(-)	0.1914(3)
O	4C	0.5878(6)	0.7500(-)	0.1062(10)
O	4C	0.3192(6)	0.7500(-)	0.0515(10)
O	8d	0.4186(4)	0.9702(5)	0.3190(7)

Ref: Hartman and Strom
Cell dimensions (Angstroms)
8.884 5.457 7.156

Atom	Wyck.	X	Y	Z
Ba	4C	0.1845	0.2500	0.1558
S	4C	0.4373	0.7500	0.1913
O	4C	0.5883	0.7500	0.1063
O	4C	0.3183	0.7500	0.0510
O	8d	0.4198	0.5299	0.3114

and secondly those affecting the relative rates of growth of each surface. The kinetic effects will play a dominant role in determining the morphology during phases of rapid growth, while the effects of the relative surface stabilities will be more apparent with slow growth rates and at equilibrium.

Recent work (1991) by J.D.Hopwood and S.Mann at Bath on the growth and morphology of barium sulphate has demonstrated that the crystal morphology shows a considerable variation with the degree of supersaturation. The degree of supersaturation (DS) is defined as

$$DS = \sqrt{([Ba][SO_4]/K_{sp})}$$

where K_{sp} is the solubility-product constant.

One effect of supersaturation is to increase the growth rate of the crystal. The rate, τ, is usually given by

$$\tau \propto (DS)^{\alpha}$$

where α is an empirically derived constant. However there have been a number of attempts to obtain quantitative estimates from theory (see Cheng (1989) and references therein), although this approach suffers from using highly idealised

model surfaces which for the most part are material independent.

At the onset of crystallisation an increase in the degree of crystallisation will lead to a greater driving force for crystallisation and hence an increased rate of growth. The significant changes in morphologies observed show that the rates of growth at different surfaces are themselves different. The question is whether this can be addressed via computer simulation. This will however greatly depend on the mechanism for growth. For example at high DS the growth may proceed by adsorption of clusters, compared to the adsorption of individual molecules at low DS. Alternatively, at low DS those surfaces which are most 'open', allowing easy access to surface sites, may grow most rapidly (geometric control), while at high DS growth may be favoured with those surfaces with the largest surface excess, (energetic control). Of the two types of mechanism, the former requires a reliable description of the aqueous phase while the latter is dependent on the solid surface. We can only address the importance for the second example, using the atomistic approach based on energy measurement of the surface.

In the work by Hopwood and Mann the degree of saturation (DS) was varied from 1.2 to 95. They found that when the DS was between 1.2 and 5.1 the crystals were lenticular in cross-section showing a rounded approximately (1,1,0) face, with the longest axis in the (0,1,0) direction. Increasing the DS to 8.2 increased elongation

in the (0,0,1) direction, and well formed (2,1,0) faces appeared. At DS = 21.8 the longest axis was in the (0,0,1) direction and the (2,1,0) faces were insignificant. Figure 6.2.1 shows the morphology at these saturations. On further increasing DS small (0,1,1) faces appeared and remained. However between DS 27.7 and DS 94.9 secondary crystal growths were observed on all crystals grown, giving the appearance of clusters at high DS. Crystals grown above DS = 50 showed extensive growth in the (0,0,1) and (0,1,0) directions, leading to cross-shaped crystals.

In the brines used in the offshore oil industry, the precipitation of barium sulphate is also influenced by the high concentrations of alkaline-earth ions present. Changes in growth due to the addition of alkaline-earth ions [Benton (1993)] at low supersaturation is evidenced by slight changes in the morphology in the presence of strontium and magnesium ions which is ascribed to the change of ionic strength, however addition of calcium ions has a significant effect, causing the crystal to become more plate-like, i.e. preferentially stabilising the (0,0,1) face. At high supersaturation calcium causes a thickening of the arms of the cross-shaped crystals, while strontium and magnesium still have little effect. Energy-dispersive X-ray analysis shows calcium and strontium were incorporated into the crystals with higher concentrations near the surface, with no trace of magnesium present.

The importance of ionic strength in crystal growth is not fully quantified, but,

Figure 6.2.1

The effect of supersaturation on morphology

(a) Morphology at low supersaturation

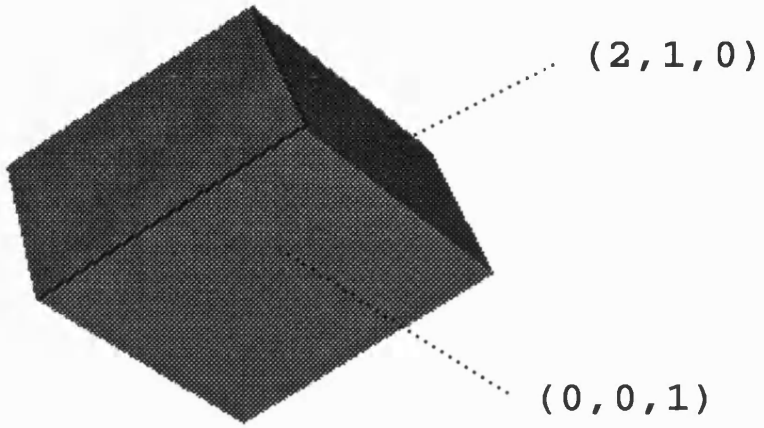

(b) Morphology at high supersaturation

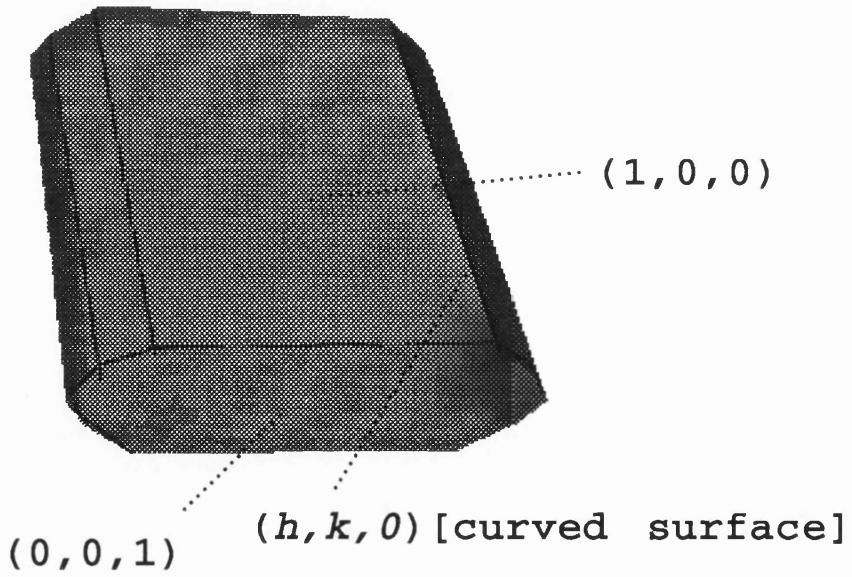

in general, when increased significantly it will stabilise charged surfaces. This occurs because with increasing ionic strength, the complementary space charge layer in solution increases in density and becomes thinner; neutralising the surface charge more effectively within a smaller distance from the interface. This will have the effect of increasing the cohesion and hence the surface stability. There will also be a secondary effect of allowing easier access of like ions of the same charge as the surface and in the extreme case this will allow crystallites to join. The morphology observed at high ionic strengths in Hopwood's work is shown in Figure 6.2.2, where the (0,0,1) and (1,0,0) surfaces dominate.

In the work by Hopwood and Mann, morphology was also affected by the pH, which was altered by the addition of 0.1 M HCl and 0.1 M NaOH. At pH 2.0 flat rhombic crystals characterised by large (0,0,1) faces and small (2,1,0) prismatic faces were found. Increasing the pH to 3.0 caused elongation along the (0,0,1) axis and the expression of a rounded {h,k,0} face (about (1,1,0)). The expression of the {h,k,0} faces reached a maximum extent at pH 5.6, but were significantly reduced at pH 7.0 and totally absent at pH 8.0. The (0,0,1) elongation was constant between pH 5.6 and pH 8.0. At pH 8.0 the crystals were again rhombic, with large (0,0,1) and (2,1,0) faces. Although not considered in this work, the effect of pH could be addressed by modelling the hydroxylation at low pH as the surface would be dominated by HSO_4^-,

Figure 6.2.2

The observed effect of ionic strength on morphology

(a) Morphology at low ionic strength

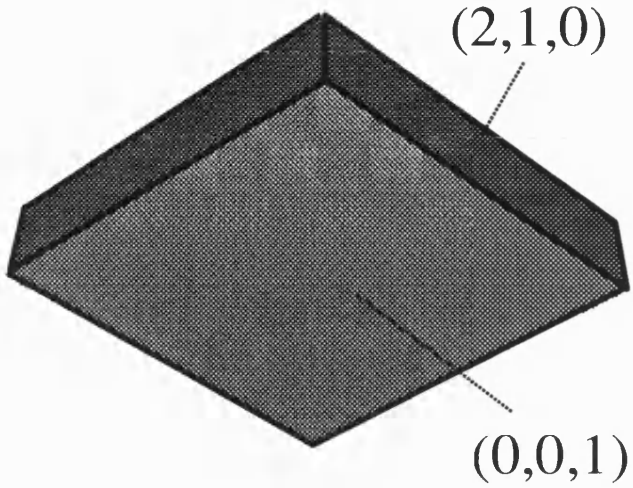

(b) Morphology at high ionic strength

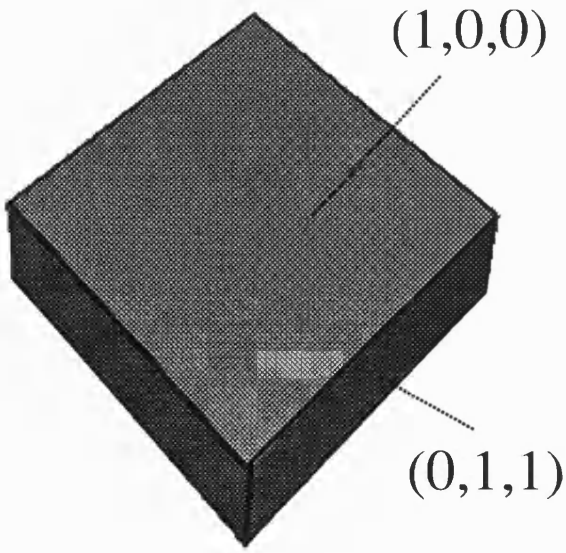

and at high pH by considering OH^- as an impurity. Because there is a large change of morphology with ionic strength, any adequate explanation of the morphology under a wide range of conditions must include mechanisms that depend on concentrations of various ions in solution.

6.3 Computational background to modelling the effects of additives on morphology

The use of atomistic simulation to model crystal structures is a well-established method for confirming or predicting experimental results, as well as for yielding an understanding of processes at the atomistic level [Parker (1989), Mackrodt (1988), Allan (1988), Ball (1990)]. The particular method used in this work, energy minimisation, allows us to take advantage of already existing potentials and to enable a greater number of calculations to be made than would be possible with other more computationally expensive methods, which are also often not suited to determining surface properties.

Recent calculations, using energy minimisation techniques, by Allan *et al.* (1993) have been made on a range of sulphates and provide a useful comparison with this work. They derived two models for barium sulphate, here donated as models *I*

and *II*. Their short-range potential forms for barium sulphate were derived from modified electron-gas calculations of the two-body interactions. These potentials were then adjusted by a radial 'shift' to improve the fit. This shift, and other parameters including shell charges for all of the ions and the sulphur and oxygen ionic were fitted to the experimentally observed structure and properties of $BaSO_4$. A non-fitted charge of +2 was given to Ba. A second potential (model *II*) was also derived, based on the Buckingham form and using Morse potentials with explicit three-body angle-dependent terms for the intramolecular sulphate interactions. The surface energies calculated with each model differed by 2-4 J/m^2 between the models, but showed similar relative stabilities between surfaces. However, despite the greater complexity of model *II*, model *I* showed greater relaxation of the surfaces and gave a final morphology closer to both our calculated and the experimental morphology. The two potentials described above were not used in this work as they were not available when this work was undertaken.

6.4 Potential Derivation

The aim was to establish a procedure for modelling polyanions which could help build a library of potentials similar to those obtained for oxides [Lewis and

Catlow (1985)]. I derived the interatomic potentials in a systematic way in an attempt to ensure that the parameters used to describe the forces were transferrable. The approach was first to take the anion potential derived for $CaCO_3$ by Jackson (1992), but setting the oxygen charge equal to -1 from -0.99, which is a value in agreement with other empirical and ab-initio calculations [Titiloye (1992)]. In addition, by redefining integer charges, future defect calculations should be more straightforward and if there are potentials derived for the interaction of ions with O^{1-}, they may be transferred to these systems as a first approximation. The potentials were then transferred to $CaSO_4$ except that the 3-body bond O-C-O which was modified so the equilibrium angle was the tetrahedral angle, 109.47°, instead of 120°. In addition, Jackson has also developed a model for K_2SO_4, and his S-O Buckingham potential was used. The $CaSO_4$ structure was then minimised and compared to experiment. The result was in reasonable accord with the experimental values, and therefore $SrSO_4$ and $BaSO_4$ were considered next. The Sr^{2+}-O^- and Ba^{2+}-O^- potential parameters were obtained by fitting the parameters developed for the binary oxides SrO and BaO [Lewis (1985)], to model the differences between Ca^{2+}-O^- for the calcium carbonate and Ca^{2+}-O^{2-} from CaO. The resulting minimised structure for $BaSO_4$ is given in Table 6.4.1, which can be compared to experimental structures given in Table 6.2.1. Another independent test for the $BaSO_4$ parameters can be

Table 6.4.1

Calculated BaSO4 unit cell

Space Group: Pnma

Lattice parameters (Å)		8.868	5.578	7.136
		Coordinates		
Atom	Wyckoff	X	Y	Z
Ba	4C	0.185	0.250	0.158
S	4C	0.448	0.750	0.190
O	4C	0.603	0.750	0.122
O	4C	0.341	0.750	0.035
O	8d	0.423	0.966	0.307

made as the experimentally determined elastic constants are known. This is not a rigorous fitting of the experimental data, but if such a simple recipe is successful it may be possible to generate relatively simply potentials for a wide range of polyanion systems such as nitrates and phosphates in which the cation parameters are largely common, allowing for the inclusion of mixed cation and anion effects. In Table 6.4.2 the calculated and experimental values are given and seen to be are in reasonable agreement. The simulated values are about 10 - 20% greater than the experiment which is not unusual [Saunders (1992)] and implies that the extent of relaxation will be slightly underestimated. The final barium sulphate potential is described in Table 6.4.3

6.5 Results and Discussion

All coordinates and miller indices given refer to the *Pnma* space group (No. 62).

6.5.1 Bulk properties

The parameters obtained for $BaSO_4$ were first used to obtain a minimum

Table 6.4.2

Experimental elastic constants at 293K

Ref: Haussuhl

c11	c22	c33	c12	c13	c23	c44	c55	c66
10.70	8.90	8.10	3.17	2.98	4.79	2.69	1.20	2.81

c11	c22	c33	c12	c13	c23	c44	c55	c66
11.06	9.51	8.37	3.36	3.28	5.13	2.77	1.18	2.90

Calculated elastic constants (10^11 dyne/cm^2)

c11	c22	c33	c12	c13	c23	c44	c55	c66
13.38	10.14	7.56	4.26	1.79	4.43	2.62	0.93	4.17

Calculated static dielectric constants

2.85	3.49	14.20

Table 6.4.3

Potential parameters

Ionic charges

Ba	S	O
+2.0	+2.0	-1.0

Short-range Buckingham potential parameters

Interaction	A (eV)	r (Å)	C (eV/Å^6)
O-O	36010.0	0.19756	0.00
Ba-O	7977.5	0.26980	0.00
S-O	1827.9	0.19910	0.00

Three-body parameters

K (eV/A^2)	θ_0 (degrees)
9.09724	109.47

Short-range cutoff:

10.8 Å

energy crystal structure shown in Table 6.4.1 which are similar to the experimental structure [Colville *et* al. (1967)] in Table 6.2.1. The differences in lattice parameter shown in Table 6.2.1 reveal that the largest discrepancy with the experimental structure is with the *b* lattice parameter which differs by 2.1%. In contrast, in the models developed by Allan *et al.* the fitted lattice parameters differed by no more than 1.4% from the experimental values. Our calculated volume is greater than the experimentally found volume by 2.7%, and the largest relaxation of an ion from the initial experimental coordinates is 0.2 Angstroms. Although this is a larger discrepancy than would be obtained by fitting the parameters directly to the structures determined in the different experiments, I believe this accuracy is acceptable and yields a more general potential than one fitted to a particular structure. The calculated structure reproduces the experimentally determined structure sufficiently well to proceed to calculate further properties.

Experimental elastic constants [Haussuhl (1990)] and the calculated elastic constants are shown in Table 6.4.2. The calculated values are seen to differ from the experimental values by 10% to 20%. There is some ambiguity with this as the experimental papers did not quote their crystal orientation. The difference in elastic constants is due largely to the inability of the model to include covalent interactions. One way to improve this aspect of the model may be to incorporate the shell model

into the potential. Although the rigid-ion model overestimates the elastic constants and so overestimates defect energies and underestimates relaxation of the ions in the same proportion, relative energies and stabilities are largely affected equally and hence show little net effect. The shell model was not used for these reasons, and due to the additional problems it introduces in the fitting procedure and the increased possibility of the fitted potential having unphysical aspects.

The cohesive energy calculated for this structure is -5993.5 kJ/mol. This is the enthalpy of the reaction:

$$Ba^{2+}(g) + S^{2+}(g) + 4O^{1-}(g) = BaSO_4(s)$$

The cohesive energies of strontium, calcium and magnesium sulphates were calculated to be -6121.4 kJ/mol, -6245.0 kJ/mol and -6494 kJ/mol respectively. As the covalency of the sulphate ion renders the assignment of formal charges to the sulphur and oxygen ions in isolation as somewhat arbitrary, the sulphate ion is best considered as a whole for the purpose of comparison with other sulphates. The formation of barite from its constituent ions may then be written as:

$$Ba^{2+}(g) + SO_4^{2-}(g) = BaSO_4(s)$$

The formation of the sulphate ion is calculated to be -3543.7 kJ/mol. The lattice energies calculated from this reaction for the barium, strontium, calcium and

magnesium sulphates respectively are thus -2449.8, -2577.7, -2701.3 and -2950.3 kJ/mol.

The determination of lattice energies from solution energies gives a lattice energy of -2469 kJ/mol for barite. A comparison of the lattice energies with values determined from solvation energies and the Born-Haber cycle are shown in Table 6.5.1.1. The barium and strontium sulphates show good agreement between the simulation lattice energies and those derived from solvation energies; however the calcium sulphate lattice energies do not agree, and the experimental values for $CaSO_4$ do not follow the trend expected from the ionic radii. This is because calcium sulphate adopts a different crystal structure - anhydrite - and the simulations were performed with the barite structure.

The relaxed structure of $BaSO_4$ is shown in Table 6.4.1. Comparison of the theoretical with the experimental structures shown in Table 6.2.1 shows that the calculated ionic coordinates lie within the variation of the reported experimental structure, i.e. within 0.1 Å of the reported coordinates. The calculated lattice parameters differ from the experimental ones by less than 2%, with the ***b*** parameter larger and the ***a*** and ***c*** parameters smaller than the experimental values. This anisotropic difference suggests that inaccuracies in surface energies and morphologies would first become apparent in relation to the ***b*** direction.

Table 6.5.1.1

Calculated and experimental lattice energies (kJ/mol)

This work

	S and O ions	Sulphate ion
BaSO4	-5,993.5	-2,449.8
SrSO4	-6,121.4	-2,577.7
CaSO4	-6,245.0	-2,701.3
MgSO4	-6,494.0	-2,950.3

Experimental work

	From Solvation	From B-H cycle	Reference
BaSO4	-2,469.0	-2,374.0	(a)
SrSO4	-2,577.0	-2,484.0	(a)
CaSO4	-2,489.0	-2,480.0	(b)
MgSO4	n/a	n/a	

(a) Selivanova, Karapetyants (1963) (b) Ladd, Lee (1968)

6.5.2 Pure Surfaces

Of central importance in understanding the effects of impurities on crystal growth is the ability to model the surfaces of pure $BaSO_4$. All low index surfaces with indices less than 3 were modelled. The relaxed surface structure was obtained by forming the bulk terminated equilibrium structure, then allowing the ions to adjust their positions until they experienced no net force. Minimising at constant volume enforces a constant surface area requirement on the slab. By varying the crystallographic orientation of the slab material, surfaces of different Miller index may be examined. The slab calculations were performed with a slab thickness of 4 unit cells and then repeated with a thickness of 8, to ensure the slab thickness was sufficient for convergent surface energies. For each surface the surface excess (defined as the energy difference between the surface and bulk ions per surface formula unit), and the surface energy per unit area were calculated and listed in Table 6.5.2.1. The surface energies produced from unrelaxed surfaces are shown in Table 6.5.2.1.1, to show the effect of surface relaxation. These are the energies that would be predicted with the PCB theory for example. It is noticeable that there are large changes in surface energy produced by the relaxation of up to 1.9 J/m^2. In addition,

Table 6.5.2.1: Surface energies and Excess of relaxed surfaces

Miller Index	Area ($Å^2$)	Excess (kJ/mol)	S.E. (J/m^2)
(0,0,1)	49.469	180.716	0.607
(0,1,0)	63.286	131.509	0.690
(0,1,1)	80.327	237.257	0.981
(0,1,2)	117.448	661.501	0.935
(0,2,1)	135.896	892.486	1.091
(1,0,0)	39.809	223.942	0.840
(1,0,1)	63.497	297.367	0.778
(1,0,1)b	63.497	366.643	0.953
(1,0,2)	106.647	612.776	0.954
(1,1,0)	74.765	291.964	0.648
(1,1,1)	89.650	410.158	0.760
(1,1,1)b	89.650	464.093	0.860
(1,1,2)	124.011	690.350	0.924
(1,2,0)	132.685	557.008	0.697
(1,2,1)	141.607	706.849	0.829
(1,2,2)	165.512	1,171.231	1.175
(2,0,1)	93.734	550.543	0.975
(2,1,0)	101.706	147.526	0.482
(2,1,2)	141.890	400.509	0.937

DVIE of expressed surfaces (negative implies sulphate excess)

Index	DVIE
(0,0,1)	-1.04
(0,1,1)	5.04
(1,0,0)	1.40
(1,1,0)	-1.21
(2,1,0)	1.01
(1,1,1)	3.44
(1,0,1)	-6.12
(0,1,0)	1.24

Morphology of relaxed crystal

Index	J/m^2	% total area
(1,0,0)	0.840	0.0
(2,1,0)	0.482	59.53
(1,1,1)	0.760	10.95
(1,0,1)	0.778	0.92
(0,1,0)	0.690	3.7
(0,0,1)	0.607	24.9

Table 6.5.2.1.1

Surface energies of unrelaxed surfaces

Miller index	Energy (Jm^{-2})
(0,0,1)	0.6785
(0,1,0)	0.8750
(0,1,1)	1.6286
(0,1,2)	2.6395
(0,2,1)	2.9664
(1,0,0)	1.4107
(1,0,1)	1.0680
(1,0,2)	1.6322
(1,1,0)	0.8847
(1,1,1)	1.1439
(1,1,2)	1.5364
(1,2,0)	1.0000
(1,2,1)	1.6995
(1,2,2)	3.1588
(2,0,1)	1.4538
(2,1,0)	0.6992
(2,1,1)	1.0905
(2,1,2)	1.5949
(2,2,1)	1.1101
(0,0,1)b	1.6010
(0,1,0)b	0.8750
(1,0,0)b	1.2368
(1,0,1)b	1.7331
(1,1,0)b	0.9187
(1,1,1)b	1.5421
(1,2,0)b	3.6464
(2,1,0)b	0.6992

Morphology of unrelaxed crystal

Miller index	Energy (Jm^{-2})	% Area
(2,1,0)	0.6992	60.60
(0,1,0)	0.8750	7.63
(1,0,1)	1.0680	0.87
(0,0,1)	0.6785	30.91

the degree to which each surface relaxes varies sufficiently such that the order of stability of the surfaces is not preserved, hence the unrelaxed energies can only be a crude guide to determining the equilibrium morphology of the crystal.

6.5.2.1 Equilibrium Morphology

Using the surface energies we can apply Wulff's Theorem [Wulff (1901)] to find the equilibrium morphology. Tables 6.5.2.1 and 6.5.2.1.1 show the fraction of the total surface formed from each index for the relaxed and unrelaxed surfaces; the morphologies are shown in Figure 6.5.2.1. The relaxed morphology is dominated by the (0,0,1) and the (2,1,0) surfaces, giving a lozenge shape. Interestingly the (1,1,1) surface is present despite its high surface energy. This is the shape of crystal that would be formed from a slow precipitation with no impurities present for a very small crystal, typically less than 1 μm. This is broadly similar to the morphology predicted by model *I* of the Allan *et al.* calculation, although they predict the presence of (0,1,1) faces while this work predicts the (1,1,1) surface will be expressed, and neither of these are observed during growth at low supersaturation [Hopwood (1991)]. However the extent to which kinetic factors control the growth is hard to judge. The experimental morphology seen in Hopwood and Mann's work shows a much flatter

Figure 6.5.2.1

Calculated morphologies

a) Unrelaxed surfaces

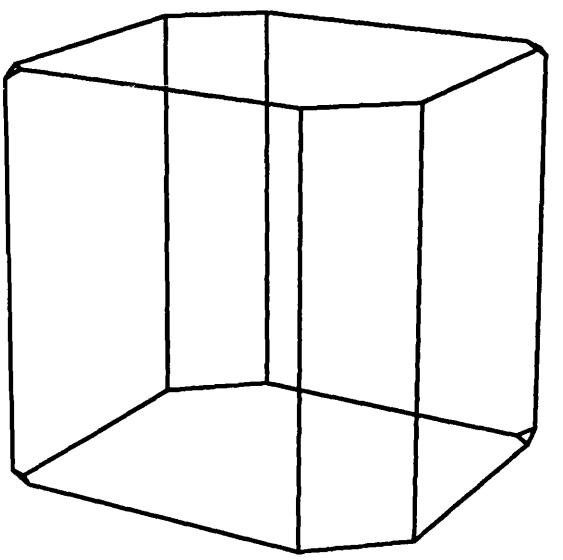

b) Relaxed surfaces

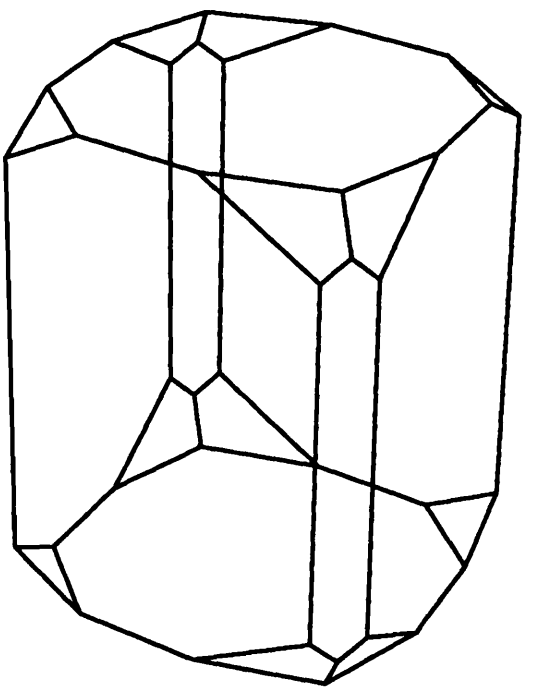

habit at relatively low supersaturation, and in this respect the model *I* morphology is closer, with a ratio of surface energies for (2,1,0) and (0,0,1) of ≅ 1.05, which is calculated to be ≅ 0.79 using our potential and the observed ratio varies from greater than about 5 to less than $\frac{1}{5}$, based on surface areas, as the supersaturation increases.

6.5.2.2 Ionic strength

In highly supersaturated solutions, or more generally solutions with a high ionic strength, the space charge effect of charged surfaces will attract a layer of counter-ions of opposite charge to the surface, which will effectively reduce the surface energy of that surface. Thus the (0,1,1) surface which has the highest charge would be the most stabilised. More highly charged ions have a greatly increased ability to form these charged layers, so we would expect the surfaces of positive charge, namely the (0,1,1), the (2,1,0) and the (1,0,0) to be most stabilised by concentrations of highly charged negative ions, while the (0,0,1) and (1,1,0) surfaces to by stabilised by positive ions of large valence. The surface charge can be expressed as a function of the difference in vacancy interactions energies (DVIE), i.e. the difference between vacancy formation energies at the surface and in the bulk. For surfaces of particular interest the DVIEs were calculated (this is discussed further

below). Several surfaces have more than one possible termination, and for these surfaces the DVIE was calculated for each termination. These values are summarised in Table 6.5.2.1. A negative DVIE implies an excess of sulphate will be present on the surface, creating a negatively charged surface. Most noticeable are the large but opposite values for the (0,1,1) and the (1,0,1) surfaces. The two dominant surfaces have lesser charges which are opposite in sign, suggesting that the relative proportion of these surfaces will be influenced by the concentrations and charges of counter-ions in solution.

6.5.2.3 Kinetic Effects

Under most common growing conditions the final morphology of the crystal will depend not only on the surface energies but also on the rates of growth of the different surfaces. To estimate the kinetic factors affecting growth is difficult, and a complete simulation of crystal growth is beyond the ability of these computational techniques at present. However some factors influencing growth rates can determined from these calculations.

At relatively low concentrations, when the critical cluster size is unlikely to be reached and the probability of adsorbed ions leaving the surface is high, the growth

rate will largely depend on the density of nucleating sites already present on the surface. For some surfaces, we have found there are two possible terminations of the surface with similar surface energies (the second termination is denoted in the tables by the suffix 'b' after the index). On the macroscopic scale we expect these surfaces to be composed of a mixture of both terminations, and hence are atomistically 'rough' due to the presence of steps between each region. This roughening of the surface should lead to rapid growth since step sites are centres for growth. The calculations show the (1,0,1) and (1,1,1) surfaces are likely to grow quickly by this mechanism, hence these surfaces will grow out and will not be present in the final crystal at low supersaturation.

Growth can only occur when ions in solution come into contact with surfaces of the crystal. However some ions will not remain on the surface but will return to solution. At equilibrium the rates of precipitation and dissolution must be equal, but during growth the ability of a surface to capture and keep ions will determine its growth rate. The probability that ions which impinge on the surface remain there is called the sticking factor. The larger the sticking factor the more quickly the surface will grow. An estimation of the relative sticking factors of various surfaces can be determined from the surface excess. The surface excess is the contribution to the lattice energy by forces perpendicular to the surface, per formula unit, and hence

measures the force with which incoming ions are held to the surface. It is assumed that the loss of solvation energy is similar for attachment to each surface. The surfaces with the largest excess will bind the ions most tightly to the surface and so will grow most quickly. The surface excess is shown in Table 6.5.2.1, and the surfaces present in the equilibrium morphology with the largest excess are the (1,1,1) and the (1,0,1) surfaces. In practice the surface morphology is largely determined by the kinetic factors i.e. the surface excess. Those surfaces with the lowest surface excess which together span the 3 dimensions (i.e. have non-zero components of each independent lattice vector) will contribute to the final morphology. In this study the lowest is the (0,1,0) at 132 kJ/mol, the (2,1,0) at 148 kJ/mol and the (0,0,1) at 181 kJ/mol. The expression of the (0,1,0) is unexpected but may indicate a limitation of the model particularly as the elastic constants in this direction (which are a limited representation of the force constants in a given direction) are much lower than the experiment.

6.5.3 Isovalent impurity segregation

The segregation energies were calculated by performing the bulk and surface calculations with a barium ion in the bulk or at the surface substituted by the impurity

ion. A comparison of the energies of a bulk-substituted material and a pure surface, with a pure bulk crystal and a substituted surface, yields the segregation and surface energies, which are given in Tables 6.5.3.1-6.5.3.3 The segregation energy for complete coverage was calculated from the following formula:

$$E_{seg} = (E_d - (E_p + nE_c))/n$$

and the surface energy was calculated from the formula:

$$E_{surf} = (E_d - (\tfrac{1}{2}E_b + E_c))/A$$

where

E_d is the energy of the substituted surface.

E_p is the energy of the unsubstituted surface.

E_c is the substitution energy (from CASCADE) given in Table 6.5.3.4.

E_b is the lattice energy of the bulk barium sulphate.

Table 6.5.3.4 compares the energy required to substitute an ion, determined from the calculated lattice energies and calculated from experimental heats of

Table 6.5.3.4

Comparison of substitution energies using calculated lattice energies and experimental heats of formation (kJ/mol)

CASCADE Substitution energies (eV)			
Vacancy	Sr^{2+}	Ca^{2+}	Mg^{2+}
21.88	-1.2	-2.08	-3.21

Solution energies in $BaSO_4$ (kJ/mol)			
$BaSO_4$	$SrSO_4$	$CaSO_4$	$MgSO_4$
0	12	52	191

Enthalpy of the reaction: $M^{2+}_{(g)} + BaSO_4 \Rightarrow MSO_4 + Ba^{2+}_{(g)}$

	M^{2+}	$BaSO_4$	MSO_4	Ba^{2+}	ΔH
Sr^{2+}					
Experimental	1,790.6	-1,465	-1,445	1,660.5	-110
Calculated	0	-5,993	-6,121	0	-128
Ca^{2+}					
Experimental	1,926	-1,465	-1,433	1,660.5	-234
Calculated	0	-5,993	-6,245	0	-252
Mg^{2+}					
Experimental	2,348.5	-1,465	-1,278	1,660.5	-501
Calculated	0	-5,993	-6,522	0	-529

formation [Cotton and Wilkinson (1988)]. The agreement between the two values for each ion is reasonable although the calculated value is in each case an overestimate, from 6% to 16%, due in part to the already mentioned large values for the elastic constants which underestimate the extent of lattice relaxation around the defect. Using the crude approximation that segregation energy is independent of coverage we can express the surface coverage as a function of segregation energy using the Arrhenius relation:

$$r_s/r_b = e^{-\Delta H/kT}$$

where

$$r_s = f_s/(1-f_s) \text{ and } r_b = f_b/(1-f_b) \approx f_b$$

represent the molar ratios of impurity to non-impurity ions at surface and bulk sites respectively, expressed here as occupancies. The change in surface energy caused by this coverage is given by

$$\Delta\gamma = f_s\Delta H_{seg}/A$$

where A is the surface area of 1 surface site. Generally, surfaces with negative segregation energies will be stabilised by the impurity (as this implies the surface energy of the impure surface is lower than the energy of the pure surface), and this stabilisation will be greater at lower temperatures. Positive segregation energies will have little effect at low temperatures, but will increasingly destabilise the surface at higher temperatures.

6.5.3.1 Strontium

Segregation energies were calculated for complete coverage of the surface by strontium ions. These energies are summarised in Table 6.5.3.1. The segregation energies are positive for the (0,0,1) and (2,1,0) faces, so these faces will remain relatively free of strontium ions, but the segregation energies are negative for the (1,1,1) and (1,0,1) faces, so we would expect strontium to segregate to these surfaces. Since their energy is lowered in the presence of the impurity, these surfaces will be stabilised. However the effect on the crystal morphology is small, with the fractional surface areas changing by under 1%. This is because the coverage is low at room temperature and the segregation energies are relatively small. As strontium sulphate

is completely soluble in barium sulphate, surface strontium ions should produce an environment for growth similar to the host crystal. If the impurity ion were less miscible a surface layer would present a barrier to further growth.

6.5.3.2 Calcium

The segregation and surface energies were calculated for 100% coverage and are summarised in Table 6.5.3.2. The segregation energies are generally more negative than for the strontium, and the (0,0,1) surface has a negative segregation energy, whilst the (2,1,0) surface has a positive one. Thus we would expect the addition of calcium to stabilise the (0,0,1) surface, giving the crystal a more plate-like morphology. Most of the segregation energies for calcium are more negative than for strontium, showing calcium segregates more readily. Furthermore the presence of calcium on the surface would be expected to hinder growth due to the more positive solution energy (see Table 6.5.3.4), thus in a kinetically controlled growth region the (0,0,1) surface area would be increased, perhaps with the (1,0,1) also being expressed.

6.5.3.3 Magnesium

Table 6.5.3.1

Surface and segregation energies for Sr^{2+} on $BaSO_4$

Miller Index	Energies at 100% coverage		% Coverage with 1% bulk impurity		
	Segregation	Surface			
	(kJ/mol)	(J/m^2)	T= 0K	T= 300K	T= 600K
Dominant surfaces					
(2,1,0)	8.34	0.51	0.00	0.04	0.19
(1,1,1)	-0.20	0.76	100.00	1.07	1.03
(0,1,0)	6.86	0.73	0.00	0.06	0.25
(1,0,1)	-8.48	0.76	100.00	23.05	5.19
(1,0,0)	26.98	1.05	0.00	0.00	0.00
(0,1,1)	-8.25	0.95	100.00	21.45	4.97
(1,1,0)	14.86	0.68	0.00	0.00	0.05
(0,0,1)	8.92	0.64	0.00	0.03	0.17
Other surfaces					
(0,0,1)b	-24.76	0.99	100.00	99.51	58.84
(0,1,0)b	6.86	0.73	0.00	0.06	0.25
(0,1,2)	-16.75	0.91	100.00	89.19	22.31
(0,2,1)	160.51	1.29	0.00	0.00	0.00
(1,0,1)b	-5.19	0.94	100.00	7.40	2.75
(1,0,2)	8.27	0.97	0.00	0.04	0.19
(1,1,0)b	16.81	0.68	0.00	0.00	0.03
(1,1,1)b	36.88	0.93	0.00	0.00	0.00
(1,1,2)	-13.99	0.91	100.00	73.21	14.18
(1,2,0)	12.67	0.71	0.00	0.01	0.08
(1,2,0)b	9.30	1.14	0.00	0.02	0.15
(1,2,1)	1.20	0.83	0.00	0.62	0.78
(1,2,2)	-29.86	1.15	100.00	99.94	79.91
(2,0,1)	9.35	0.99	0.00	0.02	0.15
(2,1,1)	15.54	0.79	0.00	0.00	0.04
(2,1,2)	4.55	0.94	0.00	0.16	0.40
(2,2,1)	4.82	0.70	0.00	0.14	0.38

Table 6.5.3.2

Surface and segregation energies for Ca^{2+}

Miller Index	Energies at 100% coverage		Percent coverage with 1% bulk impurity		
	Segregation	Surface			
	(kJ/mol)	(J/m^2)	T= 0K	T= 300K	T= 600K
Dominant surfaces					
(2,1,0)	13.45	0.53	0.00	0.00	0.07
(1,1,1)	-18.50	0.73	100.00	94.33	28.97
(0,1,0)	2.70	0.70	0.00	0.34	0.58
(1,0,1)	-35.31	0.69	100.00	99.99	92.22
(1,0,0)	62.04	1.19	0.00	0.00	0.00
(0,1,1)	-26.16	0.87	100.00	99.72	65.43
(1,1,0)	18.59	0.69	0.00	0.00	0.02
(0,0,1)	-38.93	0.48	100.00	100.00	96.08
Other surfaces					
(0,0,1)b	-77.74	0.82	100.00	100.00	100.00
(0,1,0)b	2.70	0.70	0.00	0.34	0.58
(0,1,2)	-49.32	0.87	100.00	100.00	99.49
(0,2,1)	135.92	1.26	0.00	0.00	0.00
(1,0,1)b	-35.12	0.86	100.00	99.99	91.94
(1,0,2)	-13.87	0.93	100.00	72.26	13.90
(1,1,0)b	23.43	0.69	0.00	0.00	0.01
(1,1,1)b	15.00	0.89	0.00	0.00	0.05
(1,1,2)	-48.39	0.86	100.00	100.00	99.39
(1,2,0)	16.54	0.72	0.00	0.00	0.04
(1,2,0)b	-3.72	1.12	0.00	4.26	2.07
(1,2,1)	-20.31	0.81	100.00	97.18	36.97
(1,2,2)	178.47	1.35	0.00	0.00	0.00
(2,0,1)	-1.64	0.97	100.00	1.89	1.37
(2,1,1)	-7.64	0.75	100.00	17.62	4.42
(2,1,2)	-18.00	0.92	100.00	93.16	26.96
(2,2,1)	-11.38	0.69	100.00	48.96	8.92

Segregation energies were calculated for 100% coverage and are summarised in Table 6.5.3.3. The magnesium ion has a large negative segregation energy on all surfaces, even giving rise to negative surface energies for the (0,0,1) and (0,1,0) faces. As confirmed by the solution energies in Table 6.5.3.4, magnesium has the greatest tendency of the 3 ions to segregate from the bulk barium sulphate. Some of the calculated surface energies are negative, showing that the tendency to segregate would cause fission of the crystal along an internal layer of magnesium ions. In practice the unfavourable solution energy would prevent incorporation of magnesium ions into the crystal. If magnesium ions occupied lattice sites on the surface of a growing crystal however, further growth of the crystal would be hindered as the magnesium ions would be buried, creating the unfavourable bulk defects. If magnesium was present this effect would occur on all faces with negative segregation energies.

6.6 Summary

The calculated bulk crystal structure shown in Table 6.4.1. shows acceptable agreement with the experimental structure. The largest difference is an increase of 0.1 Å in the second lattice vector. This elongation is manifested by the increased

Table 6.5.3.3

Surface and segregation energies for Mg^{2+}

Miller Index	Energies at 100% coverage		% coverage with 1% bulk Mg^{2+}		
	Segregation	Surface			
	KJ/mol	J/m^2	T= 0K	T= 300K	T= 600K
Dominant surfaces					
(2,1,0)	-99.08	0.16	100.00	100.00	100.00
(1,1,1)	-197.26	0.39	100.00	100.00	100.00
(0,1,0)b	-139.82	-0.04	100.00	100.00	100.00
(1,0,1)	-246.21	0.13	100.00	100.00	100.00
(1,0,0)	-132.18	0.38	100.00	100.00	100.00
(0,1,1)	-197.18	0.17	100.00	100.00	100.00
(1,1,0)	-91.02	0.45	100.00	100.00	100.00
(0,0,1)b	-334.50	-0.04	100.00	100.00	100.00
Other surfaces					
(0,0,1)	-180.90	0.00	100.00	100.00	100.00
(0,1,0)	-107.37	0.13	100.00	100.00	100.00
(0,1,2)	100.17	1.08	0.00	0.00	0.00
(0,2,1)	-31.10	1.05	100.00	99.96	83.61
(1,0,1)b	-240.55	0.32	100.00	100.00	100.00
(1,0,2)	-257.05	0.55	100.00	100.00	100.00
(1,1,0)b	-46.34	0.54	100.00	100.00	99.08
(1,1,1)b	-147.69	0.59	100.00	100.00	100.00
(1,1,2)	-244.21	0.60	100.00	100.00	100.00
(1,2,0)	-66.10	0.61	100.00	100.00	99.98
(1,2,0)b	-134.31	0.96	100.00	100.00	100.00
(1,2,1)	-208.02	0.58	100.00	100.00	100.00
(1,2,2)	-202.33	0.97	100.00	100.00	100.00
(2,0,1)	-163.78	0.68	100.00	100.00	100.00
(2,1,1)	-165.54	0.52	100.00	100.00	100.00
(2,1,2)	-168.48	0.74	100.00	100.00	100.00
(2,2,1)	-161.16	0.53	100.00	100.00	100.00

separation of the barium and sulphate ions within the cell in that direction, and is not due to distortion of the sulphate anion. In accord with other simulations, explicit three-body bonds are not necessary to model the crystal, however the success of the models I and II [Allan *et* al. (1993)] calculations suggest that the development of a shell model to include the electronic polarisability, for the barium ion in particular, would largely eliminate this elongation. The agreement between simulated and experimental crystal structures suggest that the potential is adequate for modelling surface stability.

The calculated surface energies give rise to morphologies that are most consistent with those found from crystallisation at low supersaturation of barium sulphate. The morphologies produced by unrelaxed and relaxed surfaces are shown in Figure 6.6.1. The presence of the (1,0,1) and (1,1,1) surfaces do not appear to be confirmed by experiment. Their absence can be explained by kinetic factors. Several of the surfaces have two or more terminations, and if these are similar in energy they will coexist at the macroscopic scale. Hence we might expect these 'rough' surfaces to grow more rapidly i.e. in this case the (1,1,1) and (1,0,1) surfaces. The main difference from the experimentally grown crystals is the enhanced stability of the (0,1,0) surface. Work by Hartman (1989) showed that this surface is stabilised by the electrostatic contributions to the surface stability, thus this may be an indication that

Figure 6.6.1

Morphologies with segregation

a) Strontium

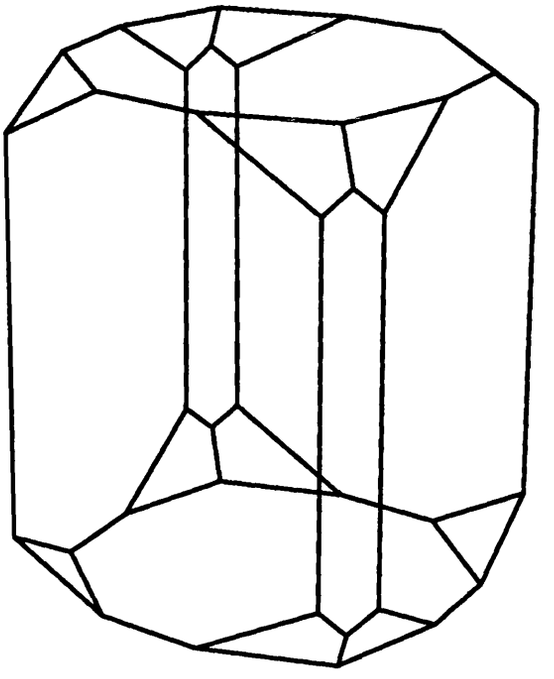

b) Calcium

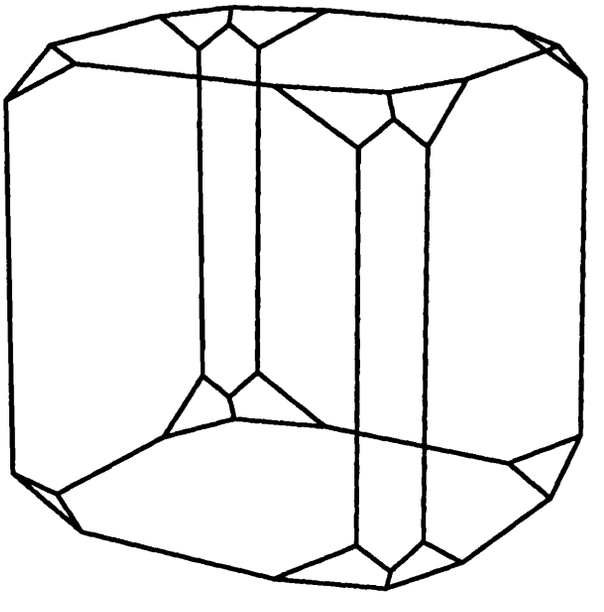

we have overestimated the electrostatic contribution if we assume the habit observed shows the equilibrium morphology. This assumption however is not justified in the absence of a much better understanding of kinetic contributions to the morphology.

At high ionic strengths charged surfaces will be stabilised by a space charge effect. Since the effectiveness of the space charge depends on the valence of the ions contributing to it, the charged surfaces are stabilised more by more highly charged ions. For example, the presence of multiply charged anions would stabilise the positively charged surfaces with low surface excesses, namely the (0,1,1) and the (1,0,0) surfaces. In addition the (1,1,1) and (1,0,1) surfaces have high surface charges, but as discussed above the (1,1,1) will grow out during growth. We must also not exclude the possibility that we are introducing problems by not using relaxed defect energies, which may reduce some of the defect energies.

The impurity segregation calculations show the strontium ion will segregate to and stabilise the (1,0,1) and (1,1,1) surfaces slightly, if they are present. However the effect on the equilibrium morphology will be small. Calcium segregates to the (0,0,1) surface and will reduce the surface energy, modifying the equilibrium morphology significantly as shown in Figure 6.2. We would expect the presence of calcium ions on the surface to also inhibit growth, acting as a blocking mechanism. In contrast magnesium, although it has significant segregation energies has a very endothermic

solution energy and hence magnesium will not dissolve in barium sulphate. Thus the effects will not be as dramatic as the segregation energies suggest. There is some recent evidence that these predictions are reasonable by comparison with the work by Benton (1993) for strontium and calcium ions which shows strontium and magnesium have little effect on morphology, with strontium incorporated into the crystal, but with no trace of magnesium substituted. Calcium had a significant effect on the morphology, with reduced expression of the (2,1,0) surface, and was also present in the grown crystal. The small observed effect of magnesium ions is consistent with the calculated properties if magnesium ions are largely absent from the surfaces. From the solution energy in Table 6.5.3.4 and the segregation energies in Table 6.5.3.3, magnesium ions on the expressed surfaces are calculated to be unstable with respect to bulk $MgSO_4$, hence unstable with respect to unsaturated magnesium sulphate solution. Thus magnesium is calculated not to be adsorbed onto these surfaces, which is confirmed by X-ray analysis. The effects of segregation are confirmed predicted surprisingly well considering the assumption of coverage-independent segregation energies.

Lattice, surface, and defect energies calculated by these methods strictly correspond to potential energies at a fixed temperature. Nevertheless static simulations can provide insight into the dynamics of crystal growth by determining

driving forces and heights of potential barriers for specific mechanisms. Once a potential model has been developed using static simulations, temperature effects can be checked using the potential model with methods which explicitly include the effects of varying temperature, namely the techniques of lattice dynamics and molecular dynamics.

Conclusions

This thesis has been concerned with the application of computer simulation techniques to the study of complex oxides and their surfaces. In this work we have made several achievements in extending the range of calculations based on static simulations. In Chapter 4 we modelled zinc oxide surfaces, including the defective and dipolar surfaces, and the segregation of intrinsic and extrinsic impurities to those surfaces. This enabled us to predict the surface features which would be present under reaction conditions and resolve some ambiguities concerning the role of copper on zinc oxide surfaces. In particular copper stabilises steps on the prism faces, which are shown to be easily formed and are predicted to cluster in terraces. The preferred defect structure of the polar surface is calculated to include a high concentration of vacancies on the oxygen terminating layer. We have shown how Monte-Carlo methods can extend classic static calculations to model temperature-related phenomena such as adsorption energies. Modelling of ternary oxides showed the bulk structure and the surface relaxation can be determined for ilmenite- and perovskite-structured compounds. The calculated strontium titanate surfaces showed similar relaxed structures to those experimentally determined, with a contraction of the interlayer spacing of about 10% between the topmost two layers, and only a slight

surface rumpling caused by different relaxations of the cations and anions at the surface. The surface energies of the two terminations were within 0.03 J/m^2 of each other, suggesting the surface is composed of a macroscopic mixture of both titanium- and strontium-terminated surface layers. In contrast to the strontium titanate surfaces, calculations on the ilmenite, manganese titanate, surfaces show large changes of the surface energies on relaxation, and that the most stable surfaces after relaxation are the (1,1,1), (0,-1,1) and the (0,-1,2) surfaces. The large change in surface energy after relaxation shows the importance of performing these calculations on all possible low-index surfaces for non-cubic structures. Calculation of the intrinsic defect energies of manganese titanate showed the predominant defect to be cation disorder, with a defect energy of 0.7 eV for the exchange of adjacent cations. Manganese substituted at titanium sites showed the most negative segregation energies for all of the surfaces considered, showing the preference of the titanium ion for the bulk environment and suggesting the surfaces will bear a net negative charge. Experimental work on manganese titanate finds the ilmenite structure to be more stable than the lithium niobate structure by about 6 kJ/mol at room temperature and pressure. Therefore the greater stability of the calculated lithium niobate structure for manganese titanate compared to the lithium niobate structure might suggest a limitation of the potential model. However significant cation disorder - involving

about 8% of cation sites - is also observed experimentally, in line with our calculated defect energies. Calculations using modified charges to model the effects of cation disorder showed the ilmenite structure became the most stable when the charges were changed by more than 10% from their formal values. Thus we conclude that the observed cation disorder stabilises the ilmenite structure relative to the lithium niobate structure. This example also suggests we should exercise caution in extrapolating calculations on perfect structures to real materials where significant concentrations of defects are known to occur. The growth of barium sulphate crystals is an example where defects and kinetic effects play a major role in determining crystal size and shape. In Chapter 6 we showed how, despite the lack of experimentally determined surface energies, we were able to determine the accuracy of our calculated surface energies by comparing calculated and experimental morphologies. The potential parameters were derived by modification of a calcite potential. Despite this simple derivation the calculated and experimental lattice parameters agreed to within 2%. The largest differences in structure are related to the overestimation of the elastic constants, which could be improved by introducing ionic polarisability for the barium ion in our model. The experimental variation of morphology with ionic strength was closely related to the calculated tendency of the surface to become charged, showing the importance of space charge effects in

stabilising surfaces during growth from solution. Direct calculation of growth rates was impossible, but the calculation of the surface excess and arguments from surface roughness were able to explain the changes in morphologies observed at high supersaturation. The modification of the morphology by the presence of alkaline earth ions in solution during growth was determined by calculating solution energies and segregation energies to each surface, showing calcium has the greatest effect, which was confirmed by experimental morphologies and analysis of impurities in grown crystals. The use of morphologies to compare calculated and experimental surface energies is improved when kinetic effects can be estimated, but remains limited due to the uncertainty of solvation effects.

This work has shown the versatility of atomistic simulation not only in modelling static structures and defects of complex materials, but in going beyond the equilibrium structures to include kinetic effects by evaluating possible mechanisms. The addition of entropic and temperature effects can only improve the scope and predictive power of these methods.

References

Akher S., Cheng W.H., Lui K., and Kung H.H., *J.Catal.*, 1984, **85**, p437

Akher S., Lui K. and Kung H.H., *J.Phys.Chem.*, 1985, **89**, p1958

Allan, N.L. and Mackrodt, W.C. *Phil. Mag. A*, **58,** 1988, p555.

Allan N.L., Rohl A.L., Gay D.H., Catlow C.R.A., Davey J.D. and Mackrodt W.C., *Faraday Discuss.*, 1993, 95

Allen M.P. and Tildesley D.J., "Computer Simulation of Liquids", Oxford University Press, 1987, ISBN 0-19-855645-4

Amrein T., Kabius B., Burger J., Saemannischenko G., Schultz L., Urban K., Jourenal of Alloys and Compounds, 1993, Vol. 195, No. 1-2, p129-132

Anpo Masakazu and Kubokawa Yutaka, *J. Phys. Chem.*, 1984, pp5556-5560

Atkins P.W. (Ed.), "Physical Chemistry", 3rd. Ed., 1987

Au C.T., Hirsch W., Hirschwald W., *Surface Science 197*, 391-401, 1988

Au C.T., Hirsch W., Hirschwald W., *Surface Science 199*, No.3, 507-517, 1988

Au C.T., Hirsch W., and Hirschwald W., *Surface Science*, **221**, 113-130, 1989

Ball R.G.J. and Grimes R.W. J. *Chem. Soc. Faraday Trans.* 86, 1990, 1257.

Benton W.J., Collins I.R., Grimsey I.M., Parkinson G.M. and Rodger S.A., *Faraday Discuss.*, 1993, 95, (in press)

Bickel N., Schmidt G., Heinz K., and Muller K., *Phys. Rev. Lett*, **62**, 17, 2009, 1989

"Topics in current Physics: Applications of the Monte-Carlo Method in Statistical Physics",Ed. Binder K., Springer-Verlag, 1987

Bowker Micheal, Houghton Hilary and C. Waugh Kenneth C., *J. Chem. Soc., Faraday Trans. I*, 1981, 77, 3023-3036

Bowker M., Houghton H., Waugh K.C.,, Giddings T., and Green M., *J.Catal.*, 1983, **84**, 252-255

Bowker M., Hyland J.N.K., Vandervell H.D., Waugh K.C., *Int. Congr. Catal.*, [Proc.] 8th (1984, Pub. 1985), Vol 2, pp35-46

Bowker M., Hadden R.A., Houghton H., Hyland J.N.K., Waugh K.C., *J. Catal.* 109, 263-273, 1988

Vera Bolis, Bice Fubini and Elio Giamello, *J. Chem. Soc., Faraday Trans. 1*, 85(4), 855-867 (1989)

Born M., Huang K., "Dynamical Theory of crystal lattices", Oxford University Press, 1954, ISBN 0-19-851248-1

Bragg W.L., Nature (London), 105, 646, (1920)

Buckingham A.D., *Adv. Chem. Phys.* 12, 107., (1967)

Buckley H.E., *Z. Krystallogr.*, 1931, 78, p412

Buckley H.E., *Z. Kristallogr*, 1935, 91, p375

Buhler J.P. and Crandell R.E., *J. Phys. A*, 1990, Vol. 23, No. 12, pp2523-2528

Burch R., Golunski S.E. and Spencer M.S., *J. Chem. Soc. Faraday Trans. 1*, 1990, **86**, 2683

Burch R., Golunski S.E. and Spencer M.S., *Catal. Lett.*, 1990, **5**, 55

Catana A., Locquet J.P., J. Mat. Research, 1993, Vol. 8, No. 6, 1373-1378

"Lecture Notes in Physics: Computer Simulation of Solids", Ed. Catlow C.R.A. and Mackrodt W.C. (Springer-Verlag 1982).

Catlow C.R.A., James R., Mackrodt W.C., Stewart R.F., Phys. Rev. 25, 1982, 2, 1006

Catlow C.R.A., Stoneham A.M., *J.Phys.C.:Solid State Phys.*, 16 (1983), 4321-4338

Cerva H., and Russwurm W., *J.Am.Ceram.Soc.* **71**,522 (1988)

Cheng V.K.W., *J. Crys. Growth,* 1989, 96, pp293-303

Chinchen G.C., Spencer M.S., and Whan D.A.,, *Appl. Catal.*, 1986, **25**, 101

Chinchen G.C., Spencer M.S., Waugh K.C. and Whan D.A.,, *J. Chem. Soc., Faraday Trans. 1*, 1987, **83**, 2193

Chinchen G.C., Denny P.J., Parker D.G., Short G.D., Spencer M.S., Waugh K.C. and Whan D.A., *Am. Chem. Soc., Div. Fuel Chem.,* 1984, **29**, 178.

Cockroft Nigel J., Lee Steven H., and Wright John C., *Phys. Rev. B*, Vol. 44, No. 9, (1991)

Colville A.A., Staudhammer K., *American Mineralogist*, 1967, 52, 1877 (Barium sulfate structure from Inorganic Crystal Structure Database at DVLB)

Cormack A.N., Freeman C.M., Catlow C.R.A. and Royle R.L., "Advances in Ceramics, Vol. 23: Nonstoichiometric Compounds", ISBN 0-916094-86-3, pp283-291, 1987

Cotton & Wilkinson, "Advanced Inorganic Chemistry", John Wiley & Son. ISBN 0-471-84997-9, 1988

Cox P.A., "The Electronic Structure and Chemistry of Solids", Oxford Science Publications, 1987, ISBN 0-19-855205-X, p215

Dauber-Osguthorpe P., Roberts V.A., Osguthorpe D.J., Wolff J., Genest M., Hagler A.T., 'Proteins; Structure,Function & Genetics', Vol 4, p31-47, 1988.

Davidson W.C., AEC Report ANL-5990(Rev), 1990

Davies M.J., Ph.D. Thesis, University of Bath, 1992

Davey R.J., Black S.N., Bromley L.A., Cottier D., Dobbs B. & Rout J.E., *1991, 353, p549-550*

Dick B.G., and Overhauser A.W., Phys. Rev., *112*, 90-103 (1958)

Duffy D. M. and Tasker P. W., *Harwell Report R9130* (1978), Harwell Lab., U.K.

Duffy D.M., and Tasker P.W., *Harwell Report* R11059, 1983, Harwell Lab, UK.

Elliot D.J.,and Pennella Filippo, *J. Catal. 114*, 90-99(1988)

Ewald P.P., *Ann. Physic,* 1921, 64, p253

Fletcher R., Powell M.J.D., Computer J., 6, 16, 1963

Frost J.C., Nature **334**, 577 (1988)

Gerlach W., *Zeitschrift fuer Physik*, 9, 184, (1922)

Gilbert, T.L. (1968). J.Chem.Phys. *49*, 2640. Soft-Sphere Model for Closed Shell Atoms and Ions.

Gillan M.J., J.Chem.Soc.-F.Trans. II, 1989, Vol.85, pp.521-536

Goodby Brian E. and Pemberton Jeanne E., *Applied Spectroscopy*, Vol. 42(5), 1988, pp 754-760

Griffin G.L. and Yates J.T. Jr, *J.Chem.Phys.*, 1982, **77**, 3751

Guest M.F., Kendrick J., and Poper S.A., Program GAMESS documentation, S.E.R.C. Daresbury Laboratory (1983)

Hamilton W.R., Woolley A.R., Bishop A.C., The Hamlyn giude to Minerals, Hamlyn, ISBN 0-600-56394-4, 1974

Harding J.H., Harwell Report R13127 (1988), Harwell Lab., UK

Hartman P. and Strom C.S., *Journal of Crystal Growth*, 97, 1989, 502512

Haussuhl S., *Z. Krystallogr.*, 1990, 192, pp137-145

Healy F., Ph.D. thesis, University of Keele, January 1993, pp47-51

Heyes D.M., Barber M. and Clarke J.H.R., 1977 *J.Chem.Soc. (Faraday II)* **11**, 1485.

Hopwood J.D., First Year Report (Sept. 1991), Bath University., also
to be published, J. Crystal Growth

Huang C.J., Tseng T.Y., Materials Chemistry and Physics, 1993, Vol. 34, No. 2, 110-114

Hutson A.R., *Phys. Rev.*, v108, No.2, 222-230
I.C.S.D. at S.E.R.C. Chemical Database System(CDS)

Jackson J.D., "Classical Electrodynamics", Wiley, New York, 1962

Jackson R.A.,"*Computer Modelling of Fluids Polymers and Solids*", Eds. Catlow C.R.A., Parker S.C., Allen M.P., 1990, pp395-404, ISBN 0-7923-0549-3

Jackson R.A., Price G.D., Catti M., and Pavasi A., *Phys. Chem. Minr.*, 1992, Vol.19, No.2, 80-87

James R.W. and Wood W.A., *Proc. Roy. Soc.*, 1925, **A109**, p598

Jaffe J.E., Pandey R., and Kunz A.B., *Phys.Rev.B* **43**,14030 (1991)

Kenway P.R., Ph.D. Thesis, University of Bath (1991)

J.G. Kirkwood, Phys. Z., 33, 1932, 57-60

Molecular statistical calculation of gas adsorption by silicalite, Kiselev A.V. (the late), Lopatkin A.A, Shulga A.A., Zeolites, 1985, Vol 5, July p261-267

Molecular statistical calaculation of the thermodynamic adsorption characteristics of zeolites using the atom-atom approximation: Part 2. Kiselev A.V., Pham Quang Du, J. Chem. Soc., Faraday Trans. 2, 1981, 77, 1-15

Kidoh Kumiko, Tanaka Kiyoaki and Marumo Fumiyuki, *Acta Cryst.* **B40**, pp 329-332 (1984)

Klier K., *Adv. Catal.*, 1982, **31**, 243

Kroger F.A., "The Chemistry of Imperfect Crystals", North Holland Publishing Co. (Amsterdam), 1964, p691

'Numerical Data and Functional Relationships in Science and Technology',Vol 17b,Landholt-Bornstein New Series, (1982 Springer-Verlag).

Leinenweber Kurt, Utsumi Wataru, Tsuchida Yoshihiko, Yagi Takahiko, and Kurita Kei, *Unquenchable high-pressure perovskite polymorphs of $MnSnO_3$ and $FeTiO_3$, Phys. Chem. Minr.*, **18**, pp244-250 (1991)

Leslie M.L., *Daresbury Laboratory Technical Memorandum DL/SCI/TM31T*, 1982, Daresbury Lab., U.K.

Lewis G.V., Catlow C.R.A., *J. Phys. C:Solid State Phys.*, 18, 1985, pp1149-1161

Lidiard A.B. and Norgett M.J., @Computational Solid State Physics", Ed. Herman F.D., Dalton N.W., Koehler T.R., Plenum press, New Tork, 1972, 385

Liu L. and Basset W.A., "Elements, Oxides and Silicates", *Oxford Monographs on Geology and Geophysics*, No. 4, (Oxford University Press, New York, 1986), pp97-98

Mackrodt W.C., *Ceramics Microstructures* (1986).

Mackrodt W.C., *Phys. Chem. Minerals*, (1988), **15**, 228-237

Mackrodt W.C., *Solid State Ionics* **12** (1984), 175-188

Mackrodt W.C. and Stewart R.F., *J. de Physique, Coll. C6,* **41**, 1990, 7,

C6-64,

Muller A., Proc. Roy. Soc. London Ser. A, 154, 1936, 624-639

Muller K.A. and Berlinger W., *Phys. Rev. B* 34, 6130, 1986

Muller K.A. and Berlinger W., *Phys.Rev.Lett.*, 26, 13, 1971

Mann S., Didymus S.J., Sanderson N.P., Heywood N.P. & Aso-Samper E.J. *J. chem. Soc. Faraday Trans.*, 1990, 86, pp1873-1880

Metropolis N., Rosenbluth A.W., Rosenbluth M.N., Teller A.H. and Teller E., *J. Chem. Phys.*, 21, 1087, 1953

Mott N.F. and Littleton M.J., *Trans. Faraday Soc.*, 1938, **34**, 485.

Natta G., "Catalysis" (D.H.Emett, Ed.), Vol. 3, p349, Reinhold, New York, 1955.

Norgett M.J., J.Phys.C, *4*, 298, 1971

Norgett M.J., Harwell Report R7650 (1974), Harwell Lab., UK

Book of data, Nuffield Advanced Science, Ed. Harrison R. D., Penguin Books (1972)

Parker S.C., (1983), Ph.D. Thesis, University College, London.

Parker, S.C. and Price, G.D. *Advances in Solid State Chemistry* 1, 1989, 295.

Parry D.E., *Surface Science,* 1975, 49, p433

Parry D.E., Surface Science 54, 195, 1976, (*erratum*)

Peng L.-M. and Czernuska J.T., *Phil.Mag. A* 1991, Vol. 64, No. 3, 533-541

Pisani C., Dovesi R., and Roetti C., "Lecture Notes in Chemistry, vol. 48, Hartree-Fock Ab Initio Treat of Crystalline Systems", 193pp, Springer-Verlag, New York, 1988

Prade J., Schroder U., Kress W., de Wette F. W., Kulkarni A. D., *J. Phys. Condens. Matter* **5**, pp1-12, (1993)

Rollheim M., Shamsili R.G., Ostvold T. and Siamos A., *Acta Chemica Scandinavica*, 1993, Vol.47, No.4, pp 358-367

Ross Nancy L., "Stability of Minerals", Chapman & Hall, Chapter 4.

Ross Nancy L., Ko Jaidong, and Prewitt Charles T., *Phys. Chem. Minr.*, **16**, pp 621-629 (1989)

Salem L., Mol. Phys., 3, 1960, 441-452

Proceedings of the Japan Academy, Sasaki S., Fujino K., Takeuchi Y., 55, 43, (1979)

Saunders G.A., Parker S.C., Benbattouche N., and Alberts H.L., *Phys. Rev. B*, 1992, Vol.46, No.14, pp 8756-8767

Sawada H. and Takuechi Y., *Z. Krystallogr.*, 1987, 181, p179

Sengupta G., Mandal N.K., Kunda M.L.L., Sanyal R.M. and Dutta S., *J.Colloid and Interf. Science.*, vol. 117, No. 2 June 1987

Schmahl N.G., Barthel J., Eikerling G.F., *Zeitschrift fuer Anorganische und Allgemeine Chemie*, 332, 230, (1964)

Schmahl N.G., Eikerling G.F., *Zeitschrift fuer Physikalische Chemie (Frankfurt Am Main)*, 62, 268, (1968)

Schooley J.F., Hosler W.R. and Cohen M.L., *Phys. Rev. Lett.* 12, 474 (1964)

Takei H., *Journal of Materials Science*, **16**, pp1310-1316 (1981)

Tasker P. W. and Bullough T. J., *Phil. Mag. A*, **43**, p313, (1980)

Tasker P.W., AERE Harwell Report No. TP999

Tasker P.W., *J.Phys. C*, **12**, 4977 (1979)

Tasker P.W., 1978 AERE Report No. AERE-R9130

Tilley R.J.D., *J.Solid State Chem.*, 21, 293, 1977

Titiloye J., personal communication, 1982

Titiloye J.O., Parker S.C., Stone F.S. and Catlow C.R.A. *J. Phys. Chem.* 95, 1991, 4038.

Titiloye J.O., Tschaufeser Petra and Parker Stephen C., "Topics in inclusion science: Spectroscopic and Computational Studies of Supramolecular Systems", Ed. Davies J.E.D., ISBN 0-7923-1958-3, 1992, pp137-185

Todate Yoshiei, Ishikawa Yoshikazu, Tajima Keisuke, Tomiyoshi Syoichi and Tahei Humihiko, *J. Phys. Soc. Jap.*, Vol. 55, No. 12,1986, pp4464-4476

Tosi M.P., Solid State Physics, 16, 1, 1964

Tschudi T., Herden A., Goltz J., Klumb H., Laeri F., and Albers J., *IEEE J. Quantum Electron.* **QE-22**, 1493 (1986)

Vetrivel R., Catlow C.R.A., Colbourn E.A., J. Phys. Chem., 1989, Vol.93, No.11, pp4594-4598

Weijnen M.P.C. and van Rosmalen G.M., *Industrial Crystallisation*, 84, 1984, pp61-66

Wulff G., *Z. Kristallogr. Kristallgeom.*, 34, 949, (1901)

Appendix 1

Monte-Carlo subroutine

```
subroutine mc(ispace)
dimension ispace(*)
parameter (maxtyp=20, MAXMOL=40)
common/dprecn/idoub,idoubm
common/thbr/thbrun
common /timing/tstart,tlast,tjob
common /dmcntl/lds(40),ldn(40),maxcor,maxcrd,nvar,maxcdf,
1  maxplu,maxrun
common/bascas/xbas(3,6000),lbas(6000)
common/bascch/ibasp(6000)
common/basis/nspe,nineb(20),ineb,mfineb(20),mlineb(20),
1 nbass,ncors,nshels,nbas,ncor,nshl,maxspe
common/lattis/rlatv(6),xlat(3,3),xrcp(3,3),vc,origin(3),
1 rlscal,rlat(10),acclat,ncrys
common/ions/chargf(maxtyp),amass(maxtyp),ntypf
common /mc1/lnvf,lnvl
common /max/maxbas
common/mciter/mcal,fcal,etot
logical thbrun,lorder,prmv,debug,nopr,dfile
character*8 ibasp,dumpfile
character*4 AA
real xold(50), err, a, b, c, xl2, zzz, theta, phi, twopi
real xrel(3,400), xrelold(3,400), xt(400), xtold(400)
real rndpos(400),rndold(400)
real beta, betam, seed, elat, eold, R,abst, trfac,mindist,etot
real cossum(3),sinsum(3), time, trem, tlast, tmin
integer errstat, fcal, mcal, totm, mtot, dmpct, dmpnm
lorder=.false.
prmv=.false.
debug=.false.
nopr=.false.
dfile=.false.
mcal=0
fcal=0
totm=0
```

```
dmpct=0
mtot=-1
etot=0.0
trfac=1
c
tmin=5.0
twopi=6.28318530717959
R=8.6168E-5
err = 1.0E-6
mindist=0.7/rlat(1)
c
c     set up dynamic memory
c
lds(2)=lds(1)+ldn(1)
ldn(2)=3*maxbas*idoub
lds(3)=lds(2)+ldn(2)
ldn(3)=3*maxbas*idoub
lds(4)=lds(3)+ldn(3)
ldn(4)=3*maxbas*idoub
lds(5)=lds(4)+ldn(4)
c
ldn(5)=18000*idoub
lds(6)=lds(5)+ldn(5)
c
if (debug) then
write(6,*)'iboub  =',idoub
write(6,*)'maxbas =',maxbas
write(6,*)'lds(1) =',lds(1)
write(6,*)'lds(2) =',lds(2)
write(6,*)'lds(3) =',lds(3)
write(6,*)'lds(4) =',lds(4)
write(6,*)'lds(5) =',lds(5)
write(6,*)'lds(6) =',lds(6)
write(6,*)'lnvf,lnvl =',lnvf,lnvl
end if
c
c     read in parameters
c
c 333   read(5,331,ERR=332,IOSTAT=errstat)AA
```

```
c 331   format(A4)
333  call input
call inpa(AA)
if (AA.eq.'STOP'.or.AA.eq.'stop') goto 334
if (AA.eq.'MOLS'.or.AA.eq.'mols') goto 335
if (AA.eq.'ITER'.or.AA.eq.'iter') goto 336
if (AA.eq.'TEMP'.or.AA.eq.'temp') goto 337
if (AA.eq.'TRAN'.or.AA.eq.'tran') goto 338
if (AA.eq.'PRIN'.or.AA.eq.'prin') goto 339
if (AA.eq.'ORDE'.or.AA.eq.'orde') goto 340
if (AA.eq.'STAR'.or.AA.eq.'star') goto 341
if (AA.eq.'SPEC'.or.AA.eq.'spec') goto 342
if (AA.eq.'MIND'.or.AA.eq.'mind') goto 343
if (AA.eq.'PRMV'.or.AA.eq.'prmv') then
prmv=.true.
goto 333
end if
if (AA.eq.'MOVE'.or.AA.eq.'move') goto 344
if (AA.eq.'DUMP'.or.AA.eq.'dump') goto 345
if (AA.eq.'DFIL'.or.AA.eq.'dfil') goto 346
if (AA.eq.'NOPR'.or.AA.eq.'nopr') then
nopr=.true.
goto 333
end if
if (AA.eq.'ENDS'.or.AA.eq.'ends') goto 350
write(6,*)'Unknown Keyword: ->',AA
goto 333
c
c 332   if (errstat.lt.0) then
c       write(6,*)'Unexpected E.O.F. on input'
c       stop
c       else
c       write(6,*)'Error on input'
c       stop
c       end if
c
334   write(6,*)'Stop command encountered'
stop
c
```

```
335   call inpi(nummol)
if (nummol.lt.0) then
write(6,*)'Error: number of molecules invalid',nummol
stop
end if
if (nummol.gt.0) numspe=(lnvl-lnvf+1)/nummol
write(6,*)'->',AA,lnvf,lnvl,nummol,numspe
goto 333
c
342   call inpi(numspe)
if (numspe*nummol.gt.(lnvl-lnvf+1)) then
write(6,*)'Error:no. of species required exceeds those given',
$ nummol,numspe
stop
end if
write(6,*)'->',AA,numspe
goto 333
c
336   call inpi(numjup)
if (numjup.lt.0.0) then
write(6,*)'Error: jump variable invalid',numjup
stop
end if
write(6,*)'->',AA,numjup
goto 333
c
344  call inpi(mtot)
if (mtot.lt.0) then
write(6,*)'Error: negative number of moves'
stop
end if
write(6,*)'->',AA,mtot
goto 333
c
337   call inpf(abst)
write(6,*)'->',AA,abst
goto 333
c
338   call inpf(trfac)
```

```
if (trfac.gt.2.0) then
write(6,*)'Warning: trfac too large',trfac
end if
write(6,*)'->',AA,trfac
goto 333
c
343   call inpf(mindist)
write(6,*)'->',AA,mindist
goto 333
c
339   write(6,*)'Lattice vectors'
write(6,*)xlat(1,1),xlat(2,1),xlat(3,1)
write(6,*)xlat(1,3),xlat(2,2),xlat(3,2)
write(6,*)xlat(1,3),xlat(2,3),xlat(3,3)
write(6,*)'Order of species is as follows:'
do 12 lino=1,nbas
write(6,170)lino,ibasp(lino)(1:4),ibasp(lino)(5:8),
1     xbas(1,lino),xbas(2,lino),xbas(3,lino)
12    continue
goto 333
c
340   write(6,*)'Order factor calculation'
lorder=.true.
goto 333
c
350   write(6,*)'->',AA
return
c
345   write(6,*)'->',AA
call outint(9)
goto 333
c
346   write(6,*)'->',AA
dfile=.true.
call inpa8(dumpfile)
call inpi(dmpnm)
goto 333
c
341   continue
```

```
write(6,*)'     - Start of Monte Carlo calculation -'
write(6,*)' '
c
call elac(elat,ispace(lds(2)),ispace(lds(3)),ispace(lds(5)),
$     ispace(lds(6)),ispace(lds(4)),ispace(lds(1)))
c
write(6,*)'Initial energy =',elat
write(6,*)' '
c
c     time=second(1)
c  ** Use NAG random number generator **
call g05ccf
ix=lnvl-lnvf + 1
c
nnn=lnvf-1
c
if (debug) then
write(6,*)'lnvf,lnvl,nummol,numspe = ',lnvf,lnvl,nummol,numspe
write(6,*)' '
write(6,*)'Species to be moved'
write(6,*)' '
do 142 i = lnvf,lnvl
write(6,170)i,ibasp(i)(1:4),ibasp(i)(5:8),
1     xbas(1,i),xbas(2,i),xbas(3,i)
142  continue
write(6,*)' '
end if
do 141 kkk=0,nummol-1
xt(kkk*3+1)=0.0
xt(kkk*3+2)=0.0
xt(kkk*3+3)=0.0
masst=0.0
do 14 i=1,numspe
nnn=nnn+1
xt(kkk*3+1)=xt(kkk*3+1)+xbas(1,nnn)*amass(lbas(nnn))
xt(kkk*3+2)=xt(kkk*3+2)+xbas(2,nnn)*amass(lbas(nnn))
xt(kkk*3+3)=xt(kkk*3+3)+xbas(3,nnn)*amass(lbas(nnn))
masst=masst+amass(lbas(nnn))
14       continue
```

```
xt(kkk*3+1)=xt(kkk*3+1)/masst
xt(kkk*3+2)=xt(kkk*3+2)/masst
xt(kkk*3+3)=xt(kkk*3+3)/masst
141   continue
write(6,*)'*',xlat(1,1),xlat(2,1),xlat(3,1)
write(6,*)'*',xlat(1,2),xlat(2,2),xlat(3,2)
write(6,*)'*',xlat(1,3),xlat(2,3),xlat(3,3)
write(7,*)'*',xlat(1,1),xlat(2,1),xlat(3,1)
write(7,*)'*',xlat(1,2),xlat(2,2),xlat(3,2)
write(7,*)'*',xlat(1,3),xlat(2,3),xlat(3,3)
call sol3(xlat,xt,rndpos,nummol)
do 15 i=1,nummol
do 152 ij=1,numspe
do 151 j=1,3
xrel(j,ij+numspe*(i-1))=xbas(j,ij+numspe*(i-1)+lnvf-1) -
$ xt(j+3*i -3)
151      continue
152   continue
15   continue
write(6,*)'xt(i) =',(i+1,xt(3*i+1),xt(3*i+2),xt(3*i+3),
$   i=0,nummol-1)
cossum(1)=0.0
cossum(2)=0.0
cossum(3)=0.0
sinsum(1)=0.0
sinsum(2)=0.0
sinsum(3)=0.0
c
call tremain(trem)
tlast = second(1)

c                @@@ main loop @@@
do 29 jup=1,numjup
c
c *** check time remaining ***
if ((trem + tlast - second(1)).lt.tmin) then
write(6,*)' '
write(6,*)'Dump: seconds left = ',(trem+tlast-second(1))
call outint(9)
```

```
goto 293
end if
c
if(dfile) then
if(dmpct.eq.dmpnm) then
open(8,file=dumpfile,status="UNKNOWN")
call outint(8)
close(8)
else
dmpct=dmpct+1
end if
end if
c *** translation ***
if(.not.nopr) then
write(6,*)'choice no. =',jup
end if
do 291 kkk=0,nummol-1
if (lorder) then
cossum(1)=cossum(1)+cos(xt(kkk*3+1)*xrcp(1,1)+
$ xt(kkk*3+2)*xrcp(2,1)+xt(kkk*3+3)*xrcp(3,1))
cossum(2)=cossum(2)+cos(xt(kkk*3+1)*xrcp(1,2)+
$ xt(kkk*3+2)*xrcp(2,2)+xt(kkk*3+3)*xrcp(3,2))
cossum(3)=cossum(3)+cos(xt(kkk*3+1)*xrcp(1,3)+
$ xt(kkk*3+2)*xrcp(2,3)+xt(kkk*3+3)*xrcp(3,3))
sinsum(1)=sinsum(1)+sin(xt(kkk*3+1)*xrcp(1,1)+
$ xt(kkk*3+2)*xrcp(2,1)+xt(kkk*3+3)*xrcp(3,1))
sinsum(2)=sinsum(2)+sin(xt(kkk*3+1)*xrcp(1,2)+
$ xt(kkk*3+2)*xrcp(2,2)+xt(kkk*3+3)*xrcp(3,2))
sinsum(3)=sinsum(3)+sin(xt(kkk*3+1)*xrcp(1,3)+
$ xt(kkk*3+2)*xrcp(2,3)+xt(kkk*3+3)*xrcp(3,3))
end if
xtold(kkk*3+1)=xt(kkk*3+1)
xtold(kkk*3+2)=xt(kkk*3+2)
xtold(kkk*3+3)=xt(kkk*3+3)
rndold(kkk*3+1)=rndpos(kkk*3+1)
rndold(kkk*3+2)=rndpos(kkk*3+2)
rndold(kkk*3+3)=rndpos(kkk*3+3)
do 21 i=1,3
rndpos(3*kkk+i)=rndpos(3*kkk+i)+trfac*2*(g05caf() - 0.5)
```

```
if (rndpos(3*kkk+i).gt.1.0) rndpos(3*kkk+i) =
$       rndpos(3*kkk+i) - 1
if (rndpos(3*kkk+i).lt.0.0) rndpos(3*kkk+i) =
$       rndpos(3*kkk+i) + 1
xt(3*kkk+i)=0.0
21      continue
do 27 i=1,3
do 277 l=1,3
xt(3*kkk+l)=xt(3*kkk+l) + rndpos(3*kkk+i)*xlat(i,l)
277     continue
27      continue
theta = g05caf()
phi = g05caf()
cs=cos(theta*twopi)
sn=sin(theta*twopi)
do 28 lin=1,numspe
xrelold(1,numspe*kkk+lin)=xrel(1,numspe*kkk+lin)
xrelold(2,numspe*kkk+lin)=xrel(2,numspe*kkk+lin)
xrelold(3,numspe*kkk+lin)=xrel(3,numspe*kkk+lin)
zzz=xrel(2,numspe*kkk+lin)
xrel(2,numspe*kkk+lin)=xrel(2,numspe*kkk+lin)*cs -
$  xrel(3,numspe*kkk+lin)*sn
xrel(3,numspe*kkk+lin)=zzz*sn + xrel(3,numspe*kkk+lin)*cs
28      continue
cs=cos(phi*twopi)
sn=sin(phi*twopi)
do 281 lin=1,numspe
zzz=xrel(1,numspe*kkk+lin)
xrel(1,numspe*kkk+lin)=xrel(1,numspe*kkk+lin)*cs -
$  xrel(3,numspe*kkk+lin)*sn
xrel(3,numspe*kkk+lin)=zzz*sn + xrel(3,numspe*kkk+lin)*cs
281     continue
do 282 lino=1,numspe
do 283 i=1,3
xbas(i,numspe*kkk+lino+lnvf-1)=xt(3*kkk+i) +
$  xrel(i,numspe*kkk+lino)
283     continue
282     continue
291     continue
```

```
if (lorder) then
do 292 i=1,3
order=sqrt(cossum(i)*cossum(i)+sinsum(i)*sinsum(i))
write(6,*)'Order',i,'=',order
292      continue
cossum(1)=0.0
cossum(2)=0.0
cossum(3)=0.0
sinsum(1)=0.0
sinsum(2)=0.0
sinsum(3)=0.0
end if
eold=elat
do 297 iit=1,nbas
do 297 jjt=lnvf,lnvl
if (iit.eq.jjt) goto 297
zzz=(xbas(1,iit)-xbas(1,jjt))*(xbas(1,iit)-xbas(1,jjt))
zzz=zzz+(xbas(2,iit)-xbas(2,jjt))*
$ (xbas(2,iit)-xbas(2,jjt))
zzz=zzz+(xbas(3,iit)-xbas(3,jjt))*
$ (xbas(3,iit)-xbas(3,jjt))
if (zzz.lt.mindist*mindist) then
if (ibasp(iit)(5:8).eq.ibasp(jjt)(5:8)) then
if(.not.nopr) then
write(6,*)'No move - species too close'
write(6,*)iit,ibasp(iit),jjt,ibasp(jjt)
end if
goto 2626
end if
end if
297   continue
c     write(6,*)'Loop duration =',second(1)-time
c     time=second(1)
call elac(elat,ispace(lds(2)),ispace(lds(3)),ispace(lds(5)),
$     ispace(lds(6)),ispace(lds(4)),ispace(lds(1)))
c
c     write(6,*)'Elac duration =',second(1)-time
c     time=second(1)
if (elat.le.eold) goto 31
```

```
if (exp((eold - elat)/(R*abst)).ge.g05caf()) goto 31
2626  continue
do 262 ii=0,nummol - 1
xt(3*ii+1)=xtold(3*ii+1)
xt(3*ii+2)=xtold(3*ii+2)
xt(3*ii+3)=xtold(3*ii+3)
rndpos(ii*3+1)=rndold(ii*3+1)
rndpos(ii*3+2)=rndold(ii*3+2)
rndpos(ii*3+3)=rndold(ii*3+3)
do 261 lin=1,numspe
do 26 i=1,3
xrel(i,numspe*ii+lin)=xrelold(i,numspe*ii+lin)
xbas(i,numspe*ii+lin+lnvf-1) =
$       xrel(i,numspe*ii+lin) + xt(3*ii+i)
26        continue
261         continue
262         continue
if(.not.nopr) then
write(6,*)'_fail_ for no.',jup,elat
elat=eold
write(6,190)elat
c         write(7,191)elat
end if
elat=eold
fcal=fcal + 1
etot=etot + elat
goto 29
31    continue
mcal=mcal + 1
if(.not.nopr) then
write(6,*)'_move_ for no.',jup
write(6,190)elat
write(6,*)'xt(i) =',(i+1,xt(3*i+1),xt(3*i+2),xt(3*i+3),
$    i=0,nummol-1)
end if
c         write(7,190)elat
c         write(7,*)xt(1),xt(2),xt(3)
c         write(7,*)theta,phi,elat
c         write(7,*)'      *'
```

```
if (prmv) then
do 311 lino=lnvf,lnvl
write(6,110)ibasp(lino)(1:4),ibasp(lino)(5:8),
1       xbas(1,lino),xbas(2,lino),xbas(3,lino)
311     continue
end if
etot=etot + elat
if (mcal.eq.mtot) goto 293
29   continue
c                @@@ end of main loop @@@
293  totm=mcal + fcal
write(6,*)'Total trials = ',totm
write(6,*)'Moves = ',mcal
write(6,*)'% moves:',100.0*float(mcal)/totm
write(6,*)'Fails = ',fcal
write(6,*)'% fails:',100.0*float(fcal)/totm
write(6,*)'Av. energy = ',etot/float(totm)
goto 333
100  format(//,6X,'coordinates of species to moved be are',/)
110  format(3X,A4,3X,A4,3F20.15)
120  format(//,6X,'increments in the x, y and z directions are',/,
1  6X,'xbit =',f20.15,'  ybit =',f20.15,'  zbit =',f20.15)
130  format(/,6X,'time for energy calculation =',f10.6,' seconds',
1  /,6X,'lattice energy = ',f20.8,' eV')
140  format(//,6X,'coordinates of moved species for this calc',/)
170  format(I3,3X,A4,3X,A4,3F20.15)
180  format(' xshift =',F20.15,' yshift =',F20.15,' zshift =',F20.15)
190  format(6X,'Energy = ',F20.8,' eV')
191  format(6X,'Energy = ',F20.8,' eV')
end
```